

## **INFORMATION TO USERS**

**This manuscript has been reproduced from the microfilm master. UMI films the text directly from the original or copy submitted. Thus, some thesis and dissertation copies are in typewriter face, while others may be from any type of computer printer.**

**The quality of this reproduction is dependent upon the quality of the copy submitted. Broken or indistinct print, colored or poor quality illustrations and photographs, print bleedthrough, substandard margins, and improper alignment can adversely affect reproduction.**

**In the unlikely event that the author did not send UMI a complete manuscript and there are missing pages, these will be noted. Also, if unauthorized copyright material had to be removed, a note will indicate the deletion.**

**Oversize materials (e.g., maps, drawings, charts) are reproduced by sectioning the original, beginning at the upper left-hand corner and continuing from left to right in equal sections with small overlaps.**

**Photographs included in the original manuscript have been reproduced xerographically in this copy. Higher quality 6" x 9" black and white photographic prints are available for any photographs or illustrations appearing in this copy for an additional charge. Contact UMI directly to order.**

**Bell & Howell Information and Learning  
300 North Zeeb Road, Ann Arbor, MI 48106-1346 USA  
800-521-0600**

**UMI<sup>®</sup>**



**TIME-DEPENDENT ELECTRON TRANSPORT AND  
OPTICAL EMISSIONS IN THE AURORA**

**A  
THESIS**

**Presented to the Faculty  
of the University of Alaska Fairbanks  
in Partial Fulfillment of the Requirements  
for the Degree of**

**DOCTOR OF PHILOSOPHY**

**By**

**Laura Marie Peticolas, B.A.**

**Fairbanks, Alaska**

**August 2000**

**UMI Number: 9985512**

**UMI<sup>®</sup>**

---

**UMI Microform 9985512**

**Copyright 2000 by Bell & Howell Information and Learning Company.**

**All rights reserved. This microform edition is protected against  
unauthorized copying under Title 17, United States Code.**

---

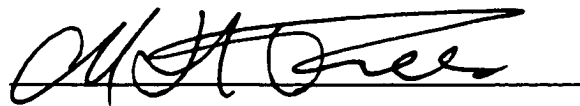
**Bell & Howell Information and Learning Company  
300 North Zeeb Road  
P.O. Box 1346  
Ann Arbor, MI 48106-1346**

**TIME-DEPENDENT ELECTRON TRANSPORT AND OPTICAL  
EMISSIONS IN THE AURORA**

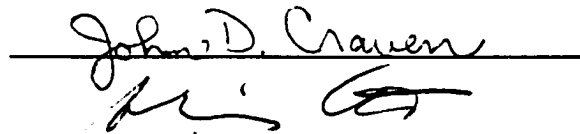
By

**Laura Marie Peticolas**

RECOMMENDED:



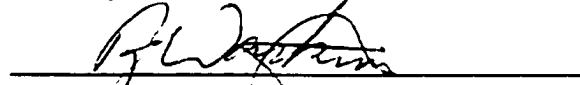









**Advisory Committee Chair**



**Department Head**

APPROVED:



**Dean, College of Science, Engineering and Mathematics**



**Dean of the Graduate School**



**Date**

# Abstract

This thesis presents the first time-dependent transport model of auroral electrons. The evolution of the spherical electron intensity in phase space is studied for a variety of incident electron intensities. It is shown that the secondary electrons with energies  $< 10$  eV and at altitudes  $> 150$  km can take over 300 ms to reach steady state in phase space. Since there are bright optical emissions in this region, such a time dependence in the auroral electrons is important.

The emissions of  $N_2(2PG)$  3371 Å and  $N_2^+(1NG)$  4278 Å are studied for time-varying electron pulses to show for the first time that this ratio will change until the secondary electrons reach steady state in the ionosphere. The way in which the 3371Å/4278Å ratio changes with time-varying precipitation depends on the precipitating electron spectra. The changes in the emission ratio can be used to learn more about the auroral acceleration region and the role of the ionosphere in auroral emissions.

Field-aligned bursts (FABs), often observed in electron spectra of instruments flying over flickering aurora, are modeled with the time-dependent transport model. How the ionosphere modifies these electrons is shown. The 3371 and 4278 Å emissions of flickering FABs are modeled to study the optical effects of modulated electron intensities in time. A study of 4278 Å emissions for electron source regions from 630 to 4,000 km are studied along with frequency variations from 5 to 100 Hz. This study shows that the percent variation of the maximum to the minimum column brightness is less for higher frequencies and more distant source regions. It is shown that with an accurate time-dependent transport calculation and 4278 Å emission observations of flickering aurora it should be possible to deduce the source altitude of the modulated electrons creating the optical flickering.

# Contents

List of Figures . . . . .	vi
List of Tables . . . . .	viii
Acknowledgements . . . . .	ix
<b>1 Introduction</b>	<b>1</b>
1.1 Solar Terrestrial Physics . . . . .	2
1.2 The Thermosphere and Lower Ionosphere . . . . .	8
1.3 Transport Theory for Rapidly Varying Aurora . . . . .	12
<b>2 The Time-Dependent Auroral Electron Transport Equation</b>	<b>16</b>
2.1 The Transport Equation . . . . .	18
2.1.1 Basic Assumptions . . . . .	18
2.1.2 Derivation of the Transport Equation . . . . .	19
2.2 Difficult Aspects of the Transport Equation . . . . .	25
<b>3 Solution to the Time-Dependent Transport Equation</b>	<b>31</b>
3.1 The Equation Revisited . . . . .	32
3.1.1 Further Assumptions . . . . .	32
3.1.2 Final Equations . . . . .	35
3.2 Method of Solution . . . . .	36
3.2.1 Evaluating Important Functions . . . . .	36
3.2.2 Numerical Discretization . . . . .	38
3.2.3 Solution Accuracy . . . . .	42
3.3 Time-Dependent Solutions . . . . .	57

<b>4</b>	<b>Time-Dependent Emission Rates</b>	<b>69</b>
4.1	Modeling Emissions . . . . .	70
4.2	Emission Ratios . . . . .	80
<b>5</b>	<b>Field-Aligned Bursts of Electrons in Flickering Aurora</b>	<b>86</b>
5.1	Field-Aligned Bursts of Electrons . . . . .	87
5.1.1	Emission Rates . . . . .	95
5.2	Discussion . . . . .	101
<b>6</b>	<b>Summary and Conclusions</b>	<b>106</b>
6.1	Summary . . . . .	106
6.2	Discussion and Future Research . . . . .	108
<b>A</b>	<b>Relating Electron Functions in Phase Space</b>	<b>112</b>
	<b>Bibliography</b>	<b>116</b>



# List of Figures

1.1	A diagram of the magnetosphere and its regions from <i>Kelley</i> [1989]. . . . .	3
1.2	Electron spectra taken by the FAST satellite. . . . .	5
1.3	Atmospheric temperature and density profiles . . . . .	10
3.1	Total cross sections. . . . .	33
3.2	Altitude and energy grids used in this thesis. . . . .	39
3.3	Errors from the numerical energy discretization. . . . .	43
3.4	Comparing transport calculations. . . . .	45
3.5	Spherical electron intensities for three beams of electrons. . . . .	46
3.6	Ionization rates for three beams of electrons. . . . .	49
3.7	700-eV field-aligned monoenergetic electron beam comparisons. . . . .	51
3.8	2-keV field-aligned monoenergetic electron beam. . . . .	52
3.9	1-keV field-aligned Maxwellian electron beam comparisons. . . . .	53
3.10	10-keV field-aligned monoenergetic electron beam. . . . .	54
3.11	Time evolution of a 700-eV field-aligned Gaussian intensity. . . . .	59
3.12	Time evolution of a 10-keV field-aligned Gaussian intensity. . . . .	60
3.13	Time evolution of a downward isotropic 2-keV Gaussian intensity. . . . .	61
3.14	Time evolution of a field aligned 2-keV Gaussian intensity. . . . .	62
3.15	Time evolution of a field-aligned 1-keV Maxwellian intensity. . . . .	63
3.16	The time to reach steady state. . . . .	67
4.1	Molecular Nitrogen Grotrian Diagram . . . . .	73
4.2	4278 Å and 3371 Å emission rates from a 2-keV Gaussian, field-aligned beam. . . . .	76

4.3	4278 Å and 3371 Å emission rates from 1-keV Maxwellian, field-aligned beam.	77
4.4	4278 Å and 3371 Å emission rates from 2-keV Gaussian, isotropic beam. . .	78
4.5	4278Å and 3371Å column emission rates for three beams. . . . .	79
4.6	$N_2(2PG)/N_2^+(1NG)$ time-dependent ratio. . . . .	81
4.7	4278Å emission for five different spectra. . . . .	83
5.1	Modulation of the initial differential flux. . . . .	89
5.2	The differential flux for 5-Hz-modulated FABs. . . . .	91
5.3	The differential electron flux at 502 km. . . . .	92
5.4	The differential electron flux at 153 km. . . . .	93
5.5	Optical emissions from FABs modulated at 5 Hz from 4000 km. . . . .	96
5.6	Optical emissions from FABs modulated at 100 Hz from 4000 km. . . . .	97
5.7	$N_2(2PG)$ 3371 Å to the $N_2^+(1NG)$ 4278 Å emission ratio. . . . .	99
5.8	Brightness variations in 4278 Å. . . . .	103
A.1	The geometry for a differential electron flux detector. . . . .	113

# List of Tables

1.1	Several neutral emissions observed in the aurora. . . . .	12
1.2	Rapid variations in aurora and electron transport. . . . .	14

# Acknowledgements

First and foremost I would like to thank my advisor, Dr. Dirk Lummerzheim, for giving me the freedom to make my own mistakes as well as permission to pester him endlessly with all types of questions. Not only has he helped me to understand phase space and the transport equation, he has shown me what it means to do what I enjoy and to enjoy what I do. He also helped me to choose a sensible and qualified committee: Professors Hans Stenbaek-Nielsen, Antonius Otto, John Craven, Manfred Rees and Roger Smith.

Hans Stenbaek-Nielsen was extremely helpful in reminding me of the reality of the aurora. He gave me unforgettable opportunities to teach, fly in jets, work in Kaktovik, work with FAST data and meet scientists from outside Alaska. Antonius Otto was a life-saver when it came to trying to sort out the numerical complications involved in this thesis and I enjoyed our many discussions about Earth's Magnetosphere and Ionosphere and their coupling. John Craven was the first to teach me space physics, how the measurements and theory of particle data relate and he has taught me an incredible amount of English in the last two months. I would like to especially thank Fred Rees for getting me started on solving the transport equation. He was also very helpful with the discussions involving emissions in this thesis. And I would like to thank Roger Smith for being a great teacher (in auroral physics) and for always finding the time to learn about my research. Although Tom Hallinan was not on my committee, he was always available to teach me about optical measurements and what to do with the video data once I had it.

Since *Truffer* [1999] pointed out that one does not need to be brief in the acknowledgements, I will take his lead and continue to acknowledge the many people who have made this thesis possible. Of all the staff at the Geophysical Institute, four people stood out as being extra helpful and kind to graduate students, and to me in particular: Dave Covey, Anne Trent, Penelope Noecker, and Delores Baker. They made my life easier and more fun when I had to deal with computers, travel, keys and room arrangements.

I'd also like to thank the NASA Graduate Student Researchers Program for funding the last years of my thesis work under grant number NGT5-50191.

I've never connected with so many people until I came to Alaska and I want to thank all of them! So, I am going to try... With Dana's Cosmology books - thanks Dana! - and

with our tensor analysis books, Martin and I kept our love of physics (besides the aurora and glaciers) alive. When the transport equation seemed dull and uninspiring, Martin was always there to do fun physics problems with me. Peter and Veronika were not only dear friends, but the graduate students I talked to most about the aurora and my code. Andrea, Heavner, Fred and I studied for hours together for our comps, which continued after with the physics problem list! And not only did I enjoy doing physics problems with Heavner, he was my main teacher when it came to Linux - my favorite operating system! Matt and Curt, look: 128 pages!! Dana was always there to solve the math after I got stuck. And she kept me going with cards, presents and food during comps, writing the thesis, and the defense. Jeffrey helped to get me through the first two years of classes and continued to keep my mind thinking hard about all sorts of things afterwards. Fred helped with all sorts of odds and ends and was a constant companion in the late night hours, along with Karen. Besides baking me bread, Ryan spent hours listening to me practice my thesis defense and helping me make it better and Bevin spent hours getting me started with Powerpoint.

Knitting kept me sane in the winters with Dorte, Jen and Seth, Jen and Peter, Bill and Maggie and frisbee kept me sane in the summers with Look At Them Beans and the Potlatch tournament. Michael and Marion, besides being Eno's God parents, were beautiful friends. It takes a village to raise a child and we had that village in Crane Court with Lisa, Dave, Dakota, Raven, Storm, Matt, Carrie, Jen, Peter, Willis, Darcy, Ryan, Hilary, Doerte, and the folks in the trailer, who reminded me of how lucky I am. Along with Hans, Krynicki, Curt, Alice, and Alice's parents, these people were my family here in Fairbanks. And of course, I could not have made it here without the support from my family from the very beginning, especially from my mom and dad. Carrie, Bevin and Veronika were my biggest support. Veronika listened every Tuesday to all my problems, both personal and in physics. She really helped me get through the last year. I would not have made it through the winters without Carrie and her zest for life, her ever patient ear and our long walks day after day. Bevin has been an incredible friend, helping me to grow faster than I ever have before - I'm so tall now! And last, but certainly not least, I would like to thank my husband, Tom, for his support. He was here in the beginning in Electrodynamics, and at the end, during the time of the defense. He has made my physics career and my life more complete. I am ready for our next adventure together!

# Chapter 1

## Introduction

On dark winter nights in Fairbanks, Alaska, one can often see to the north an elongated steady band of glowing whitish-green light in the sky stretching from the west to the east. Other times, its display is more lively with green and red dancing lights. Even more rare and often lower in latitude, a deep blood-red glow can fill the night sky. These displays are known as the Northern Lights, or Aurora Borealis, when seen in the Northern Hemisphere. In the Southern Hemisphere, these types of glowing displays are termed the Aurora Australis and the phenomena in general is simply called the aurora.

Thousands of years before we knew about the solar wind, Earth's magnetic field, the ionosphere, and the thermosphere, people saw the red glow of low-latitude aurora and others saw the dynamic green arcs in the high latitudes and they wondered: are heavenly spirits trying to communicate with us? We now understand that the various auroral displays we see from the ground are due to the solar wind's interaction with the magnetosphere, the currents thus generated, and charged particles accelerated along Earth's magnetic field to the upper atmosphere, where they collisionally excite the atoms and molecules that emit photons over a wide range of wavelengths. When it comes to understanding the details of the acceleration mechanism, the dynamics, the energy deposition into the atmosphere, and the atmospheric response to this energy, there are still many unanswered questions. The processes involved are complicated: electromagnetic interactions between particles, fields, and currents; the collisional processes in the ionosphere; and the large variations in time and length scales that appear in the many shapes and forms of the optical aurora.

In order to better understand the dynamics of the discrete aurora it is important to understand the physics of auroral arc formation and the atmospheric transport of auroral electrons. The modeling of these two processes enables us to understand the acceleration of precipitating electrons and the modification of the electrons' distribution function in phase space as well as the effect of the precipitating electrons on the temporal and spatial changes of emission rates and local ionospheric properties (conductance, temperature, and composition). The subject of this thesis covers the effect of precipitating electrons on the ionosphere during rapidly changing discrete auroral displays on millisecond time scales. Such effects have not been examined before largely due to the lack of instruments that could sample with sufficient time resolution as well as the lack of computational resources needed to solve the time-dependent transport equation numerically. However, in recent years there have been new instruments built to look at the aurora with millisecond time resolution [*Sakanoi and Fukunishi, 1999; Arnoldy et al., 1999; McHarg et al., 1998; Carlson et al., 1998*], and at the same time there has been an exponential growth in computer CPU speed. These advances in technology have made this thesis possible.

This first chapter provides a brief description of the electrons involved in creating night time discrete arcs from the plasma sheet to the acceleration region to the upper atmosphere. An overview of the upper atmosphere and lower ionosphere is then given. Finally three types of rapidly varying aurora are discussed along with the need for a time-dependent electron transport calculation for such aurora.

## 1.1 Solar Terrestrial Physics

The aurora is seen primarily at high latitudes because of the topology of Earth's magnetic field. At the present time, Earth's self-generated large-scale magnetic field at the surface is dominated by a magnetic dipole with its magnetic south pole in the Northern Hemisphere and its magnetic north pole in the Southern Hemisphere. However, Earth is embedded in the extended, expanding coronal atmosphere and magnetic field of the Sun. This magnetized plasma, called the solar wind, flows past all planets in our solar system, carrying with it the Sun's magnetic field, known as the interplanetary magnetic field (IMF). The solar wind has mass and momentum, and its dynamic pressure compresses Earth's magnetic

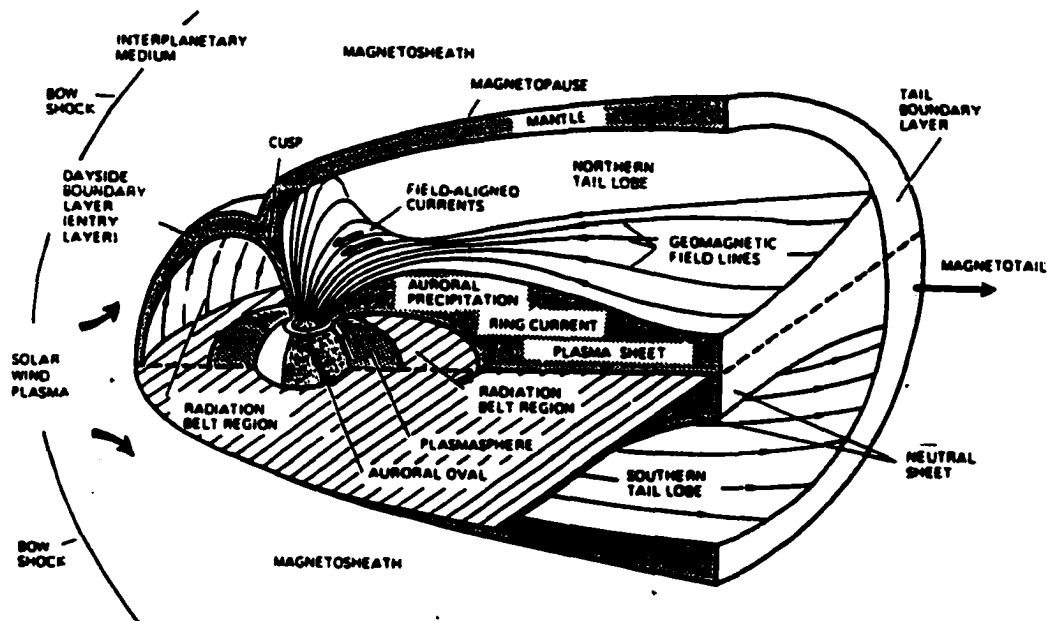


Figure 1.1. A diagram of the magnetosphere and its regions from *Kelley [1989]*.

field on the day side and elongates it on the night side. The bounded magnetic field region and its currents and plasma are known collectively as Earth's magnetosphere. The boundary between the magnetosphere and the solar wind is called the magnetopause and the elongation on the night side is referred to as the magnetotail. Figure 1.1 shows a drawing of the magnetosphere and some of its regions. The electrons particularly important to nighttime discrete arc formations are believed to travel along the magnetic field from the plasma sheet to the upper atmosphere.

The near-earth plasma sheet ( $10-30 R_e$ ), shown in Figure 1.1, is filled with particles from both the solar wind and the ionosphere. Ionospheric oxygen ions,  $O^+$ , and singly ionized helium ions,  $He^+$ , from the ionosphere populate the plasma sheet during active auroral displays while hydrogen ions and doubly ionized helium ions,  $He^{++}$ , are brought into Earth's magnetosphere from the solar wind through a combination of transport processes:



reconnection of the IMF and Earth's magnetosphere and convection through the lobes and the mantle to the plasma sheet [Hultqvist *et al.*, 1999, chap. 6]. The density of the plasma in this region is high compared with the surrounding boundary layers, ranging from 0.1 to 2  $\text{cm}^{-3}$  [Zwickl *et al.*, 1984; Lennartsson, 1992]. The electrons are often isotropic and hot with temperatures ranging from 0.1-0.7 keV [Zwickl *et al.*, 1984; Paterson and Frank, 1994]. Ion diamagnetic drifts make up the cross tail current and the electric field, i.e.  $\frac{\vec{E} \times \vec{B}}{B^2}$ , convection drifts move plasma anti-sunward in the plasma sheet during reconnection [Hultqvist *et al.*, 1999]. These drifts are typically less than the ion thermal velocities and make up the average convection patterns in the plasma sheet [Wolf, 1997]. Plasma bursty bulk flows (BBFs) are short lived bursts of plasma in the plasma sheet with average flows (100  $\text{km s}^{-1}$  or more) that have been measured to flow earthward near midnight, from the distant magnetotail ( $> 30 R_e$ ) [Angelopoulos *et al.*, 1994]. These BBFs have also been observed drifting around Earth in the stronger dipolar magnetic field regions from 8-15  $R_e$  [Hultqvist *et al.*, 1999].

Electrons move from the plasma sheet along the magnetic field to the auroral oval, the global distribution of auroral emissions within the ionosphere. This oval surrounds the magnetic pole and changes size in response to large-scale global magnetic perturbations. Above this region, primarily in the evening sector and from altitudes between 3000 to 15000 km, upward electric fields parallel to the magnetic field have been measured [Wescott *et al.*, 1976; Mozer *et al.*, 1977; Stenbaek-Nielsen *et al.*, 1984; Marklund, 1993; Carlson *et al.*, 1998]. Because these fields accelerate electrons to high energies as they travel toward the upper atmosphere, this region is known as the acceleration region. The acceleration region is one of the most complex regions in the magnetosphere-ionosphere (M-I) system, important in the coupling of the M-I system and the formation of discrete auroral arcs. M-I coupling, the acceleration mechanism, ion composition and dynamics, and plasma waves have been studied extensively in this region [Lundin *et al.*, 1994; Akasofu and Kan, 1981; Lysak, 1993; Carlson *et al.*, 1998; Hultqvist *et al.*, 1999]. However, this thesis is concerned primarily with precipitating electrons and their interaction with the upper atmosphere, such that the acceleration region will only be discussed in the context of its effect on the electrons' angular distributions and energy spectra.

The existence of parallel electric fields in the acceleration region was first deduced from electron spectra measured with instruments on board rockets and satellites [Evans, 1968,

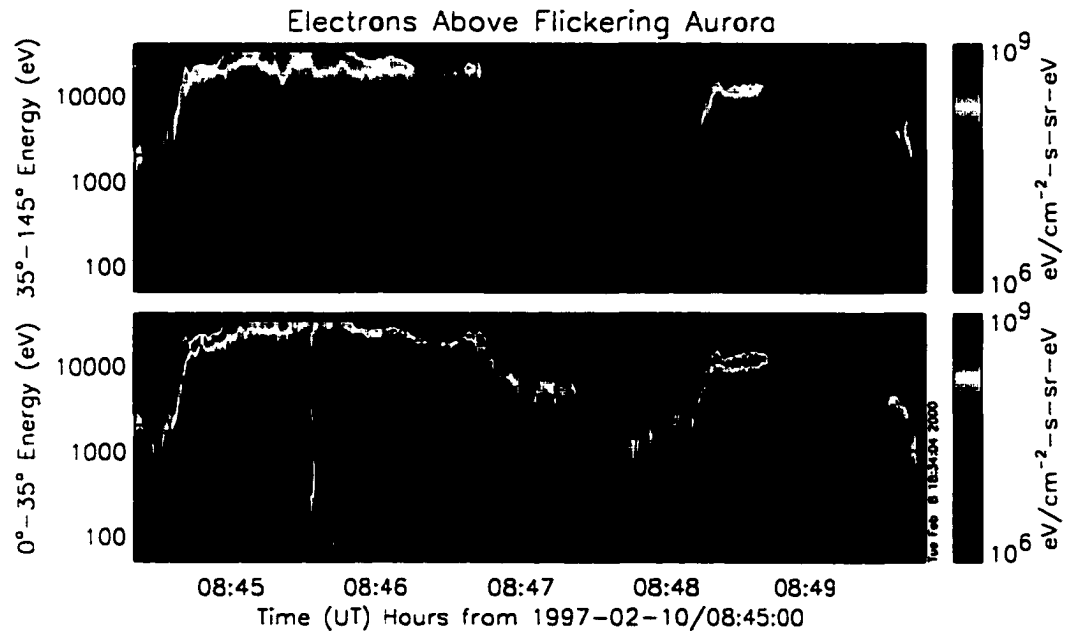


Figure 1.2. Electron spectra taken by the FAST satellite. The satellite traversed above flickering discrete arcs in the Northern Hemisphere at  $\sim 3800$  km altitude. Shown in this figure are two inverted-V energy spectrums along with field-aligned bursts shown as streaks of flux from high energies to low energies.

1974; *Mozer et al.*, 1977] traveling below the acceleration region. These electron spectra showed monoenergetic electron fluxes increasing in energy with latitude until some maximum energy was reached and then decreasing back to low energies, forming an upside down “U” or “V” in peak energy flux [*Frank and Ackerson*, 1971]. These types of spectra have ever since been called “inverted-V electron spectra” and the electrons undergoing the acceleration to form such a spectra are called “inverted-V electrons”. An example of such spectra is shown in Figure 1.2 from the FAST satellite at altitudes from 3900 to 3700 km. These inverted-V electrons have been shown to correspond well in latitude with auroral arcs observed below the inverted-V if the energy flux is sufficient to create observable emissions [*Meng*, 1981; *Fennell et al.*, 1981; *Bryant*, 1981; *Stenbaek-Nielsen et al.*, 1998].

The electrons that form the inverted-V signature in and below the acceleration region are generally isotropic in pitch angle with the exception of a well defined loss cone for the largest pitch angles. [*Arnoldy*, 1981]. On the edges and occasionally in the middle of an

inverted-V, field-aligned electron distributions are found at pitch angles less than  $20^\circ$ . These electrons are less energetic than the monoenergetic electrons, often with fluxes distributed over a wide range of energies [*Lin and Hoffman, 1979a*]. These incident electrons appear as vertical streaks in energy spectra at energies below the inverted-V energy, as seen in Figure 1.2; they are especially clear near 8:45:30 UT. Field-aligned electrons are measured more often during active auroras [*Arnoldy, 1981*]. Counter-streaming electron beams are observed below the acceleration region. These electrons are similar to the electron bursts mentioned above. They have a broad energy spectrum up to 1 keV and are field aligned with both an upward and a downward field-aligned components [*Sharp et al., 1980; Lundin and Eliasson, 1991*]. Another type of electron distribution observed below the acceleration region are low-energy electrons for which the flux increases as the energy decreases to energies less than 1 keV. The low-energy electron spectra can be fitted to a power law,  $E^{-\gamma}$ , where  $\gamma$  varies between 1 and 2 [*Reasoner and Chappell, 1973*] and are generally isotropic. They are believed to be trapped secondary electrons created from ionizations in the ionosphere, back-scattered upward, and then reflected by the electric field in the acceleration region [*Evans, 1974; Pulliam et al., 1981*].

Most of the electrons discussed above either precipitate into the upper atmosphere or the upper atmosphere modifies their distribution function in energy, pitch angle, and altitude through ionization and scattering processes. Backscattered electrons change the electron distribution functions measured just below the acceleration region as mentioned above. The electrons that precipitate into the upper atmosphere are primarily responsible for the optical aurora. These electrons follow the magnetic field lines down into the atmosphere where they collide with the neutral atmosphere to produce light. Thus the electrons produce a visual trace of the magnetic field. Hence many auroral forms have a curtain appearance. Besides this curtain appearance the visual aurora has many shapes, sizes, and motions. Cameras observing different types of optical aurora, such as discrete arcs, diffuse aurora, black aurora, pulsating aurora, and enhanced aurora [*Stoermer, 1955; Hallinan, 1991; Chamberlain, 1995*] help to provide information regarding the physics behind a particular aurora.

Discrete aurora, such as an arc that is seen as a band of light stretching east-west across the sky, are formed by electrons accelerated by the parallel electric field discussed above. Discrete arcs range in width from tens of kilometers to hundreds of meters [*Gorney, 1991*].

The manner in which these arcs move must be related to the the acceleration process in the acceleration region and the current system driven by convection in the magnetosphere. Often, discrete arcs are observed to flicker. Flickering aurora is a type of auroral display in which the brightness of  $\sim 5$  km spots of optical intensity within a discrete arc modulates at frequencies from 2-20 Hz [Beach *et al.*, 1968; Berkey *et al.*, 1980; McFadden *et al.*, 1987] to over 100 Hz [McHarg *et al.*, 1998]. Field-aligned burst of electrons, mentioned above, have been detected by instruments on-board rockets and satellites passing above flickering aurora [Spiger and Anderson, 1985; McFadden *et al.*, 1987; Lund *et al.*, 1995; Arnoldy *et al.*, 1999]. The spectrum shown in Figure 1.2, for example, was measured while the FAST satellite traversed flickering aurora in a discrete arc as observed by cameras below the aurora Hallinan *et al.* [1997].

Besides moving and flickering, discrete arcs can have kinks and bends in their form across the sky which are often quasi-periodic along the arc [Hallinan, 1991]. Structures with wavelengths around 10-50 km are called folds. These folds often have horizontal velocities up to 5 km/s. Structures with wavelengths between 1-9 km, as observed in the magnetic zenith, are called curls [Hallinan and Davis, 1970]. Curls have faster horizontal velocities than folds, reaching speeds as high as 20 km/s [Hallinan and Davis, 1970]. When viewed from the side, arcs with curls or folds can look like rays, much as semi-transparent window curtains can look when they have folds in them. These types of arcs are generally called rayed arcs. Rapid ray motions in these rayed arcs, such as those seen by Wescott *et al.* [1993], are associated with the horizontal velocities of curls seen in the magnetic zenith.

There are two other types of discrete auroral rays that do not make up a rayed arc and may not be related to curls. Auroral rays can appear in a bundle or sometimes a single ray will appear by itself [Chamberlain, 1995]. Tall, stationary rays are also observed. The luminosities of these types of rays extend over several hundred kilometers [Stoermer, 1955]. These tall rays are quite different from the rapidly moving rays associated with curls and thin arcs and presumably related to different types of electron spectra and currents [Zhu, 2000].

Discrete arcs are often made up of filamentary arcs with widths of  $<1$  km [Maggs and Davis, 1968; Borovsky *et al.*, 1991; Lanchester *et al.*, 1994, 1997; Trondsen, 1998]. Maggs and Davis [1968] were the first to measure the width of auroral forms in discrete and diffuse

aurora as thin as 70 m (their video resolution). In this thesis, thin arcs with widths of  $\sim 100$  meters will be called "auroral filaments" to differentiate them from arcs with thickness of several kilometers. The importance and general lack of knowledge of small-scale auroral processes was demonstrated by *Borovsky* [1993] when he examined 22 auroral acceleration mechanisms in order to ascertain if any would produce auroral filaments. None of the existing theories in Borovsky's review could produce such filaments. Since Borovsky's paper there have been new theories to address the thinness of the observed auroral filaments [e.g., *Otto and Birk*, 1993] and high-time-resolution measurements have been placed on board polar orbiting satellites, such as the Freja and FAST satellites [*Lundin et al.*, 1994; *Carlson et al.*, 1998]. The effect of such filaments on the ionosphere as well as the magnetosphere-ionosphere coupling of such small-scale structures is an active research area [*Lanchester et al.*, 1994, 1997; *Zhu et al.*, 2000].

## 1.2 The Thermosphere and Lower Ionosphere

The emission rate altitude profiles are dependent on the neutral density profiles in the upper atmosphere. If the neutral densities change, the appearance of the aurora could potentially change. The ionosphere and upper atmosphere are also important in M-I coupling since ionization created by electron precipitation will change the electron number density and thus the conductivity. Changes in the conductivity are important to magnetospheric dynamics as well as to the ionospheric currents which heat the atmosphere by Joule heating. The upper atmosphere is also important in M-I coupling, as mentioned above, since precipitating and secondary electrons scatter off its molecules and atoms back into the near-Earth magnetosphere.

To first order, gravity causes the atmosphere to be horizontally stratified with density exponentially decreasing with altitude. Each atmospheric region is defined by its vertical temperature profile since the temperature of the region defines much of the physics and dynamics. Temperature profiles for the atmosphere over Fairbanks, AK ( $65^\circ$  N,  $212^\circ$  E geographic) at 10 LT and 22 LT are shown in Figure 1.3 for a moderately active auroral period. The mass spectrometer incoherent scattering (MSIS) [*Hedin*, 1991] atmospheric model was run to produce these profiles. We live in the troposphere, where the temperature

decreases in altitude by approximately 7 K/km [Kelley, 1989]. Above the troposphere is the stratosphere (~15-50 km) where the atmospheric temperature increases due to a layer of ozone in this region that strongly absorbs ultraviolet light (2400-2900 Å) [Solomon, 1990]. Above this layer is the mesosphere (~50-85 km), where radiative cooling decreases the temperature [Kelley, 1989]. The thermosphere lies above the mesosphere and is defined by a final large increase in temperature. The sources for the temperature increase in this region are the sun's ultraviolet (< 1750 Å) light, the precipitating auroral particles and the currents which are driven by magnetospheric convection [Rees, 1989].

The lower atmosphere, below 100 km, is made up of a homogeneous mixture: approximately 78 % N<sub>2</sub>, 20 % O<sub>2</sub>, and numerous lesser constituents. Above 100 km, in the thermosphere, collisions become less frequent and the atmospheric species begin to separate according to their mass in near diffusive equilibrium. This effect can be seen in Figure 1.3, where the N<sub>2</sub>/O<sub>2</sub> density ratio increases above 100 km and atomic oxygen becomes the dominant species above 350 km. In the thermosphere, solar UV light and auroral precipitation ionize a small fraction of the neutral atmosphere to produce the ions and electrons which make up the plasma of the ionosphere.

The plasma density in the ionosphere is a balance between the ionization sources and recombination losses, which occurs through chemical reactions. The UV radiation from the sun photoionizes the neutral species on the day side, creating a relatively constant plasma source within the day-side ionosphere. Auroral precipitation is a highly variable source, ionizing neutral atoms and molecules through electron impact ionization in the high latitude ionosphere. The loss of the ionospheric plasma density through recombination is altitude dependent resulting in several peaks in electron densities at different altitudes: one at ~250 km (the F Region), one at ~100 km (the E Region), and occasionally one at ~85 km (the D Region). Atomic oxygen ions are the dominant ion species in the F Region. In the night-time ionosphere, this plasma density can remain for hours after the sun has set since the recombination of O<sup>+</sup> in the F Region occurs through radiative recombination which proceeds at a very slow rate ( $k \approx 3 \times 10^{-12}$  cm<sup>3</sup>/s). The main ions in the E Region are NO<sup>+</sup> and O<sub>2</sub><sup>+</sup>. These ions disappear in a matter of seconds at night since molecular

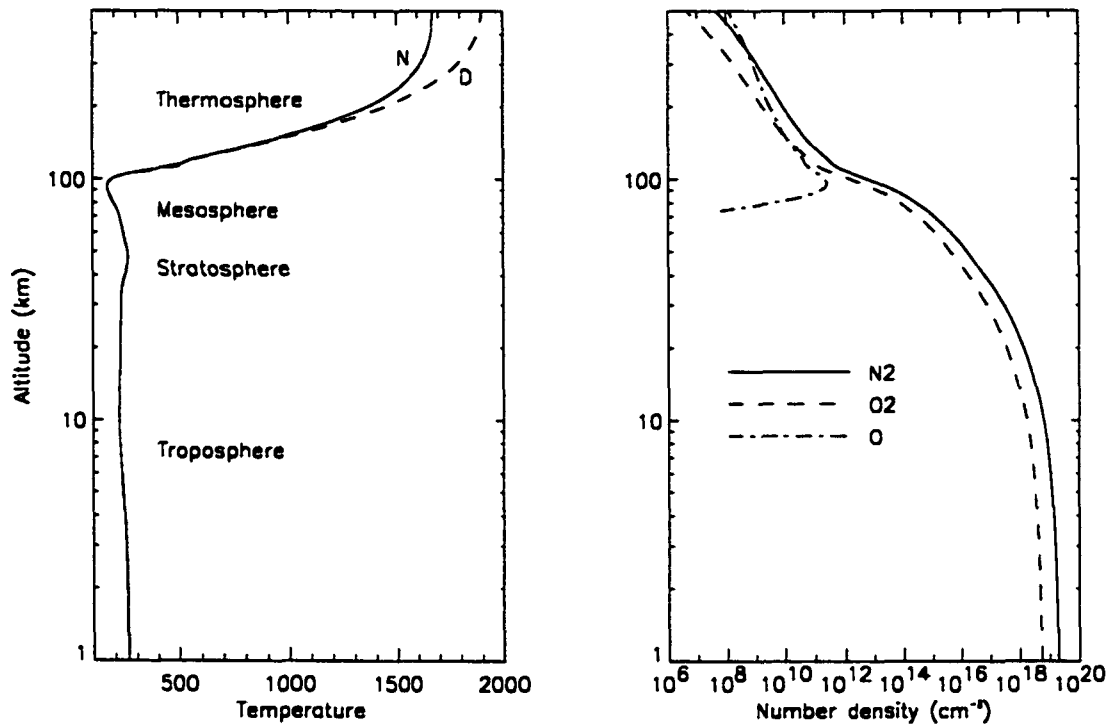


**Figure 1.3. Atmospheric temperature and density profiles. On the left, typical profiles of neutral atmospheric temperature are plotted with each region marked. The solid line represents the night-time profile and the dashed line represents the day-time profile. On the right the densities of the major species, N<sub>2</sub>, O<sub>2</sub> and O are shown. These values come from the mass spectrometer incoherent scattering (MSIS) [Hedin, 1991] atmospheric model for day 90 in 1998 with an AP of 200 and a F10.7 of 200.**

species have a faster recombination rate. For example,  $\text{NO}^+$  recombines through dissociative recombination in the E Region which has recombination rate,  $k$ , of  $\sim 3 \times 10^{-7} \text{ cm}^3/\text{s}$  [Chamberlain, 1978]. In the night-time auroral ionosphere, precipitating electrons ionize O,  $\text{O}_2$  and  $\text{N}_2$  to produce a significant plasma density below the F Region peak density.

The chemistry of the upper ionosphere is important in understanding both the neutral and ionized constituents in this region. After an intense auroral display the density of nitric oxide, NO, can increase by a factor of four [Solomon *et al.*, 1999]. This cannot be understood by simple recombination of  $\text{NO}^+$  since, as mentioned above,  $\text{NO}^+$  recombines dissociatively. Nitric oxide is a product of an ionization and two chemical-ionic reactions [Rees and Lummerzheim, 1991]. Auroral electrons (or solar soft x-rays [Barth *et al.*, 1999]) ionize  $\text{N}_2$  leaving  $\text{N}_2^+$ . Then dissociative recombination of  $\text{N}_2^+$  leads to the production of two neutral nitrogen atoms in excited states. These nitrogen atoms then react with  $\text{O}_2$  in an interchange reaction, producing nitric oxide and an excited state of atomic oxygen. Nitric oxide is not very reactive and has a lifetime of approximately a day in the upper atmosphere [Solomon *et al.*, 1999]. See Rees [1989] and references therein for a good review of this subject.

Solar radiation and auroral precipitation not only ionize and dissociate the neutral upper atmosphere, but they also excite species into electronic, vibrational and rotational quantum states. The species in these states then release energy either through photon emission or through energy transfer to another particle, resulting either in collisional de-excitation (quenching) or in a reactive collision. Table 1.1 gives some typically observed transitions, their lifetimes, the altitude below which they are quenched, and the threshold energy of the transition. The O green line (5577 Å) is well known in auroral studies because it is the brightest line in the visible auroral spectrum. This wavelength is also near the maximum sensitivity of the eye. The O red line (6300 Å) is also well known because it is the brightest emission above about 150 km. Because the lifetimes of these two lines are long (0.75 s and 134 s, respectively [Beluja and Zeippen, 1988]), it is difficult to obtain information from observations of these emissions on quickly varying sources in the upper atmosphere. It is thus common to measure  $\text{N}_2^+(1\text{NG})$  4278 or 3914 Å above 85 km since they are bright bands, have very short lifetimes, and the emission rates are directly proportional to the ionization rate, since the parent states of these emissions are excited when  $\text{N}_2$  is ionized.



Name	Upper State	Lower State	Lifetime	Quench Altitude	Threshold Energy
N <sub>2</sub> (1PG)	N <sub>2</sub> (B <sup>3</sup> Π <sub>g</sub> )	N <sub>2</sub> (A <sup>3</sup> Σ <sub>u</sub> <sup>+</sup> )	6 μs	53 km	7.50 eV
N <sub>2</sub> (2PG)	N <sub>2</sub> (C <sup>3</sup> Π <sub>u</sub> )	N <sub>2</sub> (B <sup>3</sup> Π <sub>g</sub> )	50 ns	30 km	11.18 eV
N <sub>2</sub> <sup>+</sup> (1NG)	N <sub>2</sub> <sup>+</sup> (B <sup>2</sup> Σ <sub>u</sub> <sup>+</sup> )	N <sub>2</sub> <sup>+</sup> (A <sup>2</sup> Π <sub>u</sub> )	70 ns	48 km	18.56 eV
N <sub>2</sub> <sup>+</sup> (Meinel)	N <sub>2</sub> <sup>+</sup> (A <sup>2</sup> Π <sub>u</sub> )	N <sub>2</sub> <sup>+</sup> (X <sup>2</sup> Σ <sub>g</sub> <sup>+</sup> )	14 μs	85-90 km	16.54 eV
N <sub>2</sub> (VK)	N <sub>2</sub> (A <sup>3</sup> Σ <sub>u</sub> <sup>+</sup> )	N <sub>2</sub> (X <sup>1</sup> Σ <sub>g</sub> <sup>+</sup> )	2 s	145 km	6.31 eV
O <sub>2</sub> <sup>+</sup> (1NG)	O <sub>2</sub> <sup>+</sup> (b <sup>4</sup> Σ <sub>g</sub> <sup>-</sup> )	O <sub>2</sub> <sup>+</sup> (X <sup>2</sup> Π <sub>g</sub> )	1.2 μs	60 km	18.2 eV
O (Green Line)	O( <sup>1</sup> S)	O( <sup>1</sup> D)	0.75 s	95 km	4.1 eV
O (Red Line)	O( <sup>1</sup> D)	O( <sup>3</sup> P)	134 s	250-350 km	1.95 eV

Table 1.1. Several neutral emissions observed in the aurora. These emissions come from neutral and ionized N<sub>2</sub> and O<sub>2</sub>. This table is modified from *Heavner* [2000] using *Lummerzheim* [1987] and *Vallance Jones* [1974].

Measuring the auroral optical spectra was one of the first techniques used to study the aurora. It remains an important and useful method of obtaining information regarding the upper atmosphere and the auroral electrons [*Vallance Jones*, 1991]. In such studies, it is important to understand how precipitating electrons excite the thermospheric constituents into various quantum states. For example, the brightness ratio between emissions at two different wavelengths may differ depending on the mean energy of the precipitating electrons exciting the relevant parent states.

### 1.3 Transport Theory for Rapidly Varying Aurora

The quantitative study of how precipitating auroral electrons collide with the neutral atmosphere is called auroral transport theory. Because there are billions of electrons per square centimeter per second entering the atmosphere, it is technically impossible to study individual electron interactions with the atmosphere. Instead it is possible to study the evolution of the electron distribution function or the electron directional differential flux (electron intensity) in phase space. The electron distribution function multiplied by a differential volume in phase space gives the number of electrons in this differential volume: i.e. with

a velocity between  $\vec{v}$  and  $\vec{v} + d\vec{v}$  and in a position between  $\vec{r}$  and  $\vec{r} + d\vec{r}$ . From the distribution function, many important ionospheric quantities can be derived such as ionization and emission rates of various atmospheric species. The electron intensity is defined as the number of electrons with kinetic energies between  $E$  and  $E + dE$  that travel through a solid angle cone  $d\Omega$  opening about a unit vector  $\hat{\Omega}$  and cross a surface area  $d\vec{A}$  (a counting device) perpendicular to  $\hat{\Omega}$ ,  $\hat{\Omega} \cdot d\vec{A}$ . See appendix A for a detailed discussion on intensities and distribution functions and the wide range of terminologies used.

The transport equation for auroral electrons has been solved using various techniques, as is discussed in detail in Chapter 2. All of these solutions of the auroral electron transport equation are steady state solutions. For most studies, the assumption that electrons reach steady state in phase space faster than the precipitating flux changes is sufficient. A time-dependent transport model for the auroral electrons becomes necessary when the steady-state-transport assumption breaks down, i.e. when the electrons and the secondaries produced in collisions do not reach a steady state before the incident particle flux changes. It is thus important to examine the time scales and spatial scales that make a time-dependent transport model important and specify in what type of auroras such a calculation would be needed.

As discussed in Section 1.1, auroral displays can contain extremely thin (<100 meters) arcs [Maggs and Davis, 1968; Borovsky et al., 1991; Lanchester et al., 1994, 1997; Trondsen, 1998], rapidly moving auroral rays [Chamberlain, 1995; Vallance Jones, 1974; Wescott et al., 1993], and flickering aurora [Beach et al., 1968; Berkey et al., 1980; McFadden et al., 1987; McHarg et al., 1998]. Understanding the formation and motion of these types of auroras means understanding the influence of the dynamic aurora on the thermosphere. Table 1.2 demonstrates that these types of auroral forms need to be modeled using a time-dependent transport equation for emission and ionization rates. The bottom three rows give the time it takes 100-eV, 500-eV and 5-keV electrons to become absorbed into the upper atmosphere; i.e. from 500 to 100 km. The time scales for electrons precipitating through 400 km are certainly of the same order as for quickly moving auroral filaments, auroral ray motions and flickering auroral arcs. With the plethora of new auroral observations and the newly developed theories for auroral arc formation, it has become apparent that current ionospheric transport models are unable to model the ionosphere's response to small-scale

<i>Auroral Form</i>	<i>Horizontal Velocity</i>	<i>Thickness</i>	<i>Time Scale</i>
Drifting arc filament <i>Lanchester et al. [1994]</i>	8 km/s	.1 km	.01 s
Auroral ray motions <i>Wescott et al. [1993]</i>	60 km/s	5 km	.08 s
Flickering Aurora <i>McHarg et al. [1998]</i>	NA	NA	.10 - .01 s
<i>Electron Transport</i>	<i>Vertical Velocity</i>	$\Delta$ <i>Height</i>	
.1 keV	5,900 km/s	400 km	.067 s
.5 keV	13,000 km/s	400 km	.030 s
5 keV	42,000 km/s	400 km	.0095 s

Table 1.2. Rapid variations in aurora and electron transport. The time it takes electrons of various energies to penetrate the atmosphere in which collisions become important is on the same order of magnitude as the time it takes various dynamic aurora to change location or luminosity in time.

auroral features on the time scales involved.

In this thesis, a time-dependent transport model is developed to study the electron intensities and ionization and emission rates for rapidly varying electron precipitation. In Chapter 2, the transport equation is derived and the difficulties involved solving it are discussed. A review of how others have solved different versions of the steady-state transport equation is given. In Chapter 3, the method of solving the time-dependent transport equation is discussed along with the assumptions and approximations necessary to solve the equation even in a limited form. Five types of different spectra are used as upper boundary conditions with which to study the intensity variations in phase space of a pulsed single-electron beam entering the upper atmosphere. In Chapter 4, the emission rates are studied for the five different cases to further examine the effect of the time dependence in the auroral electron equation. Ratios of  $N_2(2PG) 3371 \text{ \AA}$  to  $N_2^+(1NG) 4278 \text{ \AA}$  are also shown to change as a function of time as a pulse of electrons enters the atmosphere. In Chapter 5, field-aligned bursts (FABs) of electrons in flickering aurora are studied using the time-dependent transport code. The upper boundary electron intensities are modulated in time to simulate

flickering FABs at different frequencies and from different source heights. The results are discussed in light of rocket data published over the last twenty years. With these results, a technique is suggested with which optical measurements can be used to obtain an upper bound on the source altitude of the observed optical flickering aurora. Chapter 6 concludes the thesis with a summary of the results of Chapters 3,4 and 5, a discussion of future research involving the transport computer model and a discussion of experiments that should be done using observations at millisecond time scales to learn more about the aurora and time-dependent transport calculations.

## Chapter 2

# The Time-Dependent Auroral Electron Transport Equation

The most general study of large numbers of particles in non-equilibrium systems, such as the transport of auroral electrons, is known as non-equilibrium statistical mechanics. *Duderstadt* [1979] writes that “the primary goal of any theory of a many-particle system is to explain the macroscopic behavior of such a system in terms of the microscopic dynamics of the particles involved.” Three main techniques are used to study many-particle systems [*Duderstadt*, 1979]. The first technique is to study the microscopic dynamics of each particle in the system including its interactions with all other particles in the system. This type of study either involves studying the equation of motion for each particle or solving the Liouville equation for the probability density or ensemble density. This density is made up of all particles in the system for all systems that give the same macroscopic quantities when averaged over the microscopic quantities. Solving these microscopic equations is impossible for large numbers of particles. One level up from studying individual particle motion is to study the single-particle distribution function of a system in phase space. This type of study is known as kinetic theory and reduces the coupled equations in microscopic studies to a single equation in kinetic theory. The third type of statistical study involves studying the ensemble averages of various dynamical variables of interest. These averages are taken by multiplying either the ensemble density or the single-particle distribution function by the dynamical variable and integrating over velocity space. This study of the macroscopic

variables for a many-body system is known as hydrodynamic theory. The study of how a physical system can be understood stepwise from the microscopic to the hydrodynamic approach, is the study of non-equilibrium statistical mechanics.

As mentioned in Chapter 1, in order to deal with the large number of electrons precipitating into and colliding with the upper atmosphere, it is necessary to describe these particles by a single-particle distribution function,  $f$ . This function gives the probability of finding a certain number of electrons in a specific infinitesimal volume of configuration space and a specific infinitesimal volume of velocity space in a specific infinitesimal increment of time. The study of this electron distribution function is the subject of transport theory. Kinetic equations describe how this distribution function evolves in phase space and time for a population of particles in a physical environment. Kinetic theory deals primarily with the derivation of kinetic equations, as well as a study of the distribution function in general, whereas transport theory is a study of the solution of kinetic equations [Duderstadt, 1979]. The solutions to kinetic equations can provide information on the characteristics of a medium if the given distribution function is known, such as studying the densities of atmospheric species using measurements of an electron distribution function moving through the atmosphere. Alternatively, the solutions can allow one to study the distribution function knowing the properties of a specific medium, such as knowing the densities of atmospheric species and studying the electron distribution function as it moves through an atmosphere. It is the latter type of study that this thesis will address for auroral electrons traveling through a known part of the terrestrial upper atmosphere.

This chapter addresses the assumptions that are typically made for auroral electron transport theory. Using these assumptions the auroral electron transport equation is derived including time-dependence terms and external forces. After this derivation, the difficulties in solving such an equation are discussed along with a review of how some of these difficulties have been overcome to solve the steady-state transport equation. There are added difficulties that come with including the time dependence and/or an external, macroscopic force parallel to the magnetic field. These are also discussed.

## 2.1 The Transport Equation

### 2.1.1 Basic Assumptions

The Boltzmann equation is applicable for a system of gas particles not in equilibrium. In the formulation of this equation, from which the transport equation is derived, Boltzmann assumed that there are only short-range interactions among the gas particles, that the density of the gas is sufficiently low so only binary collisions occur, and time scales are long compared with the duration of a collision [Duderstadt, 1979]. These assumptions are also valid for the transport of auroral electrons: the collision interactions with the neutral atoms and molecules are short in range, electrons only collide with one atom or molecule at a time, and the duration of a collision is much shorter than mean time between electron-neutral collisions in the upper atmosphere.

The transport equation for auroral electrons differs from Boltzmann's original equation primarily because the incident precipitating electrons are assumed to not interact with one another; the collision rate between precipitating auroral electrons is small compared with the collision rate with neutral atoms, ions, and electrons. This makes the transport equation a linear version of the Boltzmann equation, i.e. the collision term is linear in the distribution function,  $f$ . External forces,  $\vec{F}$ , such as the magnetic mirror force or parallel electric fields, affect the transport or velocity of the electrons and are included in the transport equation

$$\frac{df}{dt} = \frac{\partial f}{\partial t} + \vec{v} \cdot \nabla f + \frac{\vec{F}}{m} \cdot \nabla_{\vec{v}} f = \left( \frac{\delta f}{\delta t} \right)_{\text{coll.}}, \quad (2.1)$$

where  $f = f(\vec{v}, \vec{x}, t)$  is the electron distribution function,  $t$  is time,  $\vec{v}$  is the vector velocity,  $\vec{x}$  is the position of the electron,  $m$  is the mass of the electron, and  $\left( \frac{\delta f}{\delta t} \right)_{\text{coll.}}$  is the collision term. The external forces are assumed to not be affected by the precipitating electrons in the lower ionosphere where the neutral collisions are dominant, making the transport equation linear with respect to the forces. Because of this, the transport equation represents the evolution of the distribution of test particles (electrons) in a given magnetosphere-ionosphere configuration where the electric and magnetic fields are known and Maxwell's equations are not needed.

In order to solve for the transport of auroral electrons, it is necessary to simplify the transport equation by continuing to make selective assumptions. First, it is assumed that

transport perpendicular to the magnetic field, such as the  $\vec{v}_\perp = \vec{E} \times \vec{B}$  drift, and that spatial gradients of the distribution function in the perpendicular direction are small compared to the transport and gradients in the parallel direction. This holds true for most auroral configurations where any perpendicular motion is parallel to the length of the arc where the gradients in  $f$  are small [Hallinan, 1991]. The equation can thus be solved in one spatial dimension,  $s$ , along the magnetic field. It is also assumed that forces on the electrons are only significant in the parallel direction; there are no perpendicular forces. For a homogeneous magnetic field there is an azimuthal symmetry in the velocity of the electrons, which follow spirals along magnetic field lines. Thus the equation in two velocity dimensions can be solved: perpendicular,  $v_\perp$ , and parallel,  $v_\parallel$ , to the magnetic field. It is also assumed that particle-wave interactions are negligible and that the electrons are moving slowly enough to ignore relativistic effects. For steady-state solutions to the auroral transport equation, the above assumptions are the ones typically made [e.g., Stamnes, 1978; Strickland et al., 1976; Solomon, 1993; Lummerzheim and Lilsten, 1994].

### 2.1.2 Derivation of the Transport Equation

Electron detectors measure the differential directional flux  $\frac{d^2j}{dE}$ , also known as the electron “angular intensity” (or “intensity”) in transport theory [Stamnes, 1977]. Transformations from an electron distribution function,  $f$ , to an intensity,  $I$ , is discussed in Appendix A. Because electron detectors measure the intensity as a function of energy,  $E$ , and pitch angle,  $\theta$ , if one wishes to compare theory with measurements it is necessary to transform the distribution function as a function of vector velocity to energy, pitch angle, and azimuthal angle. Appendix A also reviews the transformation of functions from one variable to another as well as the relationships between energy and angles and the vector velocities.

The assumption of azimuthal symmetry allows for the velocity vector to be represented by a perpendicular and a parallel velocity, which can be transformed to the electron’s kinetic energy,  $E = \frac{1}{2}mv^2$ , and pitch angle,  $\theta$ , with the assumption that the distribution function or intensity is symmetric or integrated over the azimuthal angle. The assumption that horizontal transport is small compared with transport parallel to the magnetic field means it is possible to integrate over the orthogonal perpendicular components, leaving a one-dimensional space component,  $s$ , along  $B$ . It is common to use the cosine of the



pitch angle,  $\mu = \cos\theta = \frac{v_{\parallel}}{v}$ , as a variable. With these considerations  $I = I(E, \mu, s, t)$  or  $f = f(E, \mu, s, t)$ . For completeness, the transport equation for the distribution function  $f = f(E, \mu, s, t)$  is a function of kinetic energy,  $E$ , cosine of the pitch angle,  $\mu$ , altitude along the magnetic field,  $s$ , and time,  $t$ . The electron transport equation for  $f$  is then transformed to the equation for the electron intensity,  $I(E, \mu, s, t)$ , which is equivalent to the measured quantity in experimental space physics:  $\frac{dj}{dE}$ .

Starting with Equation 2.1, first the distribution function must be transformed from velocity space to energy and cosine-of-the-pitch-angle space. The easiest way to make this transformation is to note that the left-hand side of Equation 2.1, the total derivative of the distribution function, can be rewritten using the chain rule:

$$\frac{df}{dt} = \frac{\partial f}{\partial t} + \frac{\partial f}{\partial s} \frac{ds}{dt} + \frac{\partial f}{\partial E} \frac{dE}{dt} + \frac{\partial f}{\partial \mu} \frac{d\mu}{dt} = \left( \frac{\delta f}{\delta t} \right)_{coll.} \quad (2.2)$$

where the variables are the same as in Equation 2.1 except those that were defined in the previous paragraph.

To obtain an equation that can be solved, it is necessary to explicitly determine the ordinary derivative terms in Equation 2.2:  $\frac{ds}{dt}$ ,  $\frac{dE}{dt}$ ,  $\frac{d\mu}{dt}$ , and  $\left( \frac{\delta f}{\delta t} \right)_{coll.}$ . The first of these derivatives is simply,

$$\frac{ds}{dt} = v_{\parallel} = \mu \sqrt{\frac{2E}{m}}. \quad (2.3)$$

The ordinary derivatives  $\frac{dE}{dt}$  and  $\frac{d\mu}{dt}$  are a little more complicated. The electrons experience a mirror force due to the converging magnetic field. This mirror force is not a true *parallel* force and thus the electron's total energy does not increase. Hence, the  $\frac{dE}{dt}$  and  $\frac{d\mu}{dt}$  terms for the mirror force must be treated differently than for a force that is parallel to the magnetic field, such as a parallel electric field. In both cases, the two derivatives are expanded in terms of the perpendicular and parallel velocity since azimuthal symmetry is assumed:

$$\frac{dE}{dt} = \frac{\partial E}{\partial v_{\perp}} \frac{dv_{\perp}}{dt} + \frac{\partial E}{\partial v_{\parallel}} \frac{dv_{\parallel}}{dt} = \frac{\partial E}{\partial v_{\perp}} v_{\perp} \dot{v}_{\perp} + \frac{\partial E}{\partial v_{\parallel}} v_{\parallel} \dot{v}_{\parallel}, \quad (2.4)$$

$$\frac{d\mu}{dt} = \frac{\partial \mu}{\partial v_{\perp}} \frac{dv_{\perp}}{dt} + \frac{\partial \mu}{\partial v_{\parallel}} \frac{dv_{\parallel}}{dt} = \frac{\partial \mu}{\partial v_{\perp}} v_{\perp} \dot{v}_{\perp} + \frac{\partial \mu}{\partial v_{\parallel}} v_{\parallel} \dot{v}_{\parallel}. \quad (2.5)$$

For a true parallel force,  $F_{\parallel}$ , such as an electric field there is no acceleration in the perpendicular direction, so  $\frac{dv_{\perp}}{dt}$  is zero and

$$\frac{dE_{F_{\parallel}}}{dt} = \frac{\partial E}{\partial v_{\parallel}} \dot{v}_{\parallel} = m v_{\parallel} \left( \frac{F_{\parallel}}{m} \right) = \mu \sqrt{\frac{2E}{m}} F_{\parallel}. \quad (2.6)$$

To calculate the total time derivative of  $\mu$ , write the partial parallel velocity derivative as

$$\frac{\partial \mu}{\partial v_{\parallel}} = \frac{\partial}{\partial v_{\parallel}} \left( \frac{v_{\parallel}}{(v_{\perp}^2 + v_{\parallel}^2)^{1/2}} \right) = \frac{v_{\perp}^2}{(v_{\perp}^2 + v_{\parallel}^2)^{3/2}} = \frac{1 - \mu^2}{\sqrt{\frac{2E}{m}}}, \quad (2.7)$$

from which it follows that

$$\frac{d\mu_{F_{\parallel}}}{dt} = \frac{(1 - \mu^2) F_{\parallel}}{\sqrt{\frac{2E}{m}} m} = \frac{(1 - \mu^2) F_{\parallel}}{\sqrt{2mE}}. \quad (2.8)$$

For the mirror force, the perpendicular acceleration term is non-zero because the total particle kinetic energy remains constant. This constraint yields the relation

$$v_{\perp} = -\frac{v_{\parallel} \dot{v}_{\parallel}}{v_{\perp}}. \quad (2.9)$$

Substitution of Equation 2.9 into the energy derivative in Equation 2.4 yields the expected result that this derivative is zero, for there is no energy lost or gained in the presence of the mirror force. The change in time of the cosine of the pitch angle is not zero, so the  $\frac{\partial \mu}{\partial v_{\perp}}$  term must be evaluated:

$$\frac{\partial \mu}{\partial v_{\perp}} = \frac{\partial}{\partial v_{\perp}} \left( 1 - \frac{v_{\perp}^2}{v^2} \right)^{\frac{1}{2}} = -\frac{v_{\perp} v_{\parallel}}{v^3}. \quad (2.10)$$

Combining equations 2.7 and 2.10 with the chain rule for  $\frac{d\mu}{dt}$  in Equation 2.5 results in

$$\frac{d\mu_{F_{\text{mirror}}}}{dt} = \left( \frac{\mu^2}{v} + \frac{1 - \mu^2}{v} \right) \dot{v}_{\parallel} = \frac{\dot{v}_{\parallel}}{v} = \frac{F_{\text{mirror}}}{\sqrt{2mE}}, \quad (2.11)$$

where

$$F_{\text{mirror}} = \frac{\dot{v}_{\parallel}}{m} = -\frac{v_{\perp}^2}{2B} \frac{\partial B}{\partial s} = -\frac{v^2(1 - \mu^2)}{2B} \frac{\partial B}{\partial s} \quad (2.12)$$

and  $B$  is the magnetic field [Jackson, 1975].

All relevant terms of  $\frac{df}{dt}$  have now been obtained, so inserting Equations 2.3, 2.6, 2.8, and 2.11 into Equation 2.2, yields

$$\frac{\partial f}{\partial t} + \mu \sqrt{\frac{2E}{m}} \frac{\partial f}{\partial s} + \mu \sqrt{\frac{2E}{m}} F_{\parallel} \frac{\partial f}{\partial E} + \frac{1}{\sqrt{2Em}} ((1 - \mu^2)F_{\parallel} + F_{\text{mirror}}) \frac{\partial f}{\partial \mu} = \left( \frac{\delta f}{\delta t} \right)_{\text{coll.}} \quad (2.13)$$

The collision term can be written as a loss term and a source term [Stamnes, 1978], with the primed variables representing the state of the electron before a collision and the unprimed after a collision:

$$\begin{aligned} \left( \frac{\partial f(E, \mu, s, t)}{\partial t} \right)_{\text{coll.}} &= - \sum_k n_k(s) \sigma_{\text{tot}}^k(E) \sqrt{\frac{2E}{m}} f(E, \mu, s, t) + \\ &\sum_k n_k(s) \frac{1}{2} \int_{-1}^1 d\mu' \int_0^{\infty} dE' \sigma^k(E' \rightarrow E, \mu' \rightarrow \mu) \sqrt{\frac{2E}{m}} f(E', \mu', s, t). \end{aligned} \quad (2.14)$$

In both terms,  $n_k(s)$  is the atmospheric density,  $\sigma^k(E' \rightarrow E, \mu' \rightarrow \mu)$  is the source terms, single-particle cross section for an electron collision with species  $k$ , and  $\sigma_{\text{tot}}^k(E)$  is the loss-term's total collision cross section integrated over  $\mu$ . There are several source-term cross sections that depend on the type of collisions: scattering, excitation, ionization, and secondary electron production.

For elastic scattering, it is assumed that the momentum transferred to the atom or molecule from the electron collision is very small. The elastic cross section can be written as

$$\sigma_{\text{el}}^k(E' \rightarrow E, \mu' \rightarrow \mu) = p_{\text{el}}^k(\mu, \mu') \sigma_{\text{el}}^k(E') \delta(E - E'), \quad (2.15)$$

where  $p_{\text{el}}^k(\mu, \mu')$  is the normalized angular cross section and often called the phase function,  $\sigma_{\text{el}}^k(E')$  is the elastic cross section, and  $\delta(E' - E)$  is the Dirac delta function. The  $\delta(E' - E)$  term represents the assumption of no energy transfer to the atom or molecule from which the electron scatters. In an excitation collision, an electron of energy  $E'$  that collides with an atmospheric species,  $k$ , will lose the amount of energy,  $W_j^k$ , needed to excite the species to the state,  $j$ . The electron will come away from the collision with energy  $E = E' - W_j^k$ . This cross section can then be written as

$$\sigma_{\text{ex}}^k(E' \rightarrow E, \mu' \rightarrow \mu) = \sum_j p_{\text{ex}}^{kj}(\mu, \mu') \sigma_{\text{ex}}^{kj}(E') \delta(E' - (E + W_j^k)), \quad (2.16)$$

where  $p_{\text{ex}}^{kj}(\mu, \mu')$  is the phase function for an excited state  $j$  of species  $k$  and  $\sigma_{\text{ex}}^{kj}(E')$  is the excitation cross section.

When an electron of energy  $E'$  collides with and ionizes an atmospheric species,  $k$ , two electrons emerge from the collision. The probability that the lower energy electron will be at a particular energy is given by the redistribution function  $R_{\text{sec}}(E', E)$ . This function has been measured in the lab [Opal *et al.*, 1971]. I identify electrons with energies from 0 to  $\frac{E'-W}{2}$  as the secondary electrons and those with energies from  $\frac{E'-W}{2}$  to  $E' - W$ ; the degraded primaries, where  $W$  is the ionization energy [Banks *et al.*, 1974; Strickland *et al.*, 1976]. The redistribution function for the secondaries must mirror the degraded primary redistribution function. Thus, the degraded primary redistribution function is represented by  $R_{\text{deg}}(E', E)$ . The collision cross section for ionization and secondary production then becomes

$$\sigma_{\text{ion}}^k(E' \rightarrow E, \mu' \rightarrow \mu) = \sigma_{\text{ion}}^k(E') \left( p_{\text{deg}}^k(\mu, \mu') R_{\text{deg}}(E', E) + p_{\text{sec}}^k(\mu, \mu') R_{\text{sec}}(E', E) \right) \quad (2.17)$$

where  $p_{\text{deg}}^k(\mu, \mu')$  and  $p_{\text{sec}}^k(\mu, \mu')$  are the phase functions for the degraded primary and the secondary electrons, respectively, and  $\sigma_{\text{ion}}^k(E')$  is the ionization cross section.

It can be important to model the way in which the auroral electrons and subsequent secondaries lose energy to the ambient electron population in the ionosphere. This energy loss is due to elastic Coulomb collisions and Cerenkov wave generation [Itikawa and Aono, 1966]. Stamnes and Rees [1983] use

$$m \frac{\partial \vec{v}}{\partial t} = -n_e(s) L_{ee}(E) \frac{\vec{v}}{v} \quad (2.18)$$

to represent this loss as a frictional (derivative) loss term, which gives an energy derivative term

$$\left( \frac{\delta f}{\delta t} \right)_{\text{ee, coll.}} = \frac{\partial(L_{ee}(E, s) \sqrt{\frac{2E}{m}} f)}{\partial E},$$

where

$$L_{ee}(E, s) = n_e(s) L_{ee}(E)$$

In this thesis, use is made of the loss function,  $L_{ee}(E)$ , that was parameterized by Swartz *et al.* [1971] from the results of Itikawa and Aono [1966]:

$$L_{ee}(E) = \frac{3.37e10^{-12}}{E^{0.94} n_e^{0.03}} \left( \frac{E - T_e}{E - 0.53T_e} \right)^{2.36} \quad (2.19)$$

The ambient electron temperature in eV is  $T_e$ ,  $n_e$  is the electron density in  $\text{cm}^{-3}$ , and  $E$  is the energy of the incident electrons, also in eV. The loss function has units of  $\text{cm}^2 \text{eV}$ .

Inserting the cross sections of Equations 2.15, 2.16, 2.17, and 2.19 into the collision term in the transport equation (Equation 2.13), the time-dependent auroral electron transport equation in terms of  $E$ ,  $\mu$ ,  $s$ , and  $f$  becomes

$$\begin{aligned}
\frac{\partial f}{\partial t} &+ \mu \sqrt{\frac{2E}{m}} \frac{\partial f}{\partial s} + \mu \sqrt{\frac{2E}{m}} F_{\parallel} \frac{\partial f}{\partial E} + \frac{1}{\sqrt{2Em}} ((1 - \mu^2)F_{\parallel} + F_{\text{mirror}}) \frac{\partial f}{\partial \mu} \\
&= \frac{\partial(L_{ee}(E, s) \sqrt{\frac{2E}{m}} f)}{\partial E} - \sum_k n_k(s) \sigma_{\text{tot}}^k(E) \sqrt{\frac{2E}{m}} f(E, \mu, s, t) \\
&+ \sum_k n_k(s) \sigma_{\text{el}}^k(E) \frac{1}{2} \int_{-1}^1 d\mu' p_{\text{el}}^k(\mu, \mu') \sqrt{\frac{2E}{m}} f(E, \mu', s, t) \\
&+ \sum_k n_k(s) \sum_j \sigma_{\text{ex}}^{kj}(E + W_j^k) \frac{1}{2} \int_{-1}^1 d\mu' p_{\text{ex}}^{kj}(\mu, \mu') \sqrt{\frac{2E}{m}} f(E + W_j^k, \mu', s, t) \\
&+ \sum_k n_k(s) \int_{E+W}^{2E+W} dE' \sigma_{\text{ion}}^k(E') R_{\text{deg}}(E', E) \int_{-1}^1 d\mu' p_{\text{deg}}^k(\mu, \mu') \sqrt{\frac{2E}{m}} f(E', \mu', s, t) \\
&+ \sum_k n_k(s) \int_{2E+W}^{\infty} dE' \sigma_{\text{ion}}^k(E') R_{\text{sec}}(E', E) \int_{-1}^1 d\mu' p_{\text{sec}}^k(\mu, \mu') \sqrt{\frac{2E}{m}} f(E', \mu', s, t).
\end{aligned} \tag{2.20}$$

It is possible to rewrite this equation in terms of  $E, \mu, s$ , and  $I$ , the electron intensity using the results of Appendix A, Equation A.10. That is,

$$\begin{aligned}
\sqrt{\frac{m}{2E}} \frac{\partial I}{\partial t} &+ \mu \frac{\partial I}{\partial s} + \mu F_{\parallel} \left( \frac{I}{2E} + \frac{\partial I}{\partial E} \right) + \frac{1}{2E} ((1 - \mu^2)F_{\parallel} + F_{\text{mirror}}) \frac{\partial I}{\partial \mu} \\
&= \frac{\partial(L_{ee}(E, s)I)}{\partial E} - \sum_k n_k(s) \sigma_{\text{tot}}^k(E) I(E, \mu, s, t) \\
&+ \sum_k n_k(s) \int dE' \sigma^k(E', E) \int d\mu' p^k(\mu, \mu') I(E', \mu', s, t),
\end{aligned} \tag{2.21}$$

where the collision term is not fully expanded.

A modified version of Equation 2.21 is solved in Chapter 3, and the results examined for various time varying upper boundary conditions. Other investigators have solved the auroral electron transport equation under specific assumptions. Before discussing the solution to the time-dependent transport equation, it is helpful to understand numerous difficulties that arise when confronting such an equation.

## 2.2 Difficult Aspects of the Transport Equation

To solve the auroral electron integral-differential transport equation, numerical methods have been combined with analytic methods, as the equation cannot be solved using only analytic methods with realistic cross sections and incident electron spectra. Even with numerical methods, the large energy range spanned by the primary and secondary electrons (from .1 eV to over 20 keV) makes the discrete energy degradation of the precipitating auroral electrons difficult to calculate accurately to ensure conservation of energy [Stamnes, 1978], e.g., for an ionization collision, this means that it is difficult to ensure that  $E_p = E'_p - E_s - E_w$ , where  $E_p$  is the energy of the degraded primary,  $E'_p$  is the energy of the primary electron,  $E_s$  is the energy of the secondary electron and  $E_w$  is the ionization potential energy of the atom or molecule which is ionized. Realistic phase functions either need to be fitted analytically or the number of numerical pitch angles needs to be sufficiently large to conserve electron flux [Swartz, 1971]. Because both the inelastic cross sections and the atmospheric density increase by orders of magnitudes, the aurora can span hundreds of kilometers in altitude. To obtain an accurate solution in altitude often means using 100-to-200 grid points over the altitude range from 90 to 500 km. If the converging magnetic field is included, one must decide the method by which the term  $\frac{F_{mirror}}{\sqrt{2E_m}} \frac{\partial f}{\partial \mu}$  is included in the scattering computation. If a parallel electric field is included and if this electric field increases the energy of the electrons, this continuous gain in the electron's energy must be calculated along with the discrete loss in its energy from inelastic collisions. And finally, if the time dependence is included, it is necessary to accurately calculate the distribution function at each time step. It is important to keep the solution computationally efficient as well as accurate. Juggling these two aspects of the time-dependent auroral transport equation is difficult.

Most solutions to the transport equation involve evaluating the evolution of the distribution function by separating the equation into two tasks: 1) calculating the angular redistribution and transport through the atmosphere; and 2) calculating the energy degradation. Energy degradation of the auroral electrons is due to inelastic collisions, which lead to energy losses from fractions of an eV for certain excitation collisions to tens of eV in ionizing collisions. The difficulty with calculating the energy degradation is in resolving all

the discrete energy losses, which is important in order to ensure energy conservation.

Four techniques have been developed for the calculation of energy in photoelectron and auroral electron degradation. One technique involves expanding the distribution function in a Taylor series to first order in energy, which then changes the integral into a derivative [Strickland *et al.*, 1976]. This technique is known as the continuous-slowing-down approximation (CSDA). The CSDA is used in the Fokker-Planck equation since it works well under the assumption that the electrons have energies much larger than the energies that are lost during inelastic collisions. The assumption works well for auroral electrons with energies greater than 3 keV [Strickland *et al.*, 1976]. For electrons with initially low energies, as with photoelectron transport, it is possible to make the numerical energy grid small enough so that the discrete energy losses can be accurately calculated. This method is computationally too expensive for energies much higher than 1 keV [Link, 1992].

In order to deal with auroral electron energy degradation from thermal electrons ( $\sim 0.02$  eV) to high-energy electrons ( $>60$  keV), new techniques have been developed. Swartz [1985] developed an energy degradation scheme that requires changing the cross sections according to the energy grid used. The idea is that a single inelastic collision will not degrade an electron in energy enough to reach the next lower energy grid point for large values of  $dE$ . Thus the probability of losing enough energy to reach the next energy grid point is calculated and this value is used instead of the original inelastic cross section. In this manner, energy is conserved for any energy grid [Stamnes, 1978]. A similar approach is used by Porter *et al.* [1987]. Instead of changing the cross sections, they redistribute the distribution function between the original energy and the new energy. The fraction of the distribution function that is redistributed depends on the inelastic cross section, the discrete energy lost in the collision, conservation of energy, and the energy grid.

Strickland *et al.* [1976, 1989] use yet a different energy degradation technique in which the elastic scattering is also considered. First, a two dimensional polynomial in  $E$  and  $\mu$  is constructed with undefined coefficients to create a predicted electron distribution function. The distribution function at the  $E$ - $\mu$  boundary is fitted with the polynomial and extrapolated to the next  $E$  and  $\mu$  grid point. Using the extrapolated values of the distribution function allows its evaluation at the discrete energy losses.

The way in which the pitch-angle scattering is calculated also varies quite a bit in

methodology. The difficulties involved with this calculation stem from the strongly forward-peaked phase function for high-energy electrons and from the distribution function itself when strongly peaked. Obtaining an accurate numerical integration scheme for such functions requires special techniques. The first approaches to scattering assumed that all scattering is forward peaked [e.g., *Walt et al.*, 1969; *Strickland and Bernstein*, 1976]. With this assumption, one can expand the electron distribution function in a Taylor series to second order in  $\mu$  and obtain a derivative scattering term from the integral scattering term [*Strickland et al.*, 1976]. This gives the scattering term for the Fokker-Planck equation. However, forward scattering is not a good assumption for low-energy electrons that scatter more isotropically.

Another technique to evaluate the effect of scattering is the two-stream approach, where the transport equation is integrated over the upward and the downward hemispheres, i.e. integrated over azimuthal angles and the positive  $\mu$  space and negative  $\mu$  space [*Banks et al.*, 1974]. This gives two coupled, first-order differential equations for electrons moving either upward or downward. The two equations are coupled by a backscatter coefficient which gives the probability of an electron changing direction from one hemisphere to the other in  $\mu$  space. Multi-stream calculations [e.g., *Stamnes*, 1980; *Lummerzheim and Liliensten*, 1994] are similar in concept, but instead of two coupled, first-order differential equations, there are multiple coupled equations, each equation describing electrons moving at some average  $\mu$ . In order to obtain coupling between the streams, the scattering integral must be approximated by an algebraic summation. *Stamnes* [1980] calculates the scattering integral using a technique common in radiative transfer work, by changing the integral into an algebraic sum by the Gaussian quadrature method. However, accurately evaluating the scattering integral, which contains strongly forward-peaked phase functions, can be difficult with this method if one wants to keep the number of streams (i.e., number of  $\mu$  grid points) low for computational efficiency. *Wiscombe* [1977] developed a method to represent forward-peaked phase functions by a delta function added to an expansion of the Legendre polynomials. This has been shown to be an accurate and efficient way to solve the scattering problem for the phase functions used in auroral transport calculations.

The way in which the electron transport is solved depends partially on the way in which the collisions are calculated, as in the above mentioned energy loss and scattering



collisions. The most straight forward, but computationally expensive, way to solve the transport equation is by using the Monte Carlo technique [e.g., *Solomon*, 1993; *Onda et al.*, 1999], in which one selects individual particles from a distribution of particles in phase space and then individually solves the equation of transport for these particles. This type of simulation is conducive to using the splitting technique [*Ohwada*, 1998]. In one time step the collisionless transport of the particles is calculated for a mean-free-path length or in a time given by the average time between collisions. In the next time step the effect of collisions on the particles is determined, giving a new distribution function which is then transported without collisions in the next step, and so on. The splitting technique can also be used to solve the transport equation using numerical differencing techniques [*Ohwada*, 1998].

It is often more computationally efficient to solve the altitude transport using other techniques, since the Monte Carlo method requires an extremely large number of particles to describe the secondary contribution to the distribution function. In the case of the two-stream approach used by *Banks et al.* [1974], the two coupled, first-order differential equations are combined into a single second-order differential equation for one stream which is solved. This second-order equation has been solved, but it is difficult due to the complicated terms which arise when combining the two first-order equations [*Link*, 1992]. The Feautrier method [*Feautrier*, 1964], often used in astrophysical transport problems with high collision frequencies in dense stellar atmospheres, solves the two-stream as well as the multi-stream problem by changing the distribution function into a symmetric part and an asymmetric part and then using a Taylor series to approximate the derivatives of the two first-order equations to obtain a system of algebraic equations. *Link* [1992] uses this approach for photoelectrons, but no one has been able to extend the technique to the higher energies needed to solve the auroral electron transport equation. The altitude transport in the multi-stream techniques used by *Lummerzheim and Liliensten* [1994] and *Stamnes* [1980] is incorporated in the discrete ordinate method mentioned above. Once the scattering integral is converted to a Gaussian quadrature summation, it is possible to solve the system of algebraic equations by expanding the distribution function in exponential functions. This leaves an eigenvalue problem involving inversion of a matrix. Inverting the resulting large matrix is difficult numerically because the matrix consists of large numbers for which dif-

ferences are taken in the inversion of the matrix. *Stamnes and Conklin* [1984] devised a technique to overcome this difficulty.

Not many solutions to the auroral electron transport equation include a parallel electric field. The solutions that do exist depend on iterative techniques to obtain an accurate solution [*Min et al.*, 1993; *Waite et al.*, 1988; *Liemohn et al.*, 1997]. Iterative techniques are required since the way energy loss collisions are evaluated requires that the electrons lose, not gain, energy. But with the existence of a parallel electric field there will be energy gain. The iterative approach allows the energy loss to be calculated with standard techniques and then the contribution to the flux at higher energies from lower-energy electrons is calculated from the prior iteration until convergence is achieved. However, this process is so computationally expensive that assumptions have to be made. *Waite et al.* [1988] use the two-stream approach and then assume that “the loss of flux in the (upward) direction due to the electric field depends on the value of (the upward flux) and the rate of transfer of flux across the  $\mu = 0$  plane in velocity space.” This can lead to losses in accuracy of up to 50%. *Min et al.* [1993] used the multi-stream approach assuming that the electric field is  $\leq 50 \mu\text{V/m}$ . (It is important to note at this point that caution needs to be exercised when using the results of *Min et al.* [1993] since kinetic energy and total energy were confused in deriving the final equation that they solved.) *Liemohn et al.* [1997] include the electric field for the transport of suprathermal electrons in the plasma sheet while also including the ionospheres at each end of a field line. The form of the transport equation they use is a Fokker-Planck type of equation. They also use an iterative technique to include the effects of the electric field.

*Khazanov and Liemohn* [1995] include time dependence in their studies of the suprathermal ionosphere-plasma-sheet electron transport. However, no one has studied the time-dependent auroral electron transport equation. *Onda et al.* [1999] have solved the transport equation for auroral electrons using the Monte Carlo technique with time-dependent motion of the particles between collisions given by

$$m \frac{d\vec{v}}{dt} = q\vec{v} \times \vec{B},$$

where  $m$  is the mass of the electron,  $\vec{v}$  is the velocity of the electron,  $q$  is the charge of an electron, and  $\vec{B}$  is the magnetic field. No time dependence of the electron equation is

discussed in their paper. In Chapter 3, I use simplifications and further assumptions to solve the time-dependent transport equation. Solutions of the electron intensity in phase space as a function of time will then be used to discuss the time dependence of auroral electrons for a pulse of electrons entering the upper atmosphere.

## Chapter 3

# Solution to the Time-Dependent Transport Equation

A time-dependent auroral electron transport equation was derived in Chapter 2. As it stands, it is not currently possible to solve this equation. However, some restrictive assumptions lead to simplifications that allow solutions to a time-dependent transport equation. In this thesis, the mirror force and parallel electric fields are assumed to be negligible. It is possible to use different assumptions in the calculation of the transport of high-energy electrons *versus* the transport of low-energy electrons owing to the energy dependence of the collision cross sections. Thus the auroral electron transport equation can be separated into two equations: one for the primary and degraded primary electrons and one for the secondary and degraded secondary electrons. A continuous-slowing-down approximation (CSDA) is assumed for the primary electrons and no vertical transport is assumed in the secondary electron equation. The scattering term is not included in either equation.

After a discussion about these assumptions, the equations are presented in their final form and then the method of solution is discussed. The accuracy of the solution and the consequences of the assumptions made are examined by comparing the time-dependent solution at steady state with the steady-state calculations of *Lummerzheim and Lilénsten* [1994]. Once the uncertainties in the time-dependent solution are established, the time evolution of five different electron spectra incident on the upper atmosphere is studied. The time required for the electrons to reach steady state in phase space as the electrons enter

the ionosphere, degrade in energy and produce secondaries is quantified for the five spectra. The electrons are turned off at the upper boundary and the time for the electrons to lose their energy and become part of the thermal electron population is also studied for each of the five spectra.

## 3.1 The Equation Revisited

### 3.1.1 Further Assumptions

In order to simplify the transport equation, it is reasonable to assume that the magnetic field does not affect the transport of auroral electrons that are modeled from 600 down to 90 km in altitude [Min *et al.*, 1993]. The electrons that do mirror in this region do not collide with the atmosphere and if needed, can be modelled without the Boltzmann collision term. Mirroring electrons will not affect optical emissions or ionization rates by definition since they have not interacted with the upper atmosphere. The electrons that do collide with the upper atmosphere and are affected by the small change in the magnetic field gradient in this region only contribute to a small percent of the total electron intensity [Min *et al.*, 1993]. With this assumption, the effect of magnetic mirror force,  $F_{\text{mirror}}$ , on the electron transport is very small and thus the mirror force term in Equation 2.21 can be neglected.

Parallel electric fields, such as those associated with currents driven by magnetospheric convection into the ionosphere and associated with electron precipitation, will not influence the electron distribution function low in the ionosphere [Min *et al.*, 1993; Waite *et al.*, 1988]. Waite *et al.* [1988] states that it is “unlikely that parallel electric fields produced by dynamo processes make any significant contribution to the dayglow emissions (on Uranus)”. Min *et al.* [1993] show that including the effect of electric fields on Earth only affects the distribution functions above 250 km in altitude and mostly the low-energy (< 50 eV) electrons. Since the electron distribution in this region will not greatly affect the ionization and emission rates studied in this thesis, the electric field will not be included in the transport equation. Both the energy derivative and pitch-angle derivative associated with a parallel electric field in Equation 2.21 have been neglected.

Since the collision-dominated physics for high-energy and low-energy electrons is different, especially for altitudes >90 and <200 km, it is reasonable to separate the transport

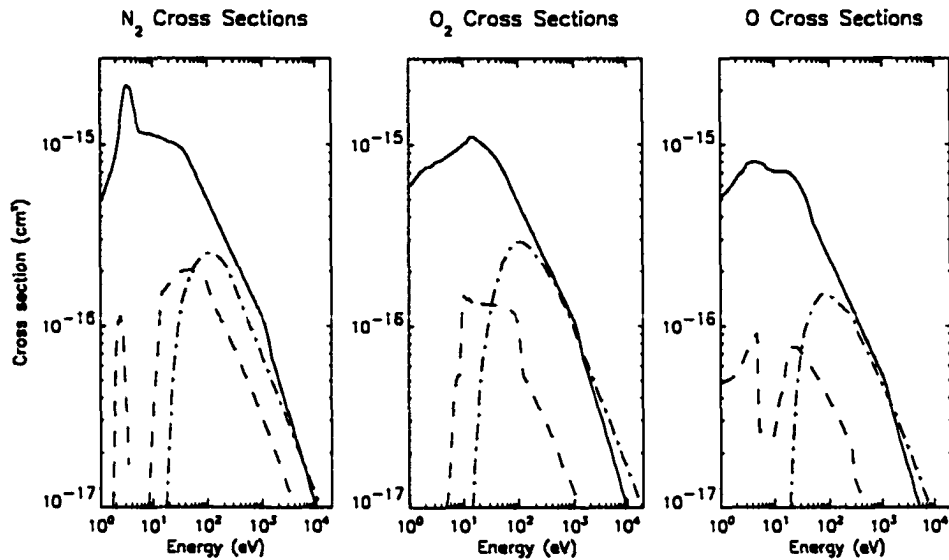


Figure 3.1. Total cross sections. The elastic (solid line), excitation (dashed line) and ionization (dotted-dashed line) cross sections are shown as a function of energy for  $N_2$ ,  $O_2$ , and  $O$ . These cross sections are from a set compiled by *Lummerzheim and Liliensten [1994]* and used throughout this thesis.

equation into two equations, one for each population [*Vallance Jones et al., 1991*]. Figure 3.1 shows ionization, excitation, and elastic cross sections for electrons colliding with  $N_2$ ,  $O_2$ , and  $O$ . This figure demonstrates that the probability of an electron colliding with a neutral molecule or atom is much lower for electrons with energies  $>1$  keV than for those with energies  $<1$  keV. It is also evident from this figure that elastic collisions will be much more probable than inelastic collisions for electrons with energies less than  $\sim 100$  eV. The precipitating (primary and degraded primary) and secondary electrons can be separated into two equations that can be solved using different assumptions for each population (equation), which is the main advantage of solving the time-dependent equation using two equations.

The precipitating electrons are typically of energies great enough ( $>3$  keV) that the continuous-slowing-down approximation (CSDA) is valid, as mentioned in Chapter 2. This assumption allows the energy degradation integral in Equation 2.21 to be replaced by an energy derivative representing a frictional loss, as is done with the energy loss to the thermal electrons from the suprathermal electrons in Equation 2.19. Since the elastic phase function for high-energy electrons is strongly forward peaked [*Stamnes, 1978*] and the elastic

cross sections are less than the inelastic cross sections for electrons with energies  $>10$  keV, as shown in Figure 3.1, scattering is negligible for electrons with energies  $>10$  keV. For electrons with energies  $<10$  keV but  $>200$  eV, the elastic and inelastic cross sections are of similar magnitude within a factor of two. In this region, the elastic phase function is still strongly forward peaked, and so the electrons that elastically scatter will change their pitch angle only slightly. For electron beams that are field-aligned, as studied in this thesis, this small change in pitch angle means very few electrons will be backscattered. However, the change in pitch angle will increase the time an electron remains in a region of the atmosphere. Thus, there is an increase of the probability of an inelastic collision, which increases the probability of any type of collision and so on. It is thus assumed that the scattering integral is negligible for electrons with energies  $>200$  eV except for the effect of increasing the energy loss at each altitude. The error associated with this assumption will be discussed in Section 3.2.3.

It is also assumed that the elastic cross section is sufficiently large at low energies ( $<200$  eV) so that secondary electrons with such energies will not travel in altitude. The assumption that the altitude transport term is negligible has been justified below 150 km by comparing rocket spectra and optical observations with a steady-state transport calculation using this assumption [Vallance Jones *et al.*, 1991]. The phase function for elastic scattering of low-energy electrons is practically isotropic [Lummerzheim and Lilensten, 1994] and since the electrons are assumed to not transport in altitude, the elastic scattering integral is neglected.

Neglecting elastic scattering avoids computing the electron intensity as a function of  $\mu$ . Instead, the spherical intensity,

$$\bar{I}(E, s, t) = 2\pi \int_1^{-1} I(E, s, \mu, t) d\mu, \quad (3.1)$$

is modeled. With this quantity, it is possible to calculate altitude dependent ionization and

$$\begin{aligned} \text{excitation rates, } \eta_j^k(s) &= 2\pi \sum_k n_k(s) \int_{-\infty}^{\infty} dE \sigma_j^k(E) \int_1^{-1} d\mu I(E, s, \mu, t) \\ &= \sum_k n_k(s) \int_{-\infty}^{\infty} dE \sigma_j^k(E) \bar{I}(E, s, t) \\ &= \sum_k n_k(s) \int_{-\infty}^{\infty} dE \sigma_j^k(E) \bar{I}(E, s, t) \end{aligned} \quad (3.2)$$

for species,  $k$  and state,  $j$ , which include the possibility of ionization. The other variables were previously defined. Detailed calculations of excitation and ionization rates for different time-dependent solutions will be discussed in Chapter 3.2. In Section 3.2.3 of this chapter, steady-state ionization rates, as well as the spherical intensity,  $\bar{I}$ , will be used to compare the time-dependent solution once it has reached a steady state with a well-tested, steady-state transport calculation. For the rest of the thesis, intensity will be used to mean spherical intensity.

### 3.1.2 Final Equations

As mentioned above, the CSDA used for the precipitating electrons implies that the energy degradation integral for the inelastic processes can be written as a derivative. *Strickland et al.* [1976] use such a term in the Fokker-Planck equation for auroral electrons. This term is written as

$$\frac{\partial(L_{en}(E, s)I)}{\partial E}, \quad (3.3)$$

where the loss function is

$$L_{en}(E, s) = \sum_k n_k(s) \sum_j \sigma_k^j(E) \Delta E_k^j. \quad (3.4)$$

The terms have the same meanings as in Chapter 2, with  $\Delta E_k^j$  the amount of energy lost in an inelastic collision of the type represented by the cross section  $\sigma_k^j(E)$ . Using this frictional loss term and the assumptions stated above, the equation for precipitating electrons solved in this thesis is

$$\frac{\partial I_1(E, s, \mu_d, t)}{\partial t} = \mu \sqrt{\frac{2E}{m}} \frac{\partial I_1(E, s, \mu_d, t)}{\partial s} + \sqrt{\frac{2E}{m}} \frac{\partial(L_{en}I_1(E, s, \mu_d, t))}{\partial E}, \quad (3.5)$$

where  $\mu_d$  represents the downward cosine of the pitch angles and  $I_1(E, s, \mu_d, t)$  is the precipitating electron intensity. The function  $I_1$  is retained in this equation instead of the spherical intensity,  $\bar{I}_1(E, s, t)$ , so that differences between isotropic downward distribution functions and field-aligned functions can be studied.

Using the assumptions above for the secondary electrons, the transport equation for these electrons becomes a time-dependent equation of energy degradation and secondary



electron production. The solution to this equation is the secondary electron spherical intensity,  $\bar{I}_2(E, s, t)$ , which is calculated by converting the precipitating electron distribution function,  $I_1$  to  $\bar{I}_1(E, s, t)$  and using it as a source term in the secondary electron equation:

$$\frac{\partial \bar{I}_2(E, s, t)}{\partial t} = \sqrt{\frac{2E}{m}} \frac{\partial (L_{ee} \bar{I}_2(E, s, t))}{\partial E} - C(s, E) \bar{I}_2(E, s, t) + Q_{\text{deg}} + Q_{\text{sec}} + Q_{\text{source}}, \quad (3.6)$$

where

$$\begin{aligned} C(s, E) &= \sqrt{\frac{2E}{m}} \sum_k n_k(s) \sigma_{\text{inel}}^k(E) \\ Q_{\text{deg}} &= \sqrt{\frac{2E}{m}} \sum_k n_k(s) \sum_j \sigma_{\text{ex}}^{kj}(E + W_j^k) \bar{I}_2(E + W_j^k, s, t) \\ &\quad + \sqrt{\frac{2E}{m}} \sum_k n_k(s) \int_{E+W}^{2E+W} dE' \sigma_{\text{ion}}^k(E') R_{\text{deg}}(E', E) \bar{I}_2(E', s, t) \\ Q_{\text{sec}} &= \sqrt{\frac{2E}{m}} \sum_k n_k(s) \int_{2E+W}^{\infty} dE' \sigma_{\text{ion}}^k(E') R_{\text{sec}}(E', E) \bar{I}_2(E', s, t) \\ Q_{\text{source}} &= \sqrt{\frac{2E}{m}} \sum_k n_k(s) \frac{1}{2} \int_{2E+W}^{\infty} dE' \sigma_{\text{ion}}^k(E') R_{\text{sec}}(E', E) \bar{I}_1(E', s, t). \end{aligned}$$

Although the secondary distribution is still written as a function of altitude, the dependence on this variable is completely due to the precipitating electron source term, not to any other terms in the equation.

## 3.2 Method of Solution

### 3.2.1 Evaluating Important Functions

In order to solve Equations 3.5 and 3.6, it is necessary to be able to accurately represent the following functions:  $n_e(s)$ ,  $L_{ee}(E, s)$ ,  $\sigma_{\text{ex}}^{kj}(E + W_j^k)$ ,  $\sigma_{\text{ion}}^k(E')$ ,  $R_{\text{deg}}(E', E)$ , and  $R_{\text{sec}}(E', E)$ . Errors in these functions will produce errors in the final solution. The subject of this section is how each of these functions is obtained and the potential errors associated with each function.

The electron-electron collisional loss function,  $L_{ee}(E, s)$ , in the term 2.19, is most important when using the transport equation to calculate heating rates of thermal electrons. This is because term 2.19 determines the energy loss from the secondary auroral electrons to the

thermal electrons.  $L_{ee}(E, s)$  and the electron thermal temperature are non-linearly related. However,  $L_{ee}(E, s) \ll L_{en}(E, s)$  above 1 eV for typical electron temperatures of 1,000 K and typical nighttime neutral densities, such as those shown in Figure 1.3. This implies that  $L_{ee}(E, s)$  does not significantly affect the excitation and ionization rates studied in Chapters 4 and 5, which have cross section maxima at energies above 6 eV except in cases of very high thermal electron temperatures. The function  $L_{ee}(E, s)$  used here was defined in Equations 2.19 and 2.19. The electron density,  $n_e(s)$ , in  $L_{ee}(E, s)$  can be determined by at least three methods: experimentally through incoherent scatter radar measurements; from a statistical model ionosphere which uses radar and other data to generate electron densities, e.g., the International Reference Ionosphere 93 (IRI93) [Bilitza et al., 1993]; or by solving the coupled continuity equations for ion species [e.g., Palmer, 1995]. The IRI93 is used here.

The neutral density for species  $k$ ,  $n_k(s)$ , is a very important input parameter for changes in  $n_k(s)$  lead to changes in the collision source and loss terms, and these in turn affect the altitude at which the electrons deposit the bulk of their energy. Several methods for determining  $n_k(s)$  exist: *in-situ* measurements, such as with a mass spectrometer on a rocket; empirical upper atmospheric models, such as the Mass Spectrometer Incoherent Scatter 90 (MSIS-90) model; or first-principle models such as the Thermosphere-Ionosphere Electromagnetic Global Circulation Model (TIE-GCM) [Roble and Ridley, 1987; Richmond et al., 1992]. Determining  $n_k(s)$  for a particular aurora is difficult since *in-situ* measurements of the upper atmosphere with aurora are rare. Also, it has been shown that models do not accurately represent the altitude profile of the different atmospheric species, such as atomic oxygen, during auroral precipitation since Joule heating associated with currents in the aurora can change atmospheric height profiles [Hays et al., 1973]. Errors in the neutral density will affect the solution to the transport equation mostly below 250 km where the density is large enough to affect the electron transport significantly. The MSIS-90 model is used here.

The choice of cross sections,  $\sigma_{ei}^k(E)$ ,  $\sigma_{ex}^{kj}(E)$ , and  $\sigma_{ion}^k(E')$  is difficult. Lummerzheim and Liliensten [1994] compare their steady-state transport calculation using different cross section sets and find that there can be up to a 20% difference in the solution of the electron intensity. The transport calculation is sensitive to any changes in a cross section at any

energy, but especially where the cross sections are largest and thus have the largest influence on the solution. As seen in Figure 3.1, the inelastic cross sections peak between  $\sim 10$  eV and  $\sim 300$  eV, except for the vibrational levels of  $N_2$ , which peak around 2 eV. Several different compiled cross section sets were used in an ionospheric model to compare radar data with the model [Schlesier *et al.*, 1997]. Schlesier *et al.* [1997] found that the model using the cross section set used by Lummerzheim and Lilensten [1994] produced the best agreements between the model and the ionospheric radar data. In this thesis, the cross section set of Lummerzheim and Lilensten [1994] is used in part to be able to compare with their steady-state results and in part because of the results of Schlesier *et al.* [1997].

The energy redistribution functions involved in the ionizing collisions,  $R_{\text{deg}}(E', E)$  and  $R_{\text{sec}}(E', E)$ , are also very important to the solution to the electron transport equation. These functions determine how the secondaries will be distributed in an ionizing collision and depend on the energy of the incident electron, the primary electron, as well as how much energy this primary electron loses. Energy conservation in an ionizing collision requires that the sum of the energy of the secondary electron,  $E_s$ , the energy of the degraded primary electron,  $E_p$ , and the ionization potential,  $W$ , add up to the energy of the incident electron  $E$ . Therefore, it is possible to write  $E_p = E - W - E_s$ , which requires:

$$R_{\text{deg}}(E - W - E_s, E) = R_{\text{sec}}(E_s, E) \quad (3.7)$$

This function is well represented both by theory [Rees *et al.*, 1969] and by experiment [Opal *et al.*, 1971], which agree to within 20% [Lummerzheim and Lilensten, 1994]. In this thesis the parameterization of Opal *et al.* [1971] is used.

### 3.2.2 Numerical Discretization

The simulation covers altitudes from 90 to 630 km and energies from .1 eV to 22 keV. When the precipitating electrons have pitch angles other than zero, only downward pitch angles are used. All the numerical grids are non-linear, as shown in Figure 3.2. The energy grid contains 216 grid points with the grid spacings growing in energy so that the details in the cross sections below 1 keV are resolved, which is important in calculating the optical observables such as column brightness in the magnetic zenith. The altitude grid contains 137 grid points with the grid spacings increasing in altitude since the atmospheric density

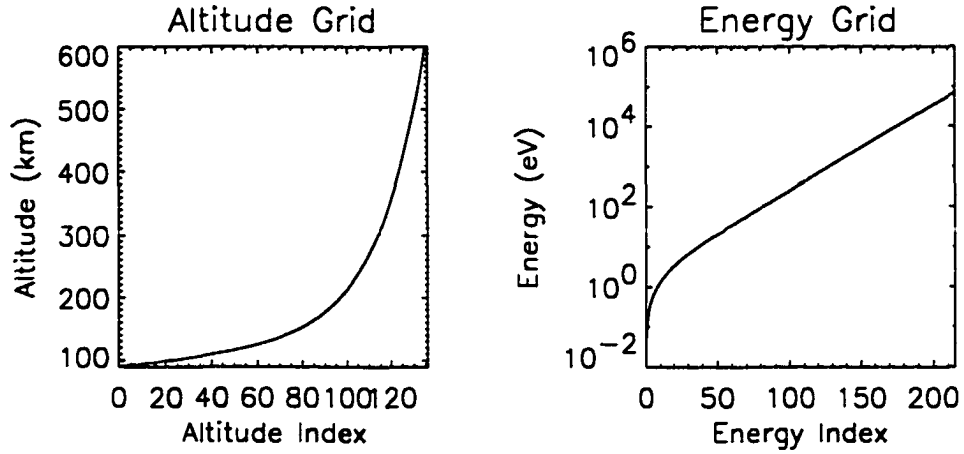


Figure 3.2. Altitude and energy grids used in this thesis.

decreases rapidly in altitude. The  $\mu$  grid for the precipitating electrons is spaced such that the pitch angles are equal and spaced every  $16^\circ$ .

The numerical discretizations for the time and altitude derivatives are taken from computational techniques for fluid dynamics [Fletcher, 1991]. However, using standard explicit schemes for the energy loss terms, i.e. the energy derivative in Equation 3.5 and the energy integral and derivative in Equation 3.6 require incredibly small time steps if typical discretizations are used. The Courant-Friedrichs-Lewy (CFL) condition must be satisfied for explicit numerical discretizations schemes to ensure that the solution remains stable. To examine the stability condition for a true leapfrog discretization, i.e. centered in space, time and energy, it is useful to separate the energy derivative in Equation 3.5 into two terms,

$$\sqrt{\frac{2E}{m}} \frac{\partial(L_{en}I)}{\partial E} = \sqrt{\frac{2E}{m}} L_{en} \frac{\partial I}{\partial E} + \sqrt{\frac{2E}{m}} I \frac{\partial L_{en}}{\partial E}. \quad (3.8)$$

The CFL condition for the  $\frac{\partial I}{\partial E}$  term is

$$\Delta t < \frac{\Delta E}{\sqrt{\frac{2E}{m}} L_{en}}.$$

Plugging in numbers from the simulation grids discussed above, gives a maximum time steps of  $2 \times 10^{-7}$  s. Since it was already estimated in Chapter 1 that the time-dependence

may be important for time scales greater than 100 ms, this would mean using a million time-steps. Such a large number of time steps not only produces long computer runs, but also leads to round-off errors.

A larger time-step can be used with numerical grids using a larger  $\Delta E$ . However, for any significant increase in the time step, the typical  $\Delta E$  around 100 eV (peak inelastic cross section) and at 120 km (where collisions become frequent) would need to be greater than 500 eV. Unfortunately, this is also the region in phase space that is important for observables such as the  $N_2^+$  emissions. Energy resolution simply cannot be sacrificed in this region. In order to surpass these difficulties, I developed a new discretization for this term. This scheme is also used in the secondary electron equation for the electron-electron loss function,  $L_{ee}$  and the discrete loss term  $C(E, s)$ .

The frictional loss term,  $L$ , in the steady-state transport equation is often discretized as

$$\frac{\partial(LI)}{\partial E} = \frac{L_{i+1}I_{i+1}}{\Delta E} - \frac{L_i I_i}{\Delta E} \quad (3.9)$$

[Link, 1992; Lummerzheim and Lilensten, 1994], where  $\Delta E = E_{i+1} - E_i$ . The  $i + 1$  term is considered a source term and the  $i$  term a loss term. Thus, the source term is included with the energy degradation integral,  $Q_{deg}$ , and the loss term is included with the inelastic collisional loss term,  $C(s, E)$ . When including the time dependence in the secondary electron local transport calculation, these terms are kept separate. The electrons are losing energy as time increases and they are losing energy very rapidly at low altitudes due to the high neutral density and cross sections. This indicates that it may be possible to calculate the energy loss at  $t = n+1$  and the source term at  $t = n$ . When using a centered time (leapfrog) discretization for the time-derivative, the new energy derivative discretization would look like

$$\frac{I_i^{n+1} - I_i^{n-1}}{2\Delta t} = \sqrt{\frac{2E}{m}} \left( \frac{L_{i+1}I_{i+1}^n}{\Delta E} - \frac{L_i I_i^{n+1}}{\Delta E} \right), \quad (3.10)$$

and thus makes the energy derivative scheme somewhat implicit. This is the new discretization which is used in this thesis.

In the discretization of Equation 3.5, a leapfrog time derivative is used with a centered-space discretization for the spatial transport term and the newly developed discretization for the energy derivative. After some algebraic manipulation, the discretization of Equation 3.5

is

$$\begin{aligned} I_{ijk}^{n+1} &= \frac{1}{\left(1 + \frac{2\Delta t v_i L_{ij}}{\Delta E_i}\right)} \left( I_{ijk}^{n-1} + \frac{2\Delta t v_i L_{i+1j}}{\Delta E_i} I_{i+1jk}^n \right. \\ &\quad \left. + \frac{\mu v_i 2\Delta t}{(z_{i+1} - z_{i-1})} (I_{ij+1k}^n - I_{ij-1k}^n) \right), \end{aligned} \quad (3.11)$$

with the subscripts  $i, j, k, n$ , representing the indices for the variables  $E, s, \mu$ , and  $t$ , respectively, and  $v_i = \sqrt{\frac{2E_i}{m}}$  the non-relativistic velocity of the particle.

The secondary equation is solved using a version of the *Lummerzheim and Liliensten* [1994] technique, which only includes the energy degradation of electrons in the transport equation. *Lummerzheim and Liliensten* [1994] solve the energy degradation using an algorithm developed by *Swartz et al.* [1971]. The time dependence is included by using a forward-differencing scheme and energy loss discretization as discussed above, written as

$$\bar{I}_{ij}^{n+1} = \frac{1}{1 + \Delta t (C_{ij} + \frac{v_i L_{ij}}{\Delta E_i})} \left( \bar{I}_{ij}^n + \frac{\Delta t v_i L_{i+1j}}{\Delta E_i} \bar{I}_{i+1j}^n + \Delta t (Q_{\text{int}})_{ij}^n + \Delta t (Q_{\text{source}})_{ij}^n \right), \quad (3.12)$$

where

$$Q_{\text{int}} = Q_{\text{deg}} + Q_{\text{sec}}$$

and

$$L = L_{ee}(E, s).$$

Equation 3.11 is solved first and then the intensity from this solution,  $I$ , is integrated in pitch angle (when necessary) and used as the source intensity,  $\bar{I}_1$ , in  $Q_{\text{source}}$  of Equation 3.12.

To check the numerical consistency of Equations 3.11 and 3.12, it is necessary to reverse the discretization process through a Taylor series expansion [*Fletcher*, 1991, chap. 4] to verify that the original equation is returned. Expanding the terms in a Taylor series for Equation 3.5 results in the equation

$$\frac{\partial I}{\partial t} = \frac{1}{\left(1 + \frac{\Delta t}{\Delta E} v L\right)} \left( \mu v \frac{\partial I}{\partial s} + v \frac{\partial(LI)}{\partial E} \right). \quad (3.13)$$

The discretization in Equation 3.11 is consistent with Equation 3.5 as long as  $\frac{\Delta t}{\Delta E} v L \ll 1$ . However, if  $\frac{\Delta t}{\Delta E} v L$  is  $> 1$ , then  $\frac{\partial I}{\partial t} = 0$  which means that this discretization approaches

steady state and thus the new energy discretization will not change the steady state solution. The consistency check for Equation 3.12 similarly demonstrates that  $\Delta t(C + \frac{vL}{\Delta E}) \ll 1$  will ensure that the discretized equation matches the physical equation and that the steady state solution is kept correct. Both Equations 3.11 and 3.12 are first order accurate if the two conditions are satisfied.

The energy degradation/loss process can be thought of in terms of a relaxation process in energy. The new energy discretization scheme will cause the solution to the transport equation to relax to steady state more slowly than it should in regions where  $\frac{\Delta t}{\Delta E}vL$  and  $\Delta t(C + \frac{vL}{\Delta E})$  are greater than 1. If the actual relaxation occurs on time scales much faster than a time step, it is sufficient for the numerical relaxation to occur on the time scale of the time step chosen for the simulation since then the error in the solution is still small.

With the grids discussed above and the maximum time steps used in this thesis ( $1 \times 10^{-5}$  s for Equation 3.11 and up to 4 ms for Equation 3.12), the percent error in the relaxation time can be calculated using  $\frac{\Delta t}{\Delta E}vL$  and  $\Delta t(C + \frac{vL}{\Delta E})$ . This error is plotted in Figure 3.3 as a function of energy and altitude for the relevant energy grids used in Equations 3.11 and 3.12. In most of the computational domain, the error is small. The largest errors occur around 100 eV and below 150 km, where energy is lost on time scales much faster than 1 ms, the minimum time studied in this thesis. Although the percent error is extremely high in this region, the actual error in the solution is still relatively small on time scales greater than 1 ms. For example, if it took 2 ms to lose energy in the region where there is a 1,000% error, the real relaxation time would be 0.5 ms. The >10 ms time scales in the simulation occur higher in the atmosphere or at very low or very high energies where the errors in relaxation times are small.

### 3.2.3 Solution Accuracy

There are no data with which to test the time-dependent transport calculation (measurements of both *in situ* electron differential flux and optical measurements at 1-ms resolution) and there are no other time-dependent transport calculations with which to compare since this is the first time-dependent auroral transport calculation. It is possible, however, to compare the steady-state limit of the time-dependent solution to a steady-state solution. The steady-state transport calculation of *Lummerzheim and Lilensten [1994]* has been tested

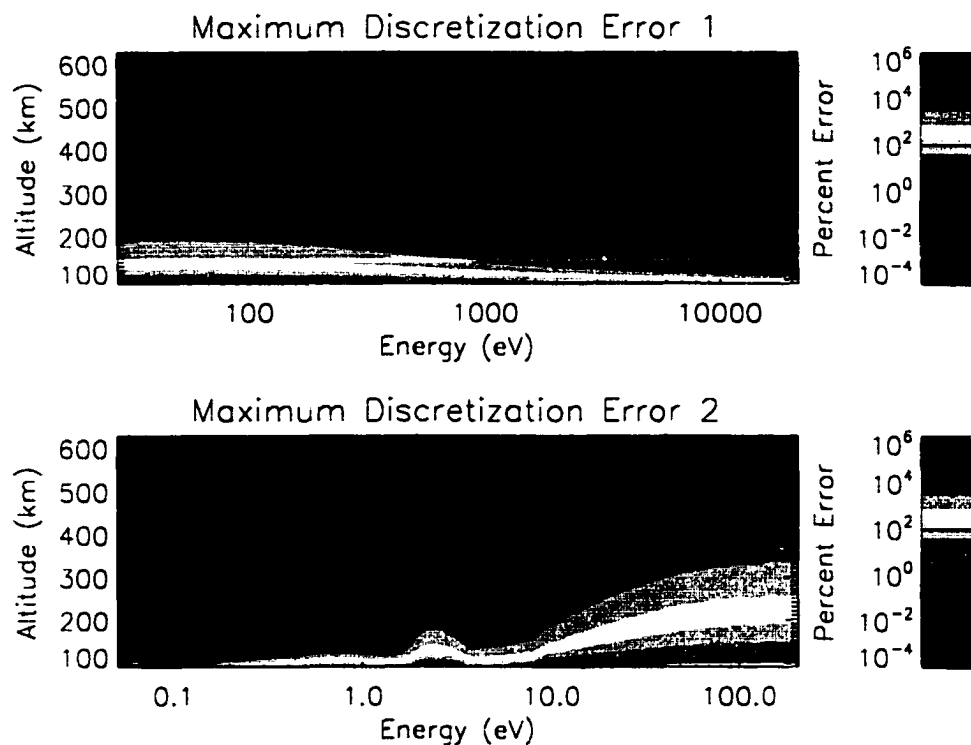


Figure 3.3. Errors from the numerical energy discretization. The maximum error in the relaxation rate of the energy loss process for the precipitating and secondary equations is shown. The top plot represents the error for the precipitating equation with a time step of  $1 \times 10^{-5}$  s and the bottom plot for the secondary equation with a time step of 4 ms.

against other transport calculations [Strickland *et al.*, 1976; Solomon, 1993] and agrees within 20%, the uncertainty in the different cross-section sets. It has also been shown to agree well with the magnitude for electron fluxes observed in rocket data [Lummerzheim *et al.*, 1989]. Since the secondary-electron equation in this thesis is calculated using the energy degradation of Lummerzheim and Lilensten [1994], the comparison between the steady-state limit of the time-dependent calculation and the calculation of Lummerzheim and Lilensten [1994] can provide some confidence in the time-dependent transport calculation.

In order to examine the validity of the assumptions that have been made above, it is important that uncertainties associated with the atmospheric density, the cross sections,



other functions mentioned above, and numerical errors are small. *Lummerzheim and Liliensten* [1994] discuss the sensitivity to variations of the functions discussed above on the electron intensity. They show that the intensity does not vary more than 20% for reasonable uncertainties in these functions. Since the same sources are used, *e.g.*, MSIS-90 and IRI93, for the functions in the steady-state transport calculations and the time-dependent calculations, any differences in the solutions will not be due to differences in these functions.

Before comparisons are made with steady-state calculations of *Lummerzheim and Liliensten* [1994], the time-dependent discretization in the secondary electron calculation is tested by solving Equation 3.12 without the time dependence and then running the model with the time dependence and comparing the results. The source used for this comparison is a 2-keV Gaussian, field-aligned ( $\mu = 1$ ) electron intensity with a downward flux of  $1 \text{ mW m}^{-2}$ . The monoenergetic, precipitating electron beam is modeled using a Gaussian distribution in energy with the half-width 10% of the peak energy (2 keV). All monoenergetic beams in this thesis are modeled with Gaussians which have half-widths 10% of their peak energies. The source is kept on for one second in the time-dependent calculation. The spherical intensity,  $\bar{I}$ , for both cases is shown in Figure 3.4. The precipitating electrons are represented by the electron intensity seen as a beam at 2 keV and the secondaries by the intensity at energies below  $\sim 1$  keV, except at altitudes  $< 175$  km where the intensity represents the degraded primaries for energies  $> 100$  eV. The intensities in the two panels of Figure 3.4 are identical below  $\sim 300$  km. Although this study indicates nothing about the solution in the time it took to reach steady state, it gives some confidence in the newly developed loss function numerical scheme.

The assumption made in the time-dependent transport model that is the most difficult to justify is that the scattering integral is negligible except for the effect of increasing the energy loss at each altitude. Since this is the first time-dependent transport calculation, the shape of the spherical electron intensity due to scattering is emphasized in order that the deficiencies of the time-dependent calculation are well understood. The effects of scattering on the solution can be studied to some degree by examining the role of scattering in the steady-state transport calculation. The steady-state transport model of *Lummerzheim and Liliensten* [1994] is used to compare the steady-state spherical intensity with and without scattering included in the model.

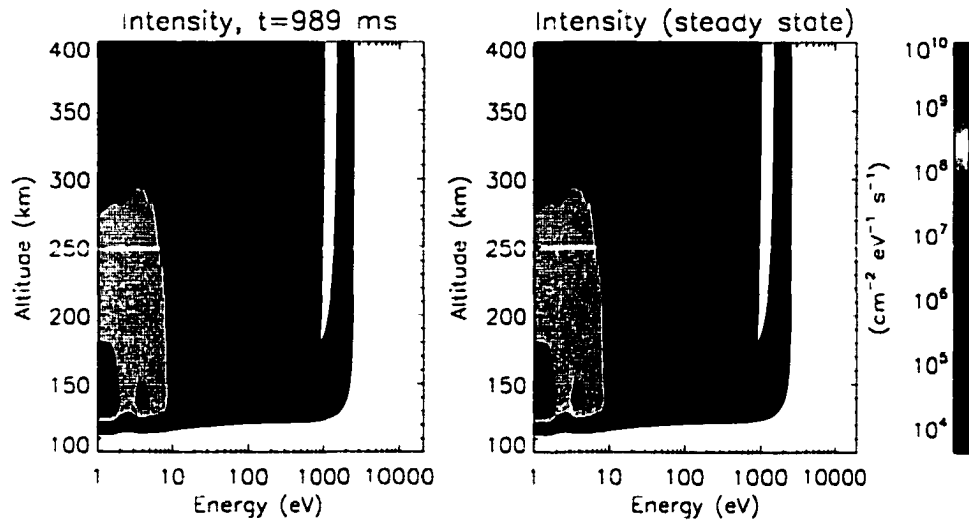


Figure 3.4. Comparing transport calculations. A 2-keV monoenergetic field-aligned precipitating-electron beam and the solution for the time-dependent (left) secondary calculation and the steady-state secondary calculation (right).

The steady-state transport code was run for three different upper boundary conditions with and without scattering. Each boundary condition consisted of a monoenergetic, field-aligned intensity, each with a different peak energy (700 eV, 2 keV, and 10 keV) and all with a downward flux of  $1 \text{ mW m}^{-2}$ . These conditions were chosen so the energy dependence of  $\bar{I}$  with and without scattering can be studied. The spherical intensities as a function of altitude and energy are shown in Figure 3.5 for each boundary condition with and without scattering. In Figure 3.5 (left) the intensities are the results of the calculations with scattering included and in Figure 3.5 (right) the intensities are the results of the calculations with scattering turned off. The top two plots show the 700-eV case, the middle plots show the 2-keV case, and the bottom plots show the 10-keV case. In each plot the precipitating beam can be seen at the higher energies with a large intensity of secondary electrons at energies below  $\sim 100$  eV. In order to understand the differences seen in the scattering *versus* no scattering cases, it is useful to discuss the physics of the electrons in this region of phase space.

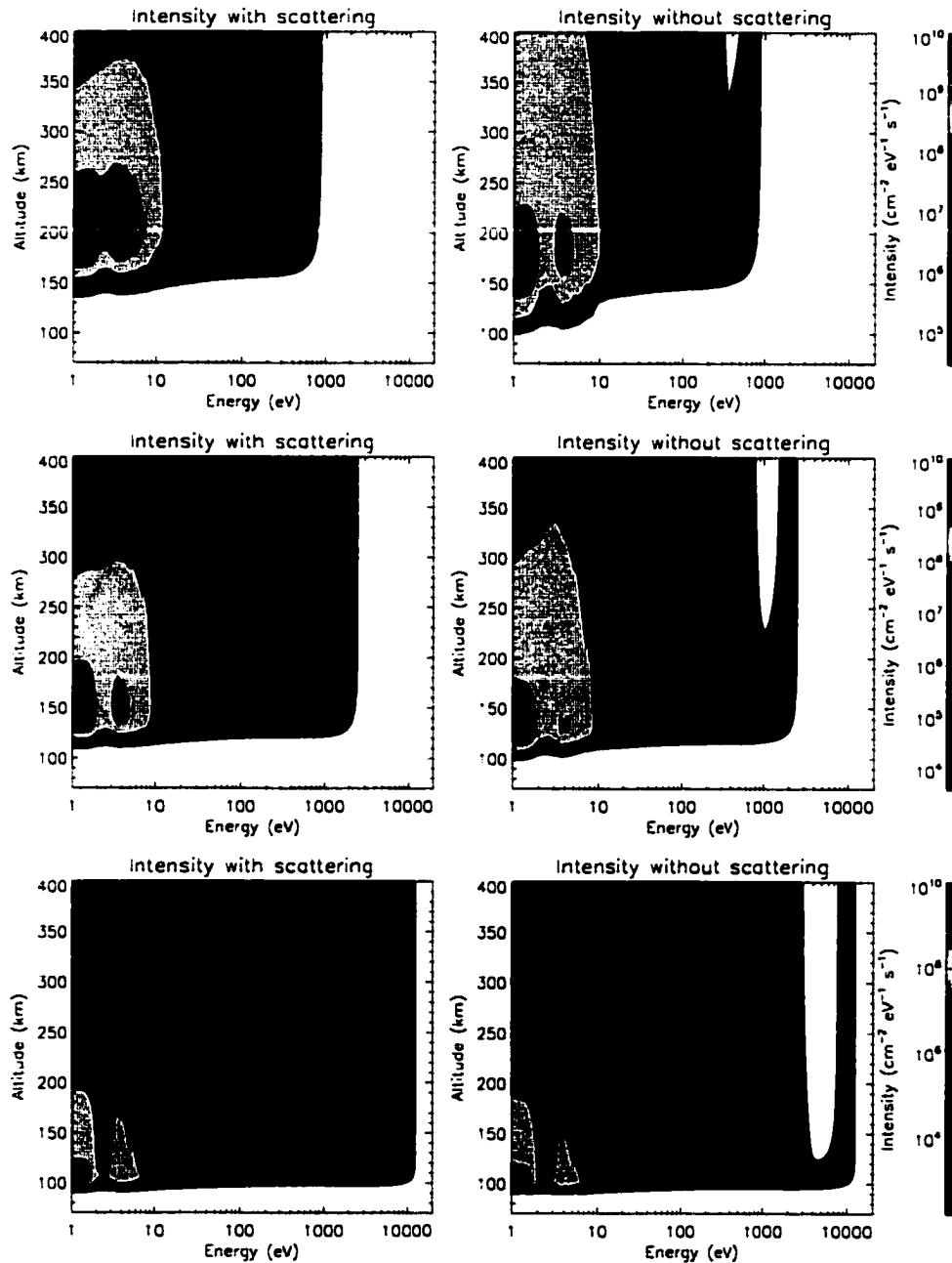


Figure 3.5. Spherical electron intensities for three beams of electrons. The beams have characteristic energies of 700 eV, 2 keV and 10 keV. These intensities were calculated using the steady-state transport model of *Lummerzheim and Lilensten* [1994] with and without scattering included. The plots on the left show the intensities for the case with scattering and the plots on the right were created with scattering turned off.

Because of their high energy, the probability of the primary electrons colliding elastically with the upper atmosphere at altitudes  $>150$  km is very small. When the electrons reach the lower ionosphere where the probability of colliding increases by orders of magnitude, they are scattered elastically. For most of the electrons, the pitch angle of high-energy electrons changes only by a few degrees due to the strongly forward-peaked phase function *Stamnes* [1978]. A small fraction scatter upward and have high enough energies that they have a small probability of colliding again with the upper atmosphere and they escape through the upper boundary. The other effect that the elastic scattering has on the electrons is to scatter them into different pitch-angles. If the precipitating beam is field-aligned along the magnetic field-line, as in our cases, the electrons will scatter into pitch-angles closer to zero degrees. Such electrons will have increased their spiral trajectory path length in an infinitesimal length along the magnetic field line. This increases the probability of an electron colliding with a neutral species at a particular altitude, which translates to an increase in the probability of depositing energy at a higher altitude than if an electron did not suffer an elastic collision. Thus there are two effects of elastic scattering on the precipitating electrons that can be noticed in Figure 3.5: the altitude of energy deposition is higher for the case including elastic scattering and the electron intensity is greater at energies between the peak of the monoenergetic beam and the broader distribution of the secondary electrons.

The height difference between the cases with and without scattering becomes less noticeable with higher precipitating electron energy, although the intensity difference due to the high-energy backscattered population just below the energy of the peak intensity remains prominent independent of the energy of the precipitating electrons. In the 700-eV plots of Figure 3.5, the electron intensity in the energy range from 100 eV to just below 700 eV differs by  $>100\%$  at altitudes  $>200$  km and the maximum energy deposition is different by  $\sim 30$  km. In the 2-keV (10-keV) case, the intensity difference begins at  $\sim 400$  eV (1 keV) and the height difference is  $\sim 15$  km (1 km).

Because of their low-energy, secondary electrons have a high probability of colliding elastically, even at altitudes  $>150$  km, and they have a smaller probability of colliding inelastically. This was noted above in the discussion regarding Figure 3.1. When these secondary electrons scatter elastically they become isotropic after only a few collisions since

the phase function for low-energy electrons is mostly isotropic. This means that roughly half the electrons will travel upward and half downward. Since the elastic collision cross sections are so high, there is a high probability that the electrons experience more collisions changing their directions only to collide again. In effect the elastic scattering acts to confine the electrons locally, whereas in the absence of elastic scattering the electrons can travel in altitude before an inelastic collision contributes to thermalization. This effect is shown in the secondary electrons in the plots in Figure 3.5 (right), compared to Figure 3.5 (left).

The effects of scattering on the spherical intensity, especially on the precipitating electron intensity, can also be seen in the ionization rate as shown in Figure 3.6. It is easier to use the ionization rate to quantify the differences that elastic scattering will have on the transport solution. The peak ionization rate from the 700-eV electron beam which does not scatter is  $\sim 20$  km lower in height and 28% larger in magnitude than the peak ionization rate from the 700-eV electron beam which does scatter. The 2-keV (10-keV) electron beam that does not scatter produces a peak ionization rate that is  $\sim 15$  km ( $\sim 5$  km) lower and 52% (21%) larger than the peak ionization rate from the 2-keV (10-keV) electrons which do scatter.

The conclusion from the above study is that for an accurate solution, scattering must be included in the calculation of the auroral transport equation. Elastic scattering has been shown to keep the low-energy electrons confined in a small altitude region. This can explain agreements between data and transport calculations using the assumption that transport of the secondaries can be neglected for altitudes  $< 150$  km [Vallance Jones *et al.*, 1991]. It has also been shown that the altitude at which the bulk of the precipitating electrons lose their energy varies depending on whether or not scattering is included in the transport equation. Because it is not currently possible to include the scattering term with the time-dependent term, an *ad hoc* method of obtaining more accurate results without including the scattering term has been developed for the precipitating electron equation. This is not necessary for the secondary electron equation since the transport term and the scattering term essentially cancel each other out.

The method of obtaining more accurate results without including scattering is to multiply the loss function,  $L_{en}(E, z)$  in Equation 3.5, by a factor of two. The factor was determined by comparing the ionization rates of three field-aligned electron beams sharply

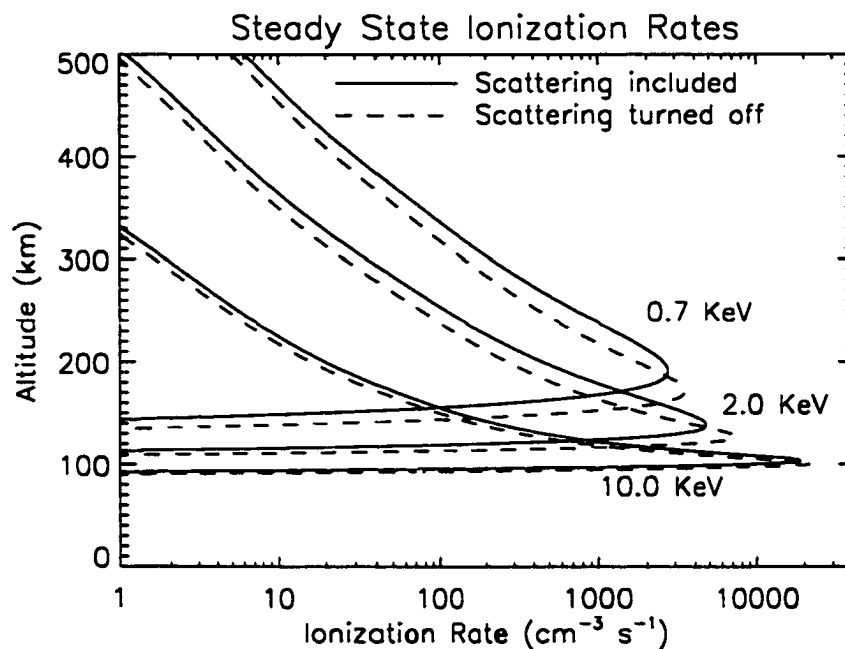


Figure 3.6. Ionization rates for three beams of electrons. The beams have characteristic energies of 700 eV, 2 keV and 10 keV. These ionization rate profiles were calculated by a steady-state transport model with and without scattering included. The solid line indicates the solution with scattering and the dashed line shows the solution with scattering turned off.

peaked at energies 700 eV, 2 keV and 10 keV calculated from the steady-state transport model with the steady-state ionization rates calculated from the time-dependent transport model. A different number was multiplied by the loss function for five simulation runs in order to find the number that produced the least error between the two calculations for all three beams. The number that gave the most accurate comparison is two. The comparison between the steady-state calculation and the time-dependent calculation (with the factor of two included), is discussed below. The number two seems reasonable since the inelastic and elastic cross sections are close in magnitude between 100 eV and 10 keV. This factor of two makes the solution more accurate in the altitude of the peak energy deposition in the time-dependent equation. However, this factor of two will not make up for the upward traveling electrons that fill out the spherical intensities at energies above the secondary electron energies. These electrons are responsible for the ionization rate at altitudes just above the

altitude of the peak ionization rate. By comparing the steady-state calculation with the time-dependent calculations after they have reached steady state it is possible to determine the percent error of the spherical intensities, as well as the emission and ionization rates, calculated with this time-dependent transport calculation.

Four different upper boundary conditions are used to compare the steady-state computer model with the time-dependent transport calculation: three monoenergetic intensities represented by a Gaussian distribution in energy with peak energies of 700 eV, 2 keV, and 10 keV. The loss function in every case is multiplied by two. Maxwellian energy distributions are often measured by instruments on rockets flying through the aurora and so the fourth upper boundary condition studied is a Maxwellian energy distribution function with a characteristic energy of 1 keV (mean energy of 2 keV). The four cases all have a downward energy flux of  $1 \text{ mW m}^{-2}$ . Both the steady-state and the time-dependent calculations use the same MSIS-90 atmosphere, the same IRI93 ionosphere, and the same cross-section set. The ionization rates and spherical intensities of each different spectrum are shown on four different figures: 3.7, 3.8, 3.9, and 3.10. In each of these figures, the ionization rates of the steady-state calculation with and without scattering are plotted along with the time-dependent ionization rate once steady state has been reached. Three contour plots of the spherical intensities are also shown as functions of energy and altitude.

In Figures 3.7, 3.8, 3.9, and 3.10 there are some very clear differences between the steady-state and the time-dependent calculations. The differences in the secondary intensities of the steady-state cases without scattering and the time-dependent cases in the four figures (bottom 2 plots) are clearly due to the non-scattering discussion above and the assumption of no transport of the secondary electrons in the time-dependent case. The intensities of precipitating electrons in these two cases are quite similar, as they should be. However, there are differences in the electron intensity just below the characteristic energies. The steady-state, non-scattering calculation shows more intensity at these energies than does the time-dependent code. There are two factors that contribute to this difference: the CSDA and the energy discretization.

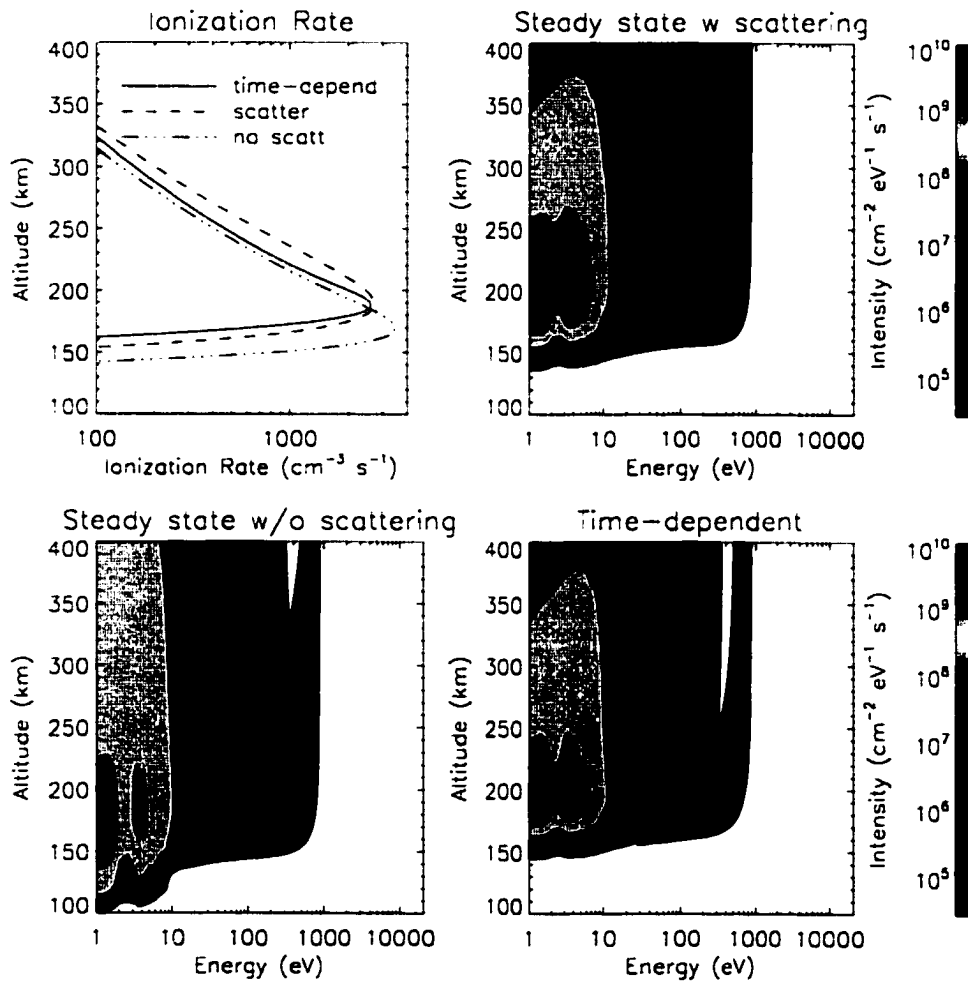


Figure 3.7. 700-eV field-aligned monoenergetic electron beam comparisons. Ionization and spherical intensity are shown.



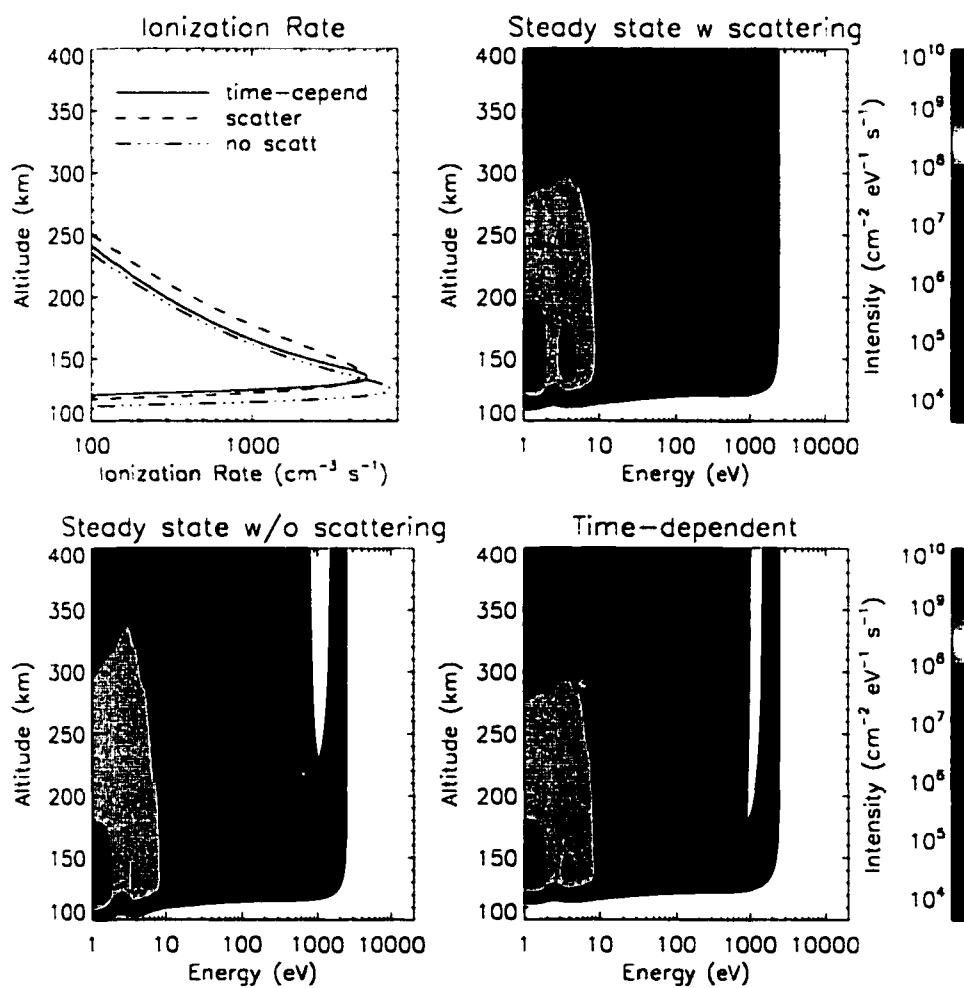


Figure 3.8. 2-keV field-aligned monoenergetic electron beam. Ionization and spherical intensities are shown.

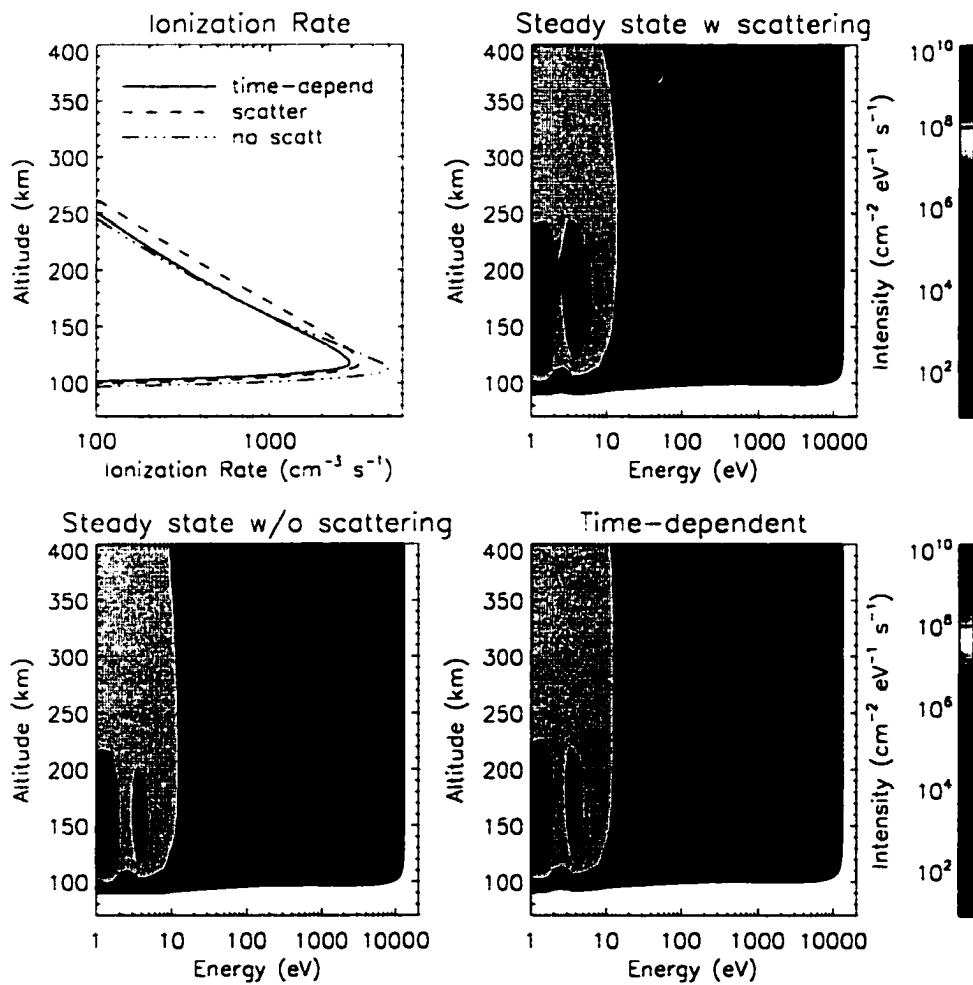


Figure 3.9. 1-keV field-aligned Maxwellian electron beam comparisons. Ionization and spherical intensities are shown.

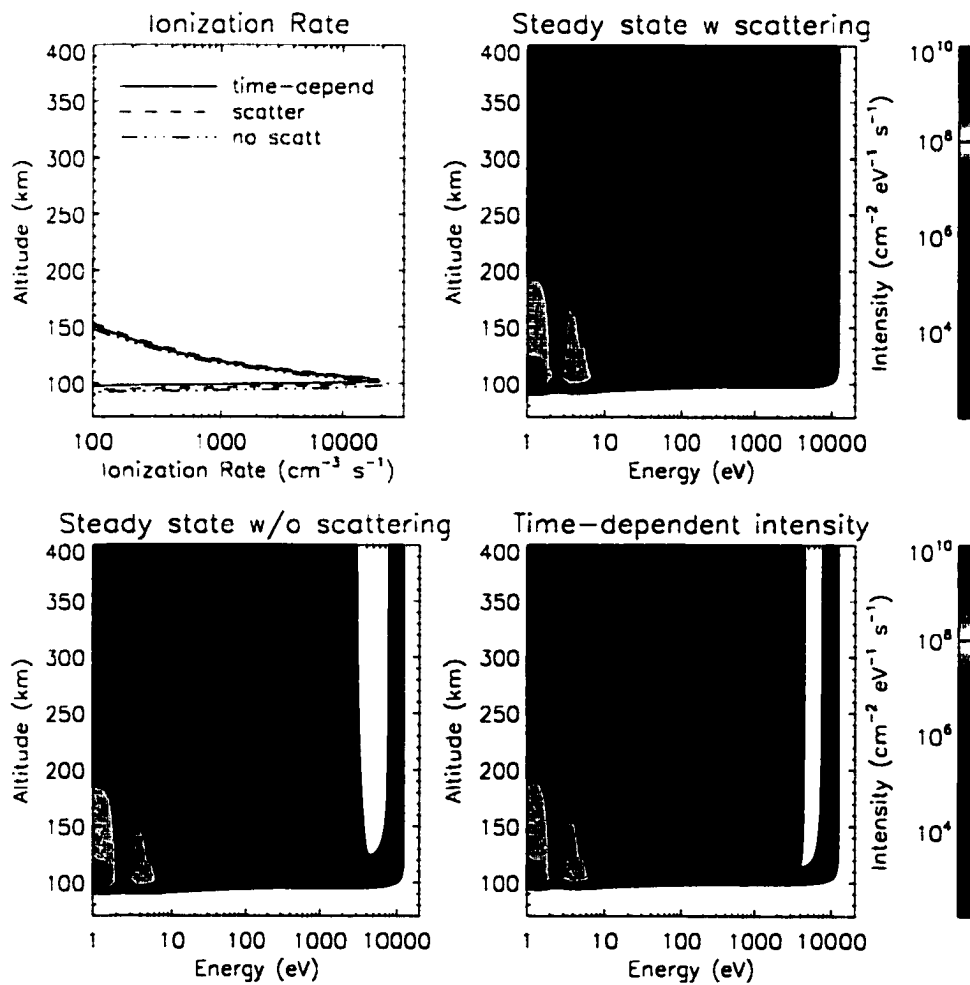


Figure 3.10. 10-keV field-aligned monoenergetic electron beam. Ionization and spherical intensities are shown.

The CSDA is used in the time-dependent calculation as a first approach to solving this equation, even though it is not valid at energies below 3 keV. Errors will occur in the high-energy intensity where the differences are seen in the bottom two contour plots of Figures 3.7, 3.8, 3.9, and 3.10. This is due to the fact that an integral collision term acts to move a fraction of all the higher energy electrons to each lower energy depending on the probabilities of colliding and losing different amounts of energy. The derivative collision term acts to continuously lose energy at a specific rate. With high-energy upper boundary conditions, like the 10-keV beam in Figure 3.10, the difference should not be large because the fraction of energy lost in a collision is low in comparison to the energy of the beam. But with a lower energy beam as with the 700-eV beam in Figure 3.7, where the collision cross sections are high, the fraction of energy lost is large. Not only will there not be enough electrons at higher altitudes and energies just below the beam energy, but since the beam does not lose enough energy at the high altitudes, it will deposit the bulk of its energy too low in the atmosphere. Because the difference in the non-scattering and time-dependent calculations decrease with increasing characteristic energy beams, the CSDA clearly changes the solution at lower energies. The way that the energy discretization is calculated may account for the difference in the two calculations for the high-energy upper boundary condition calculations.

The comparison between the non-scattering and time-dependent calculation is the best for the Maxwellian spectrum in Figure 3.9. Since the Maxwellian spectrum has a large energy spread, the errors in the energy loss approximations will be small compared to the intensity in the lower energy regions.

The comparison between the steady-state case including scattering and the time-dependent case is the important comparison since the fewest assumptions are used in the steady-state case with scattering. It is clear that in all figures: 3.7, 3.8, 3.9, and 3.10, there is a marked difference between the high-energy intensities just below the characteristic energy of the precipitating electron beam. This is primarily due to the lack of scattering in the time-dependent transport code. It is interesting to note that the precipitating electron intensities in Figure 3.9 are similar above  $\sim 3$  keV. This is a good indication that below 3 keV, scattering is most important. The secondary intensities are quite similar from the time-dependent calculation and the steady-state calculation including scattering. It can be

concluded that the assumptions made for the time-dependent secondary transport equation are valid for modeling these spherical intensities.

The difference between the ionization rates of the scattering case with the time-dependent case was calculated at the peak ionization rate shown in Figures 3.7, 3.8, 3.9, and 3.10. The difference in the calculations is 7% in the 700-eV beam, 11% in the 2-keV monoenergetic beam, 20% in the 1 keV Maxwellian beam, and 1% in the 10-keV beam. The column integrated ionization rates, which are proportional to the emission rate used later in the thesis as well as proportional to the energy conservation, is  $\sim 40\%$  less for the time-dependent calculations than for the steady-state calculations. The large differences of 40% in the altitude dependent ionization rate occur just above the peak ionization rate where scattering would fill in the ionization rate. This effect has not been compensated for by doubling the loss function.

It has been shown that by increasing the inelastic scattering by a factor of two and by not transporting the secondaries in altitude, it is possible to obtain solutions to the time-dependent equation in the steady state limit that agree with the steady-state calculation to within 20-40%. To increase the accuracy of the time-dependent solution, it would be best to include the scattering integral, increase the energy grid to higher energies, calculate discrete energy losses instead of using the CSDA, and combine Equations 3.5 and 3.6 in a single equation. However, a calculation that does not use the assumptions made here will require large amounts of computer resources. The time dependence of auroral electrons has been assumed to be unimportant due to the high energies of the electrons and the relatively thin region of the upper atmosphere that affects the electrons. This is the first calculation to examine the relevance of a time-dependent auroral electron transport calculation and its importance is shown in Section 3.3 and in Chapters 4 and 5. Although the solution, after reaching steady state, can differ from a steady-state solution by 40%, new insights into the electron transport problem have been gained by solving the time-dependent equation, so read-on!

### 3.3 Time-Dependent Solutions

In order to compare and contrast some of the time-dependent features of precipitating electrons with different incoming electron intensities, the transport equation is solved for five different electron spectra as upper boundary conditions. Each spectrum is “turned on” at  $t = 0$  (at the beginning of the computer run) and the precipitation is maintained for 150 ms at which time the electron spectrum is “turned off” completely and the system is allowed to decay. Four of the five spectra are monoenergetic (sharply peaked) electron intensities represented by a Gaussian distribution in energy,

$$I(E, \mu) = \frac{Q_o}{2\pi^{3/2} E_a E_p \bar{\mu}} \exp \left[ - \left( \frac{E_p - E}{E_a} \right)^2 \right], \quad (3.14)$$

where,  $Q_o$  is the downward integrated flux,  $E_a$  is the half-width,  $E_p$  is the peak energy as well as the mean energy,  $\langle E \rangle$ , and  $\bar{\mu}$  is the mean value of  $\mu$  that the electrons have. The fifth upper boundary condition is a Maxwellian distribution in energy,

$$I(E) = \frac{Q_o E}{4\pi E_c^3 \bar{\mu}} \exp \left( - \frac{E}{E_c} \right), \quad (3.15)$$

with a characteristic energy,  $E_c$ . The Gaussian electron intensities have peak energies,  $E_p$  of 700 eV, 2 keV, 2 keV, and 10 keV and half-width,  $E_a$ , of 10% of their peak energies. The Maxwellian intensity has a characteristic energy 1 keV and a mean energy of 2 keV. Three out of four of the Gaussian electron intensities (700 eV, 2 keV, and 10 keV) and the Maxwellian electron intensity are cold, field-aligned electron beams which means that they have no intensity in any pitch angles other than the pitch angle parallel to the magnetic field. Numerically this is done by only using only  $\mu = 1$  in Equations 3.5. The fourth Gaussian electron intensity has an energy of 2 keV and a downward pitch angle distribution that is isotropic. These types of upper boundary conditions are chosen to study the effects of the time-dependent transport of electrons with different energies (Gaussian spectra), with a spread in energy (Maxwellian spectrum) and with a spread in pitch-angles (isotropic downward spectrum).

For the isotropic study, it is important to provide a pitch angle distribution that will not mirror, since I do not include the mirror force in the equations. Including electrons that should mirror but do not can lead to an error in travel time of up to 50%. An electron with

a pitch angle greater than  $66^\circ$  at 630 km on a field line that has its footprint at College, AK will mirror above 300 km. If I include 2-keV electrons with a pitch-angle of  $77^\circ$  at 630 km in the transport equation (without the mirror force) they would take 76 ms to reach altitudes at which they would lose the bulk of their energy. The electrons that will not be affected by the mirror force will take less time. For example, 2-keV electrons with pitch angles of  $63^\circ$  at 630 km will take only 37 ms to reach altitudes where they will lose the bulk of their energy. Only electrons with pitch angles less than  $66^\circ$  are included in the isotropic upper boundary condition.

The time evolution of pulses with the described boundary conditions are shown in Figures 3.11, 3.12, 3.13, 3.14, and 3.15. Each calculation is started from an altitude of 630 km. These figures show the spherical electron intensity calculated by the method discussed in Section 3.2.2. The spherical intensities in these figures include the effects of the higher probability of elastic collisions and the lack of transport of the low-energy electrons that elastic scattering produces. However, the larger loss function and assumption of no low-energy electron transport will not simulate the time-dependence of scattering. The transport of secondary electrons would affect the time-dependence of the solution if it were included. The solutions to the time-dependent transport equation in this thesis and in these figures come to an steady state faster than if scattering and the secondary transport were included.

Each figure (3.11, 3.12, 3.13, 3.14, and 3.15) shows six contour plots of the spherical intensity as a function of energy and altitude at six different times. The time for each plot is the same in the following figures so that the different spectra can be compared. The minimum intensities are 1% of the precipitating beam intensity and the maximum intensity is  $1 \times 10^{10}$  electrons/(cm<sup>2</sup> eV s). The intensity at the given times shows 1) the precipitating electrons entering the ionosphere, 2) these electrons reaching the collision dominated atmosphere and losing their energy, 3) the secondary electron flux at its maximum just before the precipitating beams are turned off, 4) the secondary electron distribution after this beam has finished traveling into the atmosphere and has only left the secondary electrons, 5) the secondary electrons losing energy to the thermal electron population and depleting the secondary electron population at higher energies and 6) the same as 5) but a bit later in time.

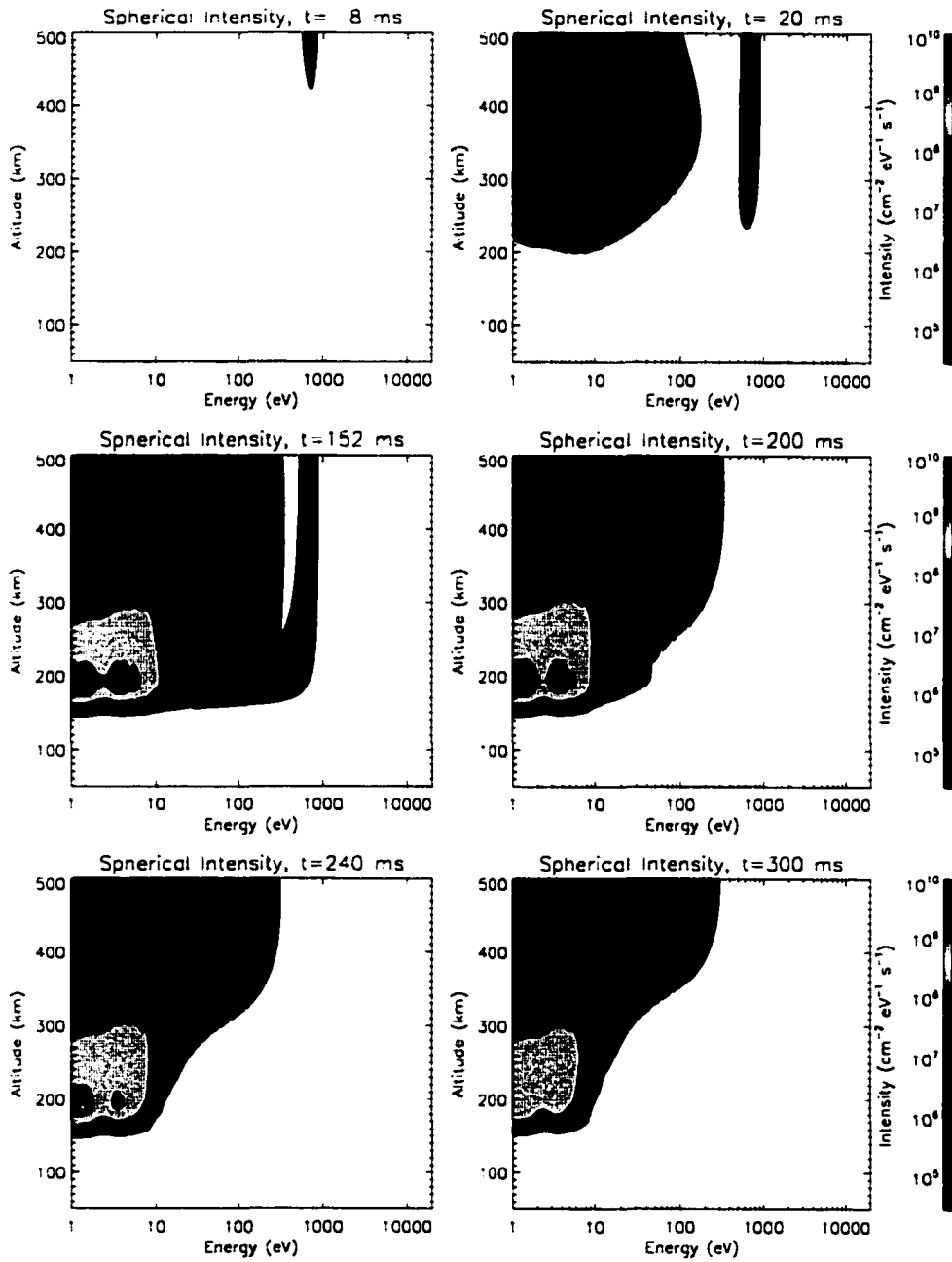


Figure 3.11. Time evolution of a 700-eV field-aligned Gaussian intensity.



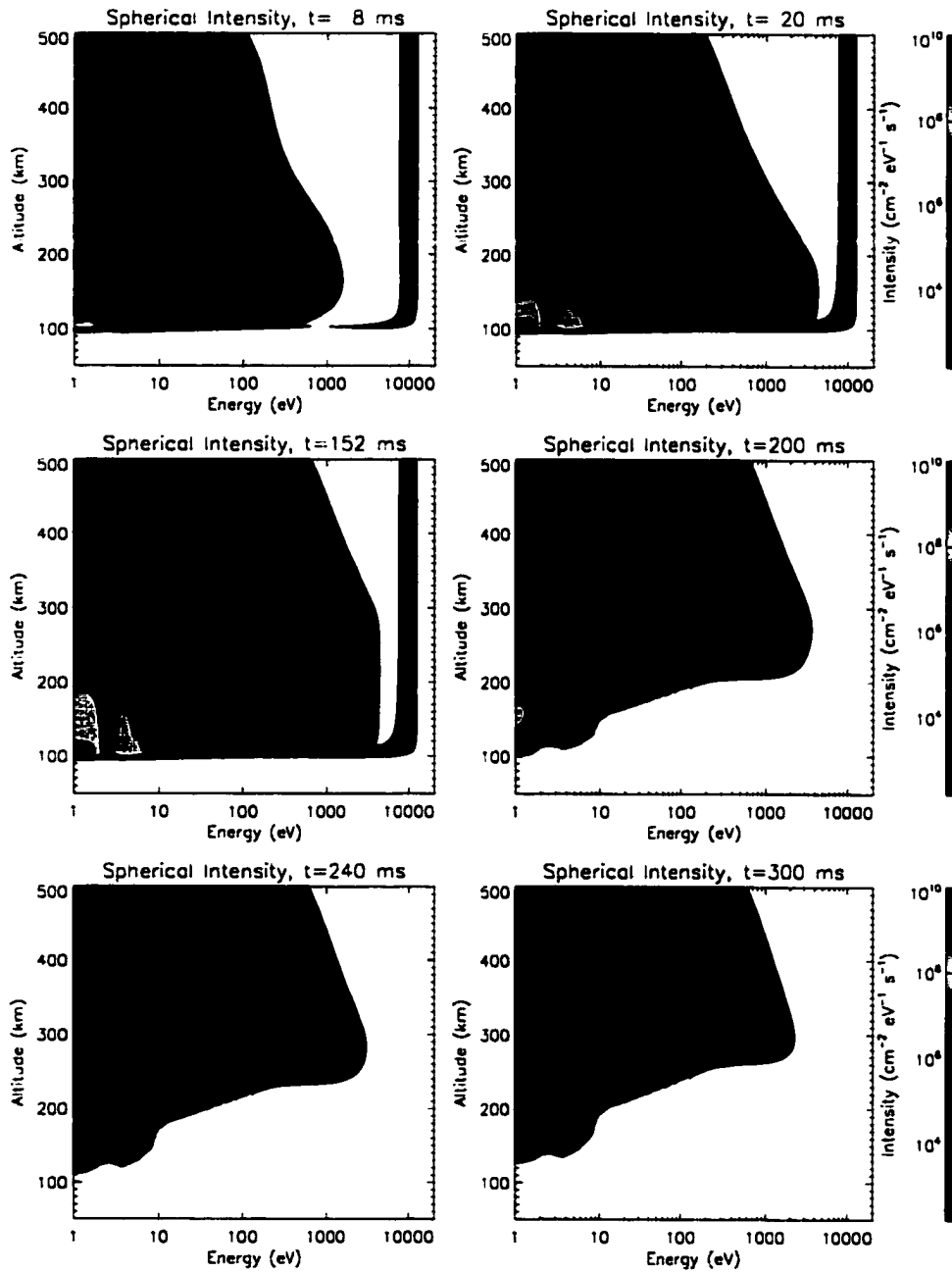


Figure 3.12. Time evolution of a 10-keV field-aligned Gaussian intensity.

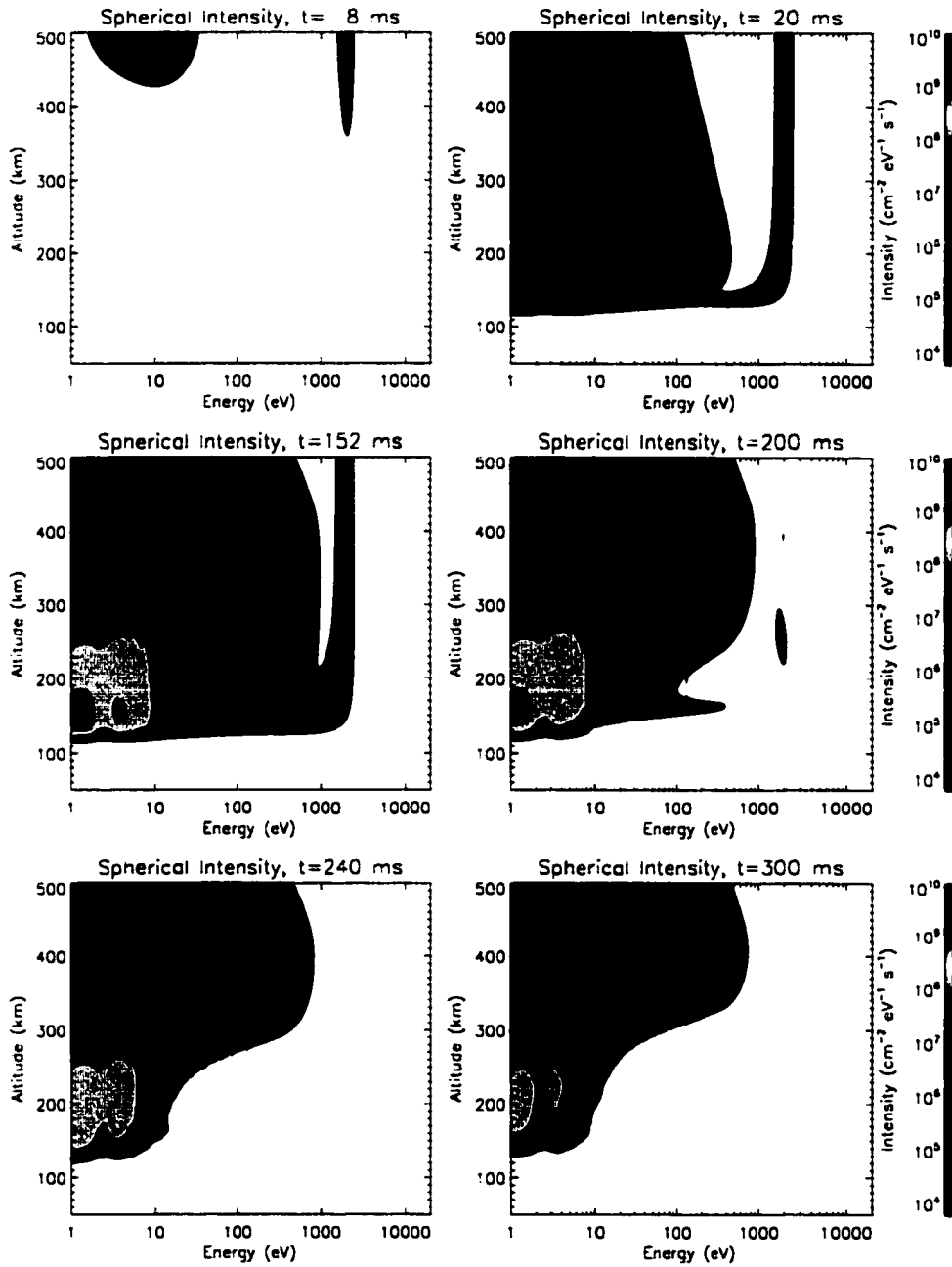


Figure 3.13. Time evolution of a downward isotropic 2-keV Gaussian intensity.

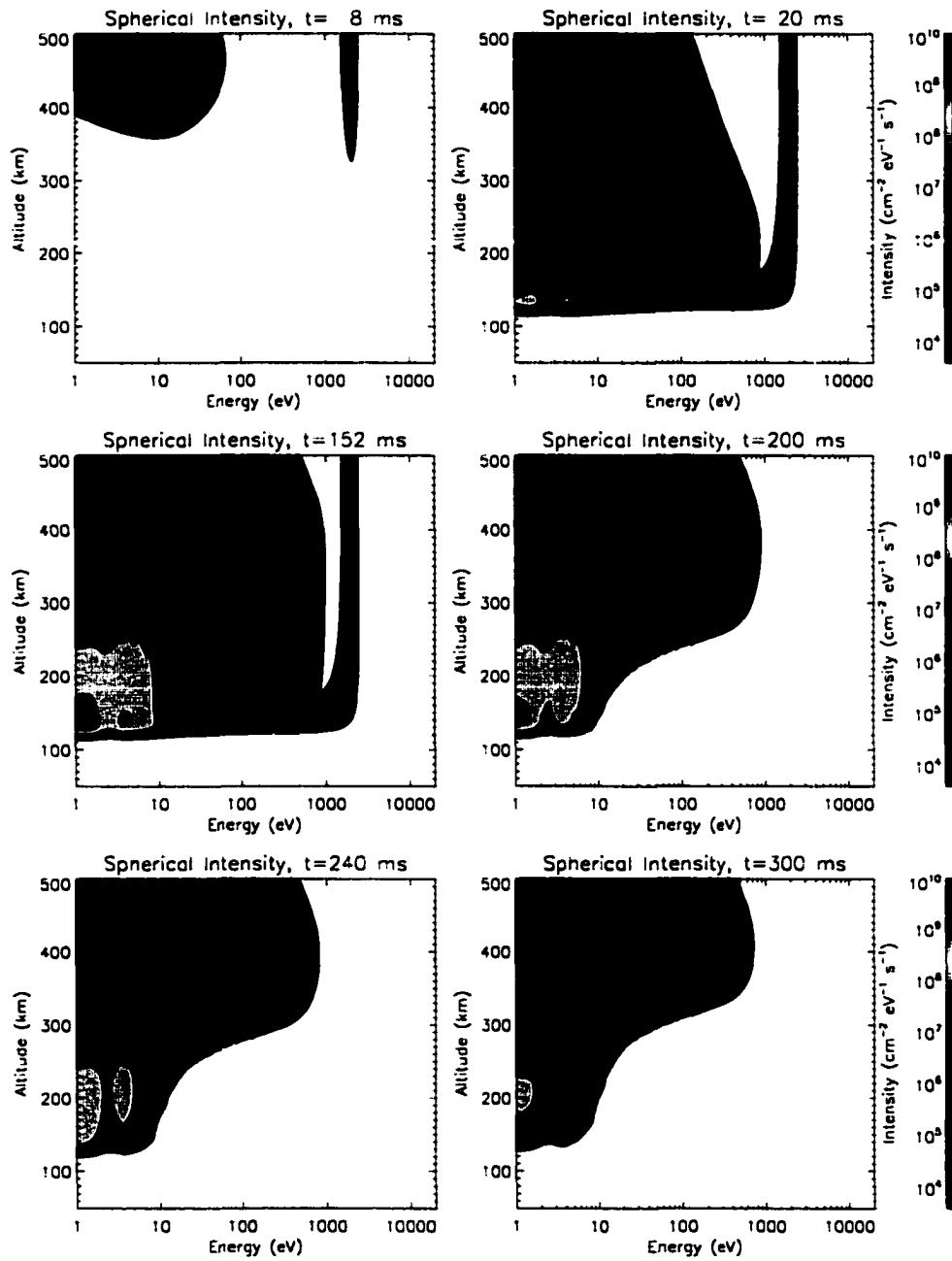


Figure 3.14. Time evolution of a field aligned 2-keV Gaussian intensity.

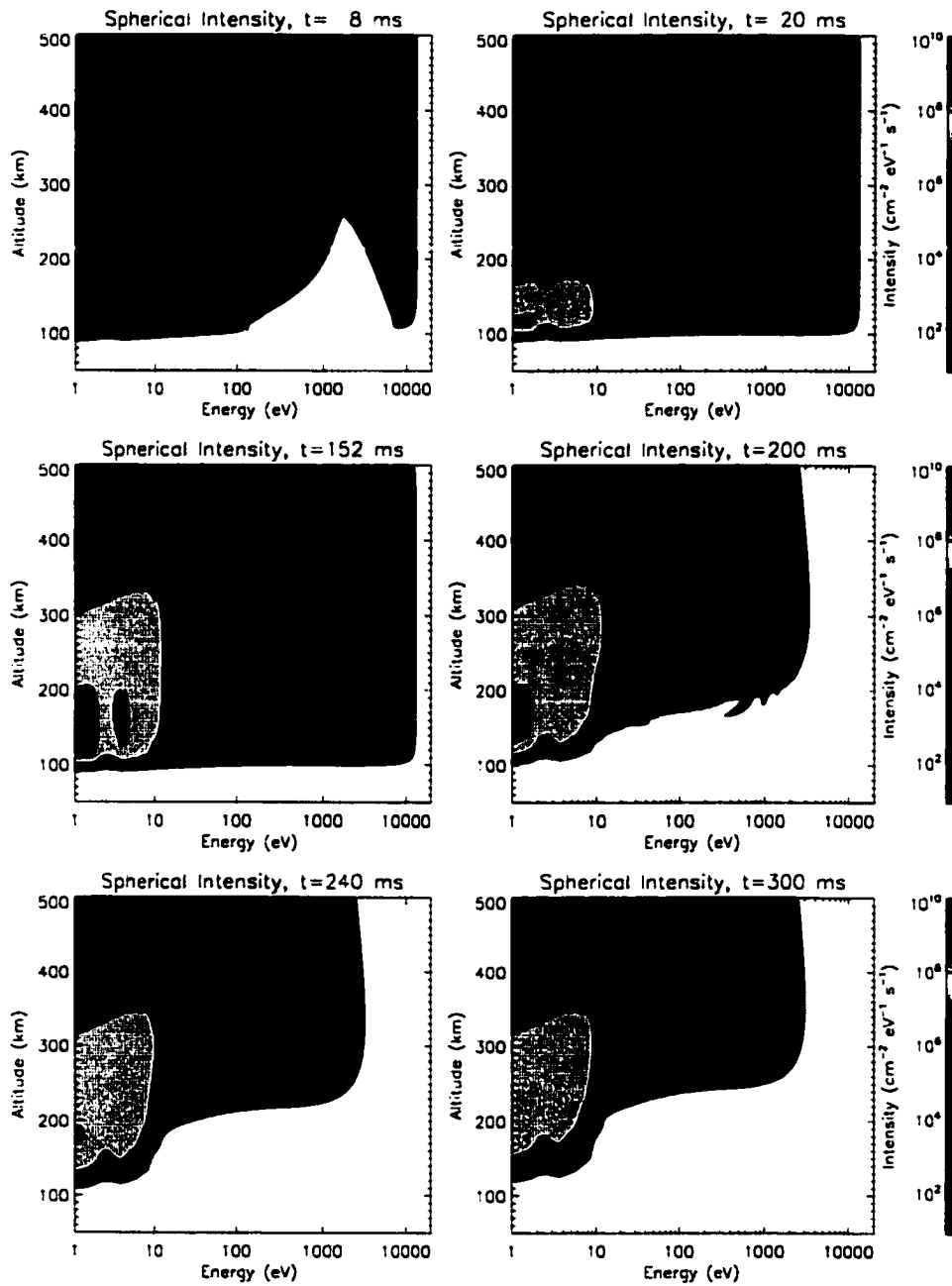


Figure 3.15. Time evolution of a field-aligned 1-keV Maxwellian intensity.

The first panel of each figure shows the electron intensity after 8 ms. By this time, the precipitating electrons have traveled into the ionosphere with a small percent colliding with the neutral atmosphere, losing energy and producing secondaries. However, since the probability of an electron colliding with a neutral atom above 300 km is very small, the precipitating electron intensity does not change much above this altitude. This is especially true of the higher-energy electrons, which see a smaller collision cross section than the lower-energy electrons, as can be seen by comparing Figures 3.12 and 3.14. Also, the isotropic downward electron intensity changes more slowly at higher altitudes than the field-aligned electron intensity. This is due to the fact that the electrons at pitch angles closer to  $90^\circ$  ( $\mu = 0$ ) will stay near an altitude longer since its parallel velocity is less. This effect is already seen in the first plots of Figures 3.14 and 3.13. Because the 1-keV Maxwellian electron intensity has a greater spread in energy, the high-energy electrons have already begun producing secondary electrons low in ionosphere at 8 ms, as seen in Figure 3.15. At this time in Figure 3.15 the velocity dispersion can be seen in the electrons as they propagate into the ionosphere because of the spread in energy of the Maxwellian spectra.

The second plots in Figures 3.11, 3.12, 3.14, 3.13, and 3.15 show the electron intensity after 20 ms. The 700-eV electrons are still propagating into the ionosphere in Figure 3.11, whereas the 10-keV precipitating electrons have already reached the lower altitudes where they lose most of their energy and the secondaries are well on their way to reaching steady state (Figure 3.12). By this time, the effect of a different pitch-angle distribution as an upper boundary condition can already be detected in Figures 3.13 and 3.14. In Figure 3.14, the 2-keV field-aligned electron intensity has reached the lower ionosphere and has begun to lose the bulk of its energy. Since the electron intensity in Figure 3.13 began as an isotropic downward distribution instead of field-aligned at 630 km, not as many electrons have reached the lower ionosphere. There are fewer secondaries produced at the lower altitudes for the isotropic case in Figure 3.13 than in the field-aligned case in Figure 3.14. But at higher altitudes, more secondary electrons have been created in the isotropic case than in the monoenergetic case. Since the Maxwellian upper boundary condition contains electrons with a spread in energy, the intensity at 20 ms for Figure 3.15 is very different than the 2-keV monoenergetic intensity in Figure 3.14. The low-energy precipitating electrons from the low-energy region of the Maxwellian distribution are still propagating into the

ionosphere, whereas the 2-keV electrons have already reached the lower atmosphere where most of their energy is lost.

These figures for the time evolution of the electron intensity also show that as time progresses, the precipitating electron intensity reaches a steady state but the secondary intensity continues to increase. This can be seen in the four Gaussian intensity figures, but especially well in the 10-keV case, Figure 3.12. The secondary electrons take longer to reach steady state since the loss of the suprathermal electrons in energy depends on the value of the electron intensity and the inelastic cross sections in this energy region. Since the inelastic cross sections below 10 eV are smaller than ionization cross sections and since they represent a smaller energy loss than an ionization energy loss, the electron intensity below 10 eV must be larger than at the electron intensity at 100 eV before the loss is equal to the source and steady state is reached. The initial energy distribution has a large effect on the time dependence of the electron intensity in phase space. A more quantitative analysis of the 2-keV, monoenergetic intensity with  $\mu = 1$  is discussed below.

At  $t = 152$  ms, all of the intensities at the upper boundary of 630 km have been turned off. At this time, none of the configurations have reached steady state as defined by the calculations using the steady-state secondary equation. The spectra closest to approaching steady state is the 1 keV Maxwellian intensity in Figure 3.15 and the spectra farthest from approaching steady state is the isotropic 2-keV monoenergetic intensity in Figure 3.13.

After the intensity at the upper boundary has been set to zero, the electrons continue to propagate into the ionosphere until reaching the collision dominated atmosphere where they lose their energy to the atoms and molecules and eventually to the thermal electrons. In the five figures discussed in this section, it is important to realize that electrons with energies greater than about 100 eV should no longer be found in the plots at  $t = 200$  ms or greater since these electrons would have transported down, a fraction losing their energy to the atmosphere and the rest scattering out of the atmosphere. As discussed in Section 3.1.1, the time-dependent calculation does not include scattering nor secondary electron transport in altitude. In the decay of the intensities shown in the figures in this section, these two assumptions lead to large errors above  $\sim 200$  km.

Knowing the limitations of the model, it is still possible to order the different spectra in terms of decay time. As would be expected, the 10-keV monoenergetic field-aligned intensity

is the fastest to decay (Figure 3.12) since such high-energy electrons will penetrate lower into the upper atmosphere where the collision frequencies are highest. The 700-eV monoenergetic field-aligned intensity is the slowest to decay (Figure 3.11) since 700-eV electrons take the longest to reach the height at which they deposit most of their energy. Of the spectra with mean energies of 2-keV, the Maxwellian field-aligned intensity (Figure 3.15) decays first, then the Gaussian, field-aligned (Figure 3.14) and last of these three, the Gaussian, isotropic intensity decays (Figure 3.13). Since many of the auroral electron intensities measured by instruments flown through the aurora are Maxwellian and isotropic [Arnoldy, 1981], the decay time of such intensities will depend strongly on the characteristic energy of the Maxwellian. If the energy is high, then the decay time will be fast as with the Maxwellian field-aligned intensities. But, if the Maxwellian is low in energy, then the time between the parallel electrons depositing their energy to the atmosphere and the more perpendicular electrons depositing their energy will be larger. The decay time will then be significantly slower than the decay time for a Maxwellian field-aligned intensity.

The question of how long it takes the electron intensity to reach steady state is examined more closely using the 2-keV, monoenergetic, field-aligned electron beam which is turned on for 1 s. The precipitating electron distribution function reaches steady state rapidly, within 30 ms (15 ms taking into account the numerical errors discussed in Section 3.2.2). The secondary electron spherical intensity takes longer to reach steady state, from 75 ms for altitudes at 140 km to 470 ms for altitudes at 220 km. In Figure 3.16, a plot is made of the time required for the intensity from 1 eV and above to reach steady state at specific altitudes. Note that the time to steady state is longest for low energy electrons like those with energies at 1 eV and the numerical errors are smallest for these energies. Obtaining values for heights greater than 220 km was too difficult since the intensity changed so slowly. This is also the altitude range where the modeled decay would be most unreliable due to the limitations from the model assumptions.

The time-dependence of the intensity should be related to an exponential [Cercignani, 1998, pg. 180], as seen by the form of the transport equation written as

$$\frac{\partial I}{\partial t} = LI, \quad (3.16)$$

where  $L$  is a linear operator including all the terms from Equation 3.5 or Equation 3.6.

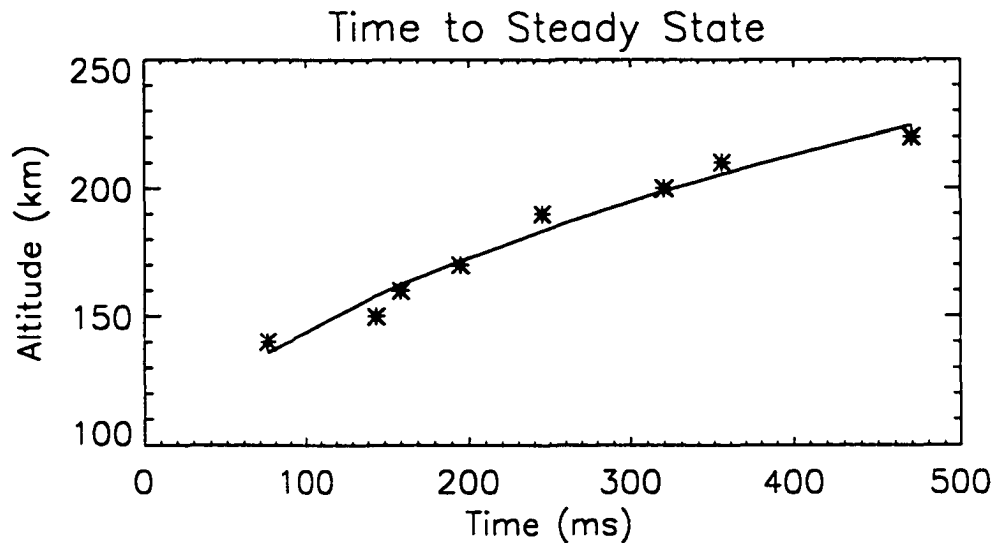


Figure 3.16. The time to reach steady state. The time it takes for the electron intensity of a 2-keV monoenergetic field-aligned incident electron beam to reach steady state as a function of altitude. The stars were taken by noting at what time the intensity stopped changing at that time. The line is a log function fitted to the stars (see Text for details).

Also, the collision frequency will decrease exponentially. Thus, a logarithm was fit to the time *versus* altitude plot in Figure 3.16. It was found that the function

$$z(t) = 103 * \ln(t + 213) - 446 \quad (3.17)$$

fits these values, where  $t$  is in ms and  $z$  is in km. With this function it is possible to extrapolate to later times. It is found that at  $t = 650$  ms the intensity should reach a steady state at 250 km and for  $t = 1.19$  s, at 300 km.

In this Chapter, numerous assumptions that were needed in order to solve the time-dependence in the transport equation were discussed. These assumptions, as well as the method used to solve the equation, have enabled solutions to be found for various time-dependent upper boundary conditions of the electron intensity. The time of exponential decay of the electron intensity out of the simulation box as well as the time to steady state can be examined more easily by looking at ionization and emission rates of the five cases studied in this chapter as a function of altitude and is examined in detail in Chapter 4. In the next two chapters, I use the solutions to the time-dependent transport equation to



**study the ionization and emission rates for the electron spectra adopted in this chapter and for flickering aurora.**

## Chapter 4

# Time-Dependent Emission Rates

Optical observations of the aurora are important because they can provide spatial, temporal and spectral information about the aurora. A spectrum of the aurora comprises families of line and band emissions due to neutral or ionized N<sub>2</sub>, O, O<sub>2</sub>, and N [Vallance Jones, 1974]. Broadband (white light) cameras and imagers observe the different forms, sizes and motions in the aurora and are often used to infer mechanisms that create these auroral morphologies and motions [e.g., Cresswell, 1969; Hallinan and Davis, 1970; Hallinan, 1976; Shepherd et al., 1990]. Spectrometers are used to infer the mean energy and energy flux of the electrons creating the aurora [e.g., Rees, 1963; Strickland et al., 1989; Vallance Jones and Gattinger, 1990], which can then be used to identify magnetospheric processes associated with a particular type of aurora. Spectral measurements are also used to study the physics and chemistry of the auroral ionosphere and upper atmosphere [e.g., Rees et al., 1988; Rees and Lummerzheim, 1991; Sivjee and Shen, 1997; Hallinan et al., 1998]. Optical instruments are also used with various other types of instruments to study both the auroral ionosphere [e.g., Lanchester et al., 1994; Stoker et al., 1996] and the auroral acceleration region [e.g., Frey et al., 1996; Stenbaek-Nielsen et al., 1998]. However, none of these optical measurements are made on millisecond time scales.

Optical instruments have recently been developed that can make measurements at millisecond resolution or less, such as the high-speed imager at the University of Alaska, Fairbanks which has a frame rate of 1000 frames/second [Hans Stenbaek-Nielsen, *personal communication*], a 16-channel high-speed photometer [McHarg et al., 1998], and a 52-channel

multi-anode fast photometer (MFP) [Sakanoi and Fukunishi, 1999]. McHarg *et al.* [1998] and Sakanoi and Fukunishi [1999] have used these instruments to study flickering aurora (see Chapter 5). Optical observations at millisecond time scales can be useful for studying the time dependence in the electron transport. The propagation of electrons through the upper atmosphere creates optical emissions that will vary on these time scales. In this chapter, time-dependent optical emissions at millisecond resolution are modeled to evaluate the importance of the time dependence in electron transport on optical auroral emissions. Both the altitude dependence of emission rates and column integrated emission rates are studied. Since the term “electron intensity” can easily be confused with emission intensity, the term “differential flux” will be used when referring to the spherical electron intensities studied in Chapter 3.

## 4.1 Modeling Emissions

Most optical aurora are the consequence of electrons colliding with the upper atmosphere, leaving neutrals and ions in vibrationally and electronically excited states, thus producing altitude-dependent optical emissions and ionization. However, the resulting optical emissions are not all directly proportional to the excitation rate. As Lummerzheim [1987] states on page 51:

Other mechanisms contribute to both the population and de-population of excited states. De-excitation occurs by quenching (collisional deactivation), dissociation, chemical reaction, and radiation. Besides direct electron impact, population of an excited state is possible by cascading, chemical reactions, photon absorption, and thermal electron excitation.

The emissions that are the easiest to model and that contain the least uncertainties are those that are populated only by direct electron impact and are de-excited promptly by radiation. In this case, the emission rate of a particular state is equal to the emission rate,  $\eta_j^k$ , in Equation 3.2. To model a particular band emission, more information is needed. The Franck-Condon factor is, to a good approximation [Vallance Jones, 1974], the probability of excitation between the ground vibrational state,  $v'''$ , and the excited vibrational state,  $v'$ .

This factor and the Einstein transition probability,  $A(v', v'')$ , together with the excitation rate,  $\eta_{v'}^t$ , can provide the emission rate for a particular band emission.

A differential volume of space in the optical aurora radiates light in all directions at a particular rate (the emission rate). What instruments measure is the light that reaches the instrument from multiple radiating layers that pass through the lower atmosphere to the instrument. This light is interpreted as due to a single luminous surface of brightness,  $B$ , for non-point sources. For an optically thin ionosphere, the light of a particular wavelength that reaches the instrument is the column integrated emission rate along the line of site. The brightness is often given in Rayleighs. Since some auroral emissions are absorbed or scattered by the atmosphere, the measured equivalent brightness is not always equal to the surface brightness at the source. When the atmosphere is optically thin to an emission at wavelength,  $\lambda$ , the observed surface brightness,  $B$ , in Rayleighs is related to the emission  $B$  in photons  $\text{cm}^{-2} \text{sr}^{-1} \text{s}^{-1}$ , by the relation [Chamberlain, 1995]

$$B(\text{Rayleigh}) = \frac{4\pi}{10^6} B(\text{photons cm}^{-2} \text{sr}^{-1} \text{s}^{-1}). \quad (4.1)$$

For an arbitrary observing direction, calculating the equivalent surface brightness requires knowledge of the geometric shape of the aurora. Quantitative modeling of the observed surface brightness is best for observations in the magnetic zenith, since emission rates along a field line are modeled. In this chapter, emission rates are integrated along the field line to give a column integrated emission brightness which can then be compared with measured brightness of aurora in the magnetic zenith.

Unfiltered photometer, imager, and camera data are difficult to model since many emissions are not only the result of electron impact and prompt radiative de-excitation, but also include collisional reaction, quenching, and radiative lifetimes which span many orders of magnitude in time. The goal of this study is to model emissions that directly relate to the time changes in the electron differential number flux and can be observed using the ground based optical instruments mentioned above. The bright, visible emissions of atomic oxygen at wavelengths 6300 and 5577 Å have long radiative lifetimes of 134 s and 0.7 s respectively. Modeling these emissions would require including the effects of quenching and other collisional reactions. Since the electron differential flux changes in milliseconds, emissions from these states will not give direct optical response to the changing electron differential

flux. When evaluating broadband optical measurements in millisecond timescales, the long lifetime emissions may be treated as constant offsets in the optical brightness.

Molecular nitrogen is a source of bright emissions with lifetimes  $< 1$  ms. Such emissions are the first positive emission,  $N_2(1PG)$ , the second positive,  $N_2(2PG)$ , first negative,  $N_2^+(1NG)$ , and Meinel,  $N_2^+(\text{Meinel})$ . The upper and lower states for these emissions are given in Table 1.1. A partial Grotrian diagram for  $N_2$  is shown in Figure 4.1, which gives the potential energy of the states and vibrational levels as a function of internuclear distance. Such a diagram is useful for displaying the discrete energy levels of the  $N_2$  states and their vibrational levels.

Of the above mentioned states,  $N_2(1PG)$  and  $N_2^+(1NG)$  have been measured at high time resolution by *Sakanoi and Fukunishi [1999]*. The  $N_2^+(1NG)$  emission is suitable for modeling the optical emissions of the time-dependent electron transport but the  $N_2(1PG)$  emissions are complicated with cascading into the  $B^3\Pi_g$  state from  $C^3\Pi_u$  state (the  $N_2(2PG)$  emission) as well as from the A, W and B' states [*Cartwright et al., 1971; Shemansky and Broadfoot, 1973; Cartwright et al., 1973; Morrill and Benesch, 1996*]. The overlap in potential energy and internuclear distance is shown on in Figure 4.1 on the right panel. This emission is believed to be affected by collisional energy transfer between the B state and the A, W, and B' states to create the bright lower red border in type *b* aurora [*Morrill and Benesch, 1996; Hallinan et al., 1998*] because the lifetime of the state is  $6 \mu\text{s}$  and  $N_2$  will collide with other neutral atmospheric species. Because of these complications, the  $N_2(2PG)$  state is modelled instead. This emission is a better indicator of the electron transport, and since it cascades to the B state of the  $N_2(1PG)$  emission can be used in future studies of the time dependent  $N_2(1PG)$  emission rates. The  $3371 \text{ \AA}$  emission band is modelled since it is a commonly observed band even with the large atmospheric scattering effects [*Lummerzheim and Liliensten, 1994; Gattinger et al., 1991; Solomon, 1993*].

Besides being a prompt, bright auroral emission, the  $4278 \text{ \AA}$  band of  $N_2^+(1NG)$  is proportional to the  $N_2$  ionization rate [*Borst and Zipf, 1970*]. The changes in time of the  $4278 \text{ \AA}$  emission rate reflect the changes in time of the ionization rate. Because the  $N_2^+$  ionization cross section peaks at  $100 \text{ eV}$ , the time dependence in the  $4278 \text{ \AA}$  band will primarily reflect the time dependence in the degrading primary electrons as they loose their energy to the upper atmosphere. However,  $3371 \text{ \AA}$  band of  $N_2(2PG)$ , which cascade into  $N_2(B^3\Pi_g)$ ,

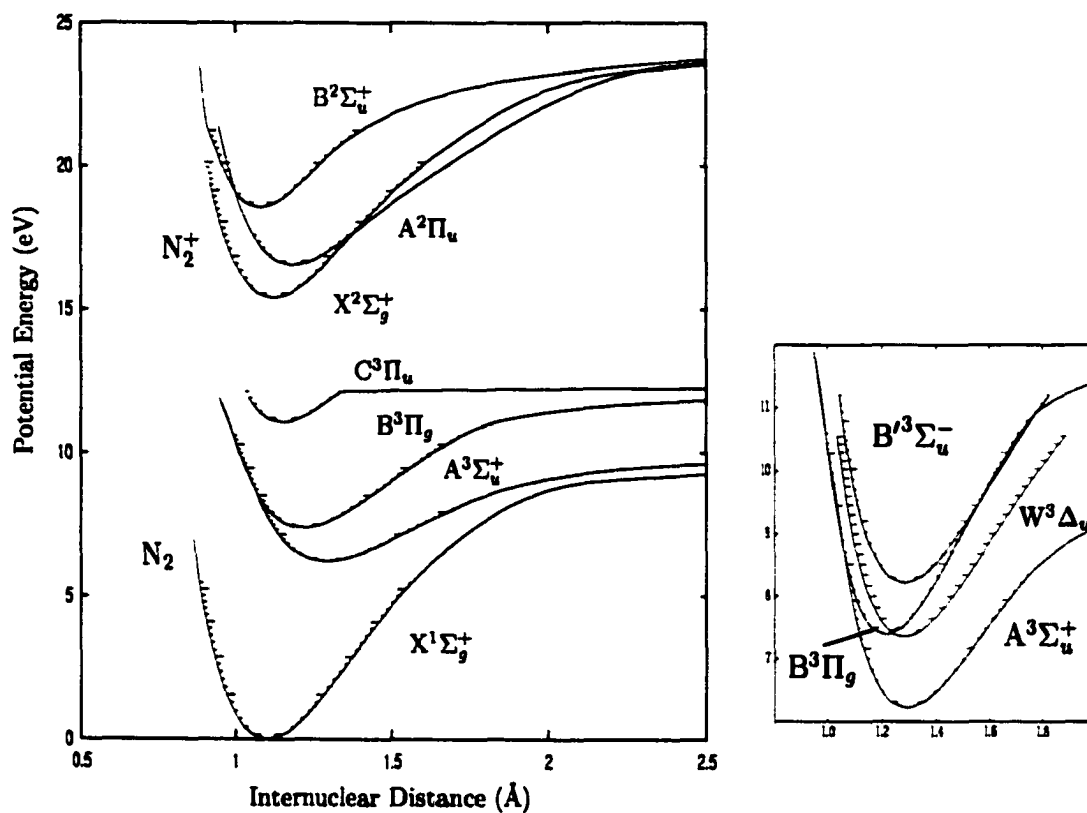


Figure 4.1. Molecular Nitrogen Grotrian Diagram.  $N_2$  Grotrian diagram adapted from *Heavner* [2000] showing potential energy curves for some electronic states with vibrational levels indicated by horizontal ticks. The expanded section in the lower right shows the  $N_2(B'^3\Sigma_u^-)$ ,  $N_2(B^3\Pi_u)$ , and  $N_2(W^3\Delta_u)$  electronic potentials energy curves and the corresponding vibration levels.

has its peak cross section centered at 14 eV. Thus, the time dependence in the  $N_2(2PG)$  emission will be related to the time dependence in the lower-energy secondary electrons. This difference in cross sections is another advantage to modeling these two emissions.

The 4278 Å emission rate is calculated by first using Equation 3.2 with the  $N_2^+$  ionization cross section and the  $N_2$  atmospheric densities to obtain the ionization rate of  $N_2$ . Then the excitation rate is multiplied by the branching ratio, 0.11, to obtain the excitation rate of the  $N_2^+(B^2\Sigma_u^+)$  state [Borst and Zipf, 1970; Doering and Yang, 1997]. Vallance Jones [1974] uses the Einstein Coefficients of Shemansky and Broadfoot [1971] and the Franck Condon factors of Nicholls [1969] to create a table of intensities of individual bands. This table, (Table 4.9 of Vallance Jones [1974]), is used here to calculate the fraction of the total excitation of the  $N_2^+(B^2\Sigma_u^+)$  state that goes from the zeroth vibrational level of this state to the first vibrational level of the  $N_2^+(X^2\Sigma_g^+)$  state, emitting a photon with the wavelength of 4278 Å. This procedure results in simply multiplying the  $N_2^+$  ionization rate with a factor of 0.022 (the branching ratio times the emission fraction) to obtain the 4278 Å emission rate.

Calculating the second positive emission rate is just as simple as the  $N_2^+(1NG)$  4278 Å emission since 90% of the  $C^3\Pi_u$  state is excited by direct electron impact and only 10% is populated through cascading from other states Tachibana and Phelps [1979]. To calculate the 3371 Å emission rate, the excitation rate of the  $C^3\Pi_u$  state is calculated using Equation 3.2 with the appropriate cross sections and  $N_2$  densities and the electron differential number flux. Then excitation rates are multiplied by the fraction of the total excitation that is emitted in the  $N_2(2PG)$  3371 Å band as calculated by Vallance Jones [1974] in Table 4.12. When comparing either the 4278 or the 3371 Å emission model calculations, it is important to account for atmospheric scattering. Gattinger et al. [1991] has estimated the transmission of 4278 Å (3371 Å) optical emissions from direct viewing of an auroral arc near the magnetic zenith to be as low as 0.64 (0.44).

The solution to the time-dependent transport equation for the five different upper boundary conditions in Section 3.3 (10-keV Gaussian, field-aligned; 1-keV Maxwellian, field-aligned; 2-keV Gaussian, field-aligned; 2-keV Gaussian, isotropic; and 700-eV Gaussian, field-aligned) are used in this chapter to examine the time-dependence of the emission rates and brightnesses of  $N_2(2PG)$  3371 Å and  $N_2^+(1NG)$  4278 Å. All cases were calculated for an incident electron flux of  $1 \text{ mW m}^{-2}$ . Since the transport equation is not calculated

with the time dependence of scattering or traveling secondary electrons, the time for the 4278 Å emission rate to reach steady state and to decay will be underestimated and its height integrated value will also be underestimated, as discussed in chapter 3.

Figures 4.2, 4.3, and 4.4 show the  $N_2^+(1NG)$  4278 Å and the  $N_2(2PG)$  3371 Å emission rate profiles and column integrated emission rates (brightness) for the three electron differential fluxes (Gaussian, field-aligned; Maxwellian, field-aligned; Gaussian, isotropic) with mean energies of 2 keV. For the Maxwellian spectra, this implies a characteristic energy of 1 keV. In each of these figures, the shape of the  $N_2^+(1NG)$  brightness in time is similar to the shape of the  $N_2(2PG)$  brightness in time. However, the  $N_2(2PG)$  brightness takes longer to reach peak brightness. This is expected since it was shown in Chapter 3 that the low-energy secondary electrons take longer to reach steady state (represented by the  $N_2(2PG)$  emission) than the precipitating electrons (represented by the  $N_2^+(1NG)$  emission).

The result of the 1-keV Maxwellian, field-aligned electrons and the high energy secondaries colliding with the atmosphere as shown in emission rates of Figure 4.3, is quite different from the emission rates from the 2-keV Gaussian, field-aligned electrons, shown in Figure 4.2. Since the Maxwellian intensity contains a small number of electrons at very high energies, the propagation of the beam does not produce significant optical emissions until the high-energy electrons have already reached the atmosphere at  $\sim 110$  km. The slower electrons trail the high-energy electrons and so the emission region expands upward in altitude with increasing time after starting at the bottom of the aurora. This optical effect is known as “flaming” [Vallance Jones, 1974; Chamberlain, 1995]. The brightness of the 2-keV Gaussian, isotropic beam also produces the flaming effect in the optical emission. Whereas the Maxwellian beam in Figure 4.3 has parallel velocity dispersion due to the different energy electrons, the isotropic beam in Figure 4.4 has parallel velocity dispersion due to the different pitch-angles (pitch-angle dispersion). The 2-keV electrons in the pitch-angle parallel to the magnetic field will reach the lower ionosphere first and then the electrons in the other pitch-angles will reach the ionosphere higher in altitude and will produce optical emissions this region. The higher the source region for these types of spectra (isotropic and Maxwellian), the larger the dispersion will be and the longer the emission rates will take to reach steady state, as studied in Chapter 5.



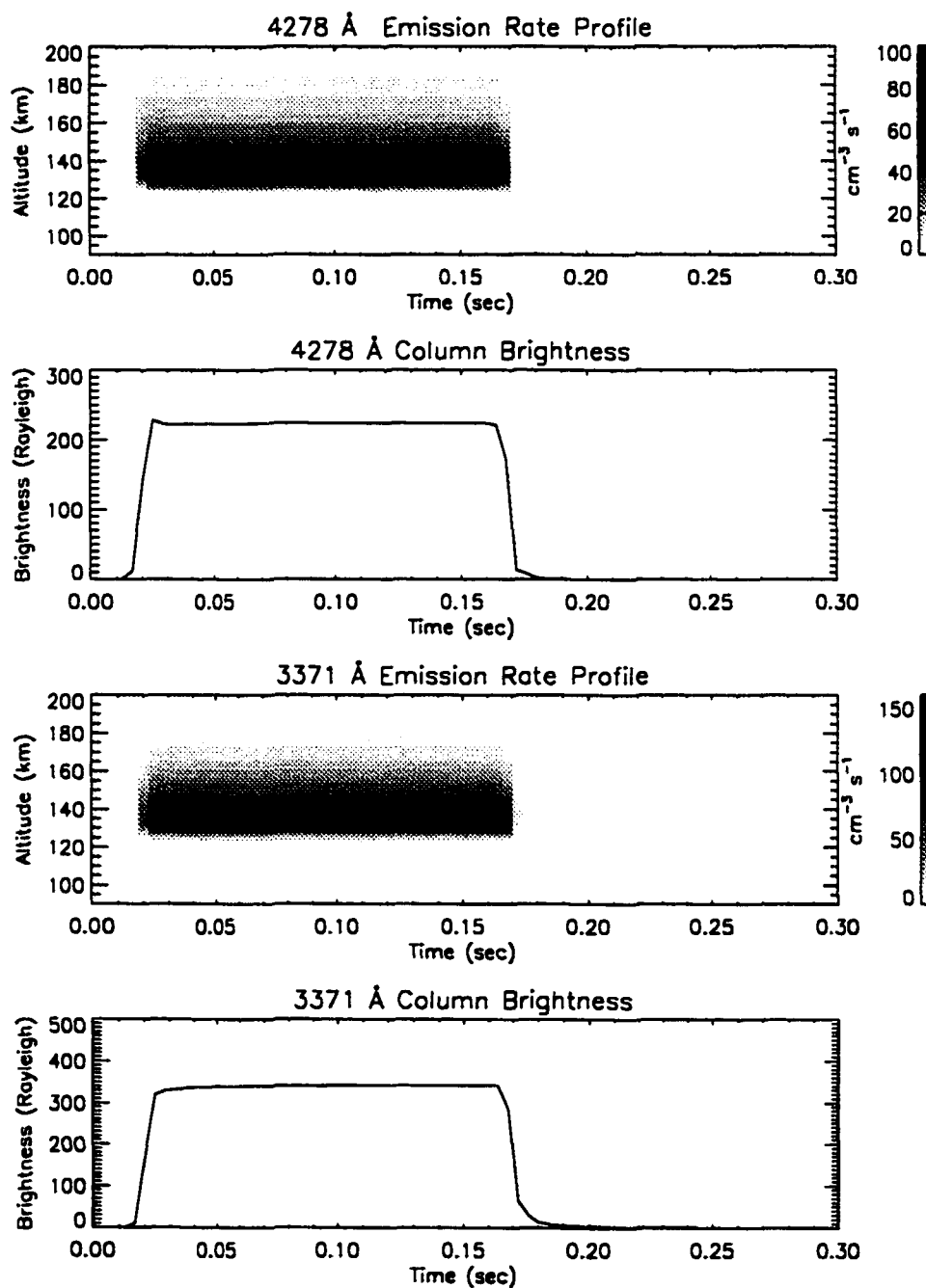


Figure 4.2. 4278 Å and 3371 Å emission rates from a 2-keV Gaussian, field-aligned beam.

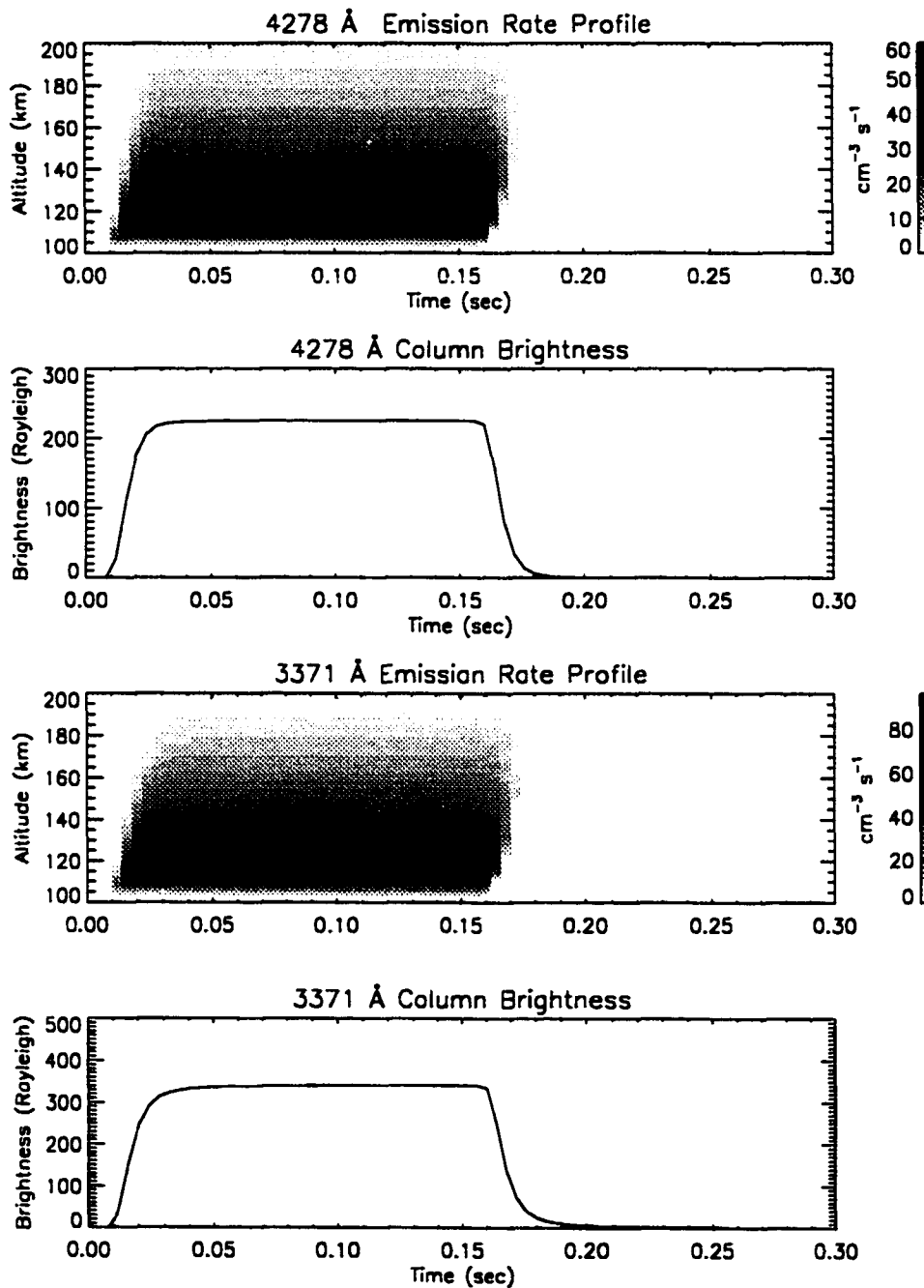


Figure 4.3. 4278 Å and 3371 Å emission rates from 1-keV Maxwellian, field-aligned beam.

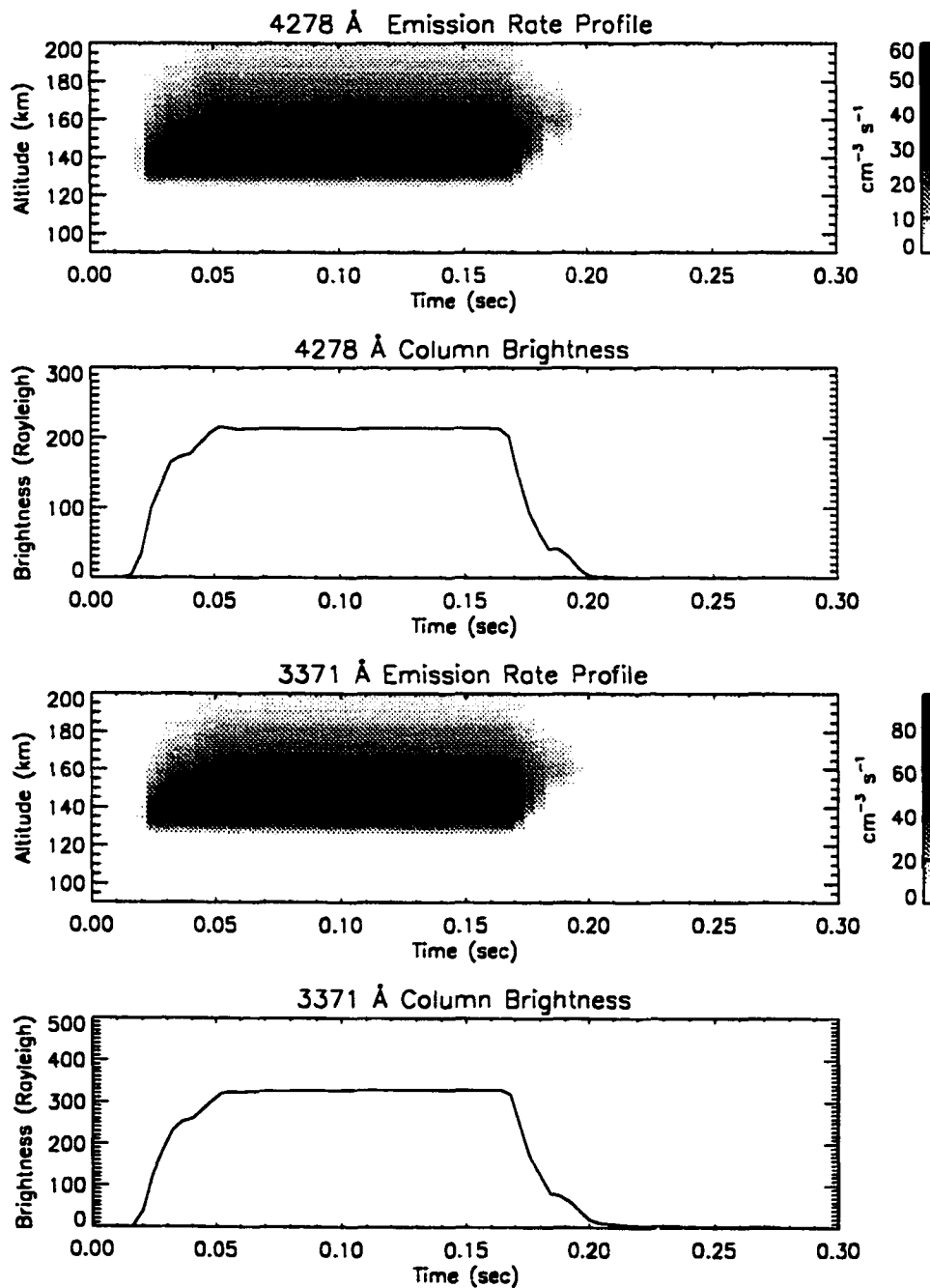


Figure 4.4. 4278 Å and 3371 Å emission rates from 2-keV Gaussian, isotropic beam.

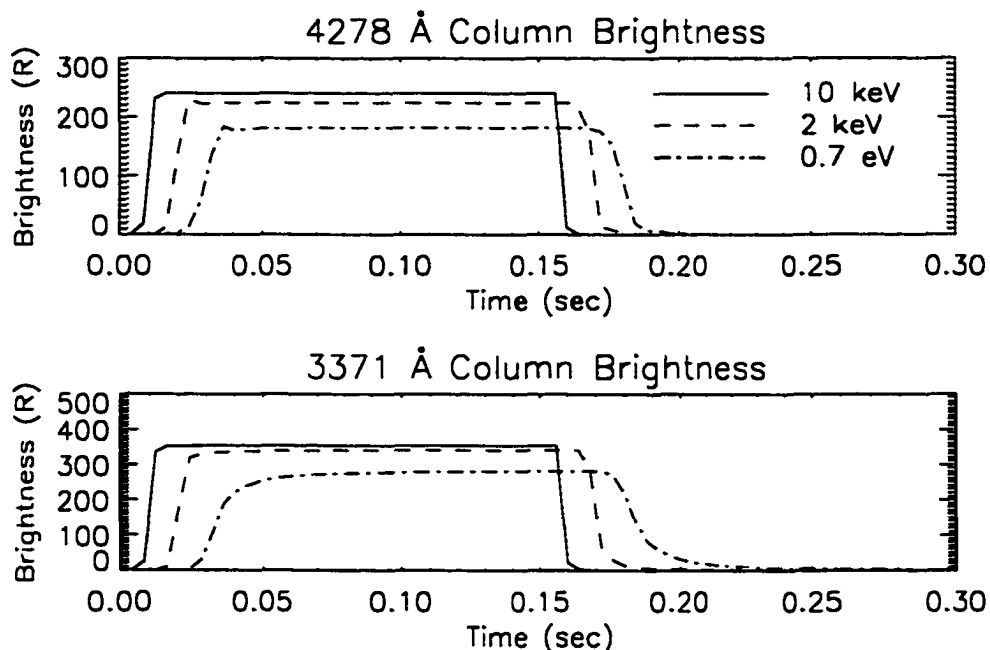


Figure 4.5. 4278Å and 3371Å column emission rates for three beams. The electron beams are monoenergetic and field-aligned with energies of 700 eV, 2 keV and 10 keV.

Since the 4278 Å emission rate is primarily dependent on the degraded primary electrons, the ionization rate will decay according to how the last of the electrons in the precipitating pulse transport through the upper atmosphere. For the monoenergetic beams, this means little time-dependent decay as seen in Figure 4.2, but for the Maxwellian and isotropic spectra, the slower parallel velocity electrons will trail the faster electrons, as can be seen in Figures 4.3, and 4.4. The scattering of these electrons and their propagation back to the acceleration region will affect the tail of the ionization rate decay. The same velocity dispersion effects can be seen in the  $N_2(2PG)$  3371 Å emission rates since the precipitating electrons that ionize  $N_2$  create the secondaries that then excite  $N_2$  to produce these emission rates.

By comparing the brightnesses of the monoenergetic, field-aligned beams of different energies, it is possible to examine the effect of the electrons with different energies on the time dependence of the emissions. Figure 4.5 shows the  $N_2^+(1NG)$  and  $N_2(2PG)$  surface brightness for 700-eV, 2-keV and 10-keV monoenergetic, field-aligned electron pulses. Since

each pulse starts from 630 km, this altitude can be considered the source region. The 10-keV electrons are the first to reach the altitude at which they lose the bulk of their energy. This velocity dispersion can be seen from the time lag in the growth and decay of the brightness in time for each different energy electron pulse. If the source of the electrons is higher in altitude, this lag will be greater for the different energies. If the source of the electrons is at or below the altitude at which the 700-eV electrons lose the bulk of their energy, the 700-eV brightness will begin to grow and decay before the 2-keV and 10-keV emission rates. The shape of the brightness curve will remain the same independent of the altitude from which the beam starts since these beams are monoenergetic and field-aligned and therefore without dispersion. The shape, then, reflects the way in which the electrons lose their energy to the atmosphere. In Figure 4.5, the shapes of the  $N_2^+(1NG)$  brightness curves are quite similar, but for the expected time delays and differing maximum amplitudes. The shape of the  $N_2(2PG)$  brightness curves are different for the three different energy beams. This reflects the fact that the secondaries take longer to reach steady state at higher altitudes where the 2-keV electrons lose the bulk of their energy and even longer at altitudes, where the 700-eV electrons deposit most of their energy.

## 4.2 Emission Ratios

It is apparent from Figures 4.2-4.5, that the ratio of the  $N_2(2PG)$  3371 Å emission to the  $N_2^+(1NG)$  4278 Å emission should vary in time differently for different incident electron spectra. This 3371Å/4278Å ratio is displayed in Figure 4.6 for the first 60 ms of the five different electron spectra propagating into the upper atmosphere. The electron spectra are the same as those studied above. Even though the  $N_2(2PG)$  brightness in Figure 4.5 is still changing after 60 ms for the 700-eV beam, it only increases by 10% by the time it does stop changing at 150 ms. Figure 4.6 is organized with the fastest growth time at the top and the slowest growth time at the bottom. The time it takes this ratio to increase from 15% of its value to 85% of its value is 2 ms, 5 ms and 30 ms, respectively, for the 10-keV, 2-keV and 700-eV monoenergetic, field-aligned electron spectra. For the 1-keV Maxwellian, field-aligned electron beam it takes 10 ms and for 2-keV monoenergetic, isotropic beam, it takes 15 ms.

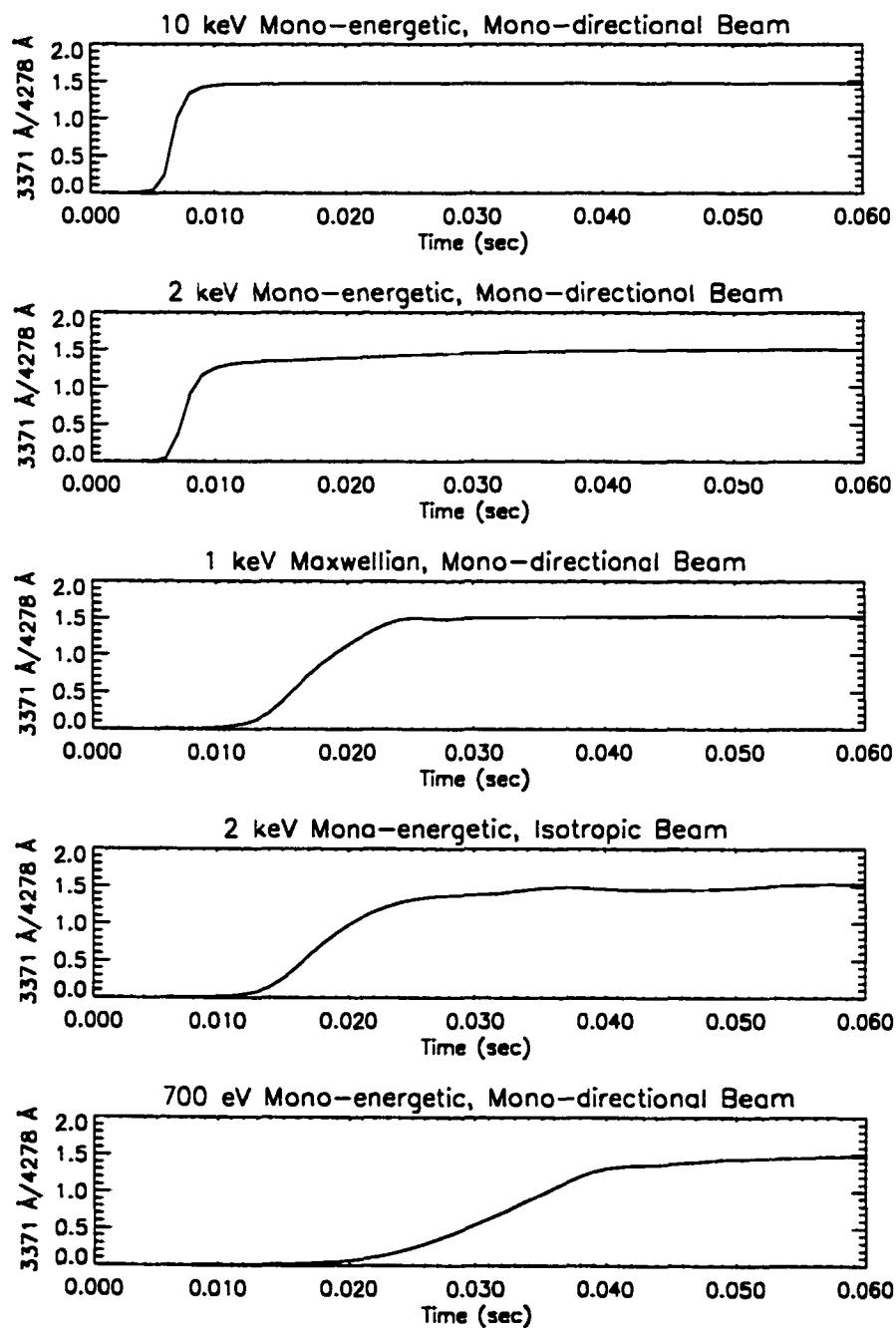
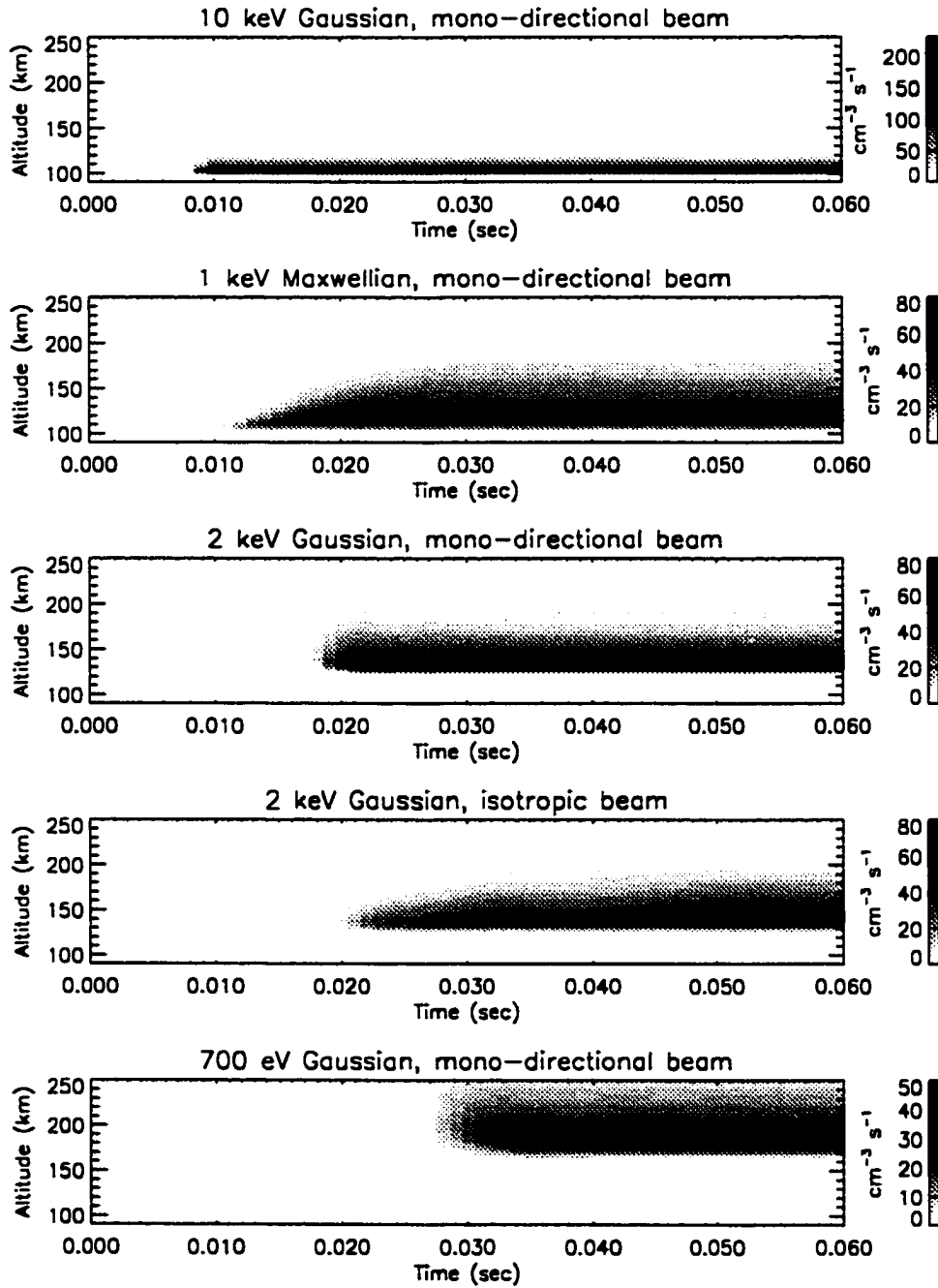


Figure 4.6.  $N_2(2PG)/N_2^+(1NG)$  time-dependent ratio.

In the case of steady-state electron differential number fluxes, the  $N_2(2PG)$  to  $N_2^+(1NG)$  ratio has been shown to be constant independent of the energy of the precipitating electrons with a value of  $0.93 \pm 0.07$  for the  $3371\text{\AA}/4278\text{\AA}$  ratio [Strickland *et al.*, 1989; Richards and Torr, 1990; Gattinger *et al.*, 1991]. This should also be true in this study when the electrons  $< 14$  eV have reached steady state. It is seen here clearly that all five of the ratios approach the same value of 1.5 for this ratio. This error is mostly in the  $4278\text{\AA}$  column brightness since the lack of scattering in the calculation decreases this value by  $\sim 40\%$ , as discussed in Chapter 3 regarding the integrated ionization rates. The 2-keV monoenergetic, isotropic beam and 700-eV monoenergetic, field-aligned beam just reach the steady state value in the 60 ms shown. Because this ratio should be constant for steady-state electron differential fluxes in the ionosphere, variations in the ratio should be attributable to time dependence in the auroral electron differential fluxes. Gattinger *et al.* [1991] found slight variations in the  $N_2(2PG)$  to  $N_2^+(1NG)$  ratio for lower energy electrons. Since the time dependence in the  $N_2(2PG)$  to  $N_2^+(1NG)$  ratio has been shown to be more significant (i.e., on longer time scales) for lower energy precipitating electrons, the variations Gattinger *et al.* [1991] measured could be due to this time dependence.

The results in this chapter indicate that most electron spectra should lead to some type of flaming aurora if observed at sufficiently high time resolution. It is possible to optically observe low-energy precipitating electrons propagating down into the atmosphere and emitting light as they collide with the upper atmosphere. Observing high-energy electrons in the same manner is very unlikely due to the low probability of collisions at higher altitudes. To better demonstrate this, Figure 4.7 shows 1 ms resolution  $4278\text{\AA}$  emission rate profiles for the first 60 ms from each of the five different electron spectra transport calculations. There is no obvious altitude spread in the emission rates of monoenergetic, field-aligned spectra with higher energies, as seen in the 2-keV and 10-keV electron spectra in Figure 4.7.



**Figure 4.7. 4278 Å emission for five different spectra.**



Also seen in Figure 4.7, the parallel velocity dispersion in the Maxwellian and isotropic spectra produce flaming emissions: the emissions begin at a lower altitude and 'grow' upward in altitude as time increases. One could argue that this flaming is the optical observation of the pulse entering the ionosphere when the observation is made using prompt emissions. White-light observations are dominated by the OI (5577 Å) line with a radiative lifetime of 0.7 s, which may wash out some of the flaming effects. [Vallance Jones, 1974]. Flaming has been studied by *Sourfield and Parsons* [1969] and *Cresswell* [1969] who concluded that the electrons creating pulsating aurora come from altitudes as far away as the equatorial plane. If a Maxwellian or isotropic pulse of electrons comes from 60,000 km instead of 630 km, as in the simulations for the emission rates shown in Figure 4.7, longer time scales and thinner emission rate profiles will result due to the larger effect of velocity dispersion.

The time-dependent electron transport model shows that sudden pulses of monoenergetic or Maxwellian electrons penetrating into the ionosphere result in a sudden activation of the aurora at a fixed altitude or give the appearance of an upward moving emission region (flaming). From the understanding gained from this modeling it is instructive to speculate which conditions would give the appearance of a downward moving pulse of light from energetic electrons (those that travel farther in altitude). Since such an observation could not be explained with the types of spectra simulated in this thesis, there are at least three explanations for such an observation. First, the observing geometry could be such that the motion of the emission is moving away from the observer, such as a drifting arc, and not down along the field line. Second, the acceleration region could be changing slowly such that the acceleration of electrons is increasing in time. The change in the acceleration would have to be sufficiently slow that the fast electrons do not reach the ionosphere before the slower electrons. And third, the source of the acceleration could be in the lower ionosphere, below 1,000 km. For example, imagine a parallel electric field in the upward direction is turned on from ~100 km-1,000 km. Then the electrons near ~300 km would be accelerated the least and would collide immediately near ~200 km, producing emissions. The electrons closer to 1,000 km would drop through a greater potential and pick up more energy, but it would take them longer to reach the lower altitudes. Thus the emissions would appear at the higher altitudes first from the lower energy electrons and then at lower altitude from

the higher energy electrons. If these three situations can be distinguished, looking for such optical observations could help to study the parallel electric fields in the ionosphere and in the acceleration region.

This chapter has been concerned with the study of optical emissions varying on the order of milliseconds to hundreds of milliseconds due to the time dependence in the incident electron differential number flux. Such a study shows that flaring in prompt emissions should be common unless monoenergetic, field-aligned electrons are producing the emissions observed. Ratios of  $N_2(2PG)$  to  $N_2^+(1NG)$  should be constant for electrons having reached steady state in phase space and should vary for a time-varying incident electron fluxes. Measurable variations in the  $3371\text{\AA}/4278\text{\AA}$  emission ratios provide quantitative information regarding the shape of the incident electron spectrum. Time variations on the order of milliseconds can be observed in any measured emission ratios whose parent states are excited by electron impact with significantly different excitation cross sections. The time-dependent transport of electrons places restrictions on theories which could explain observations of emissions that propagate down to altitudes less than  $\sim 120$  km. Looking for such optical signatures may help to learn about other physics in the ionosphere.

## Chapter 5

# Field-Aligned Bursts of Electrons in Flickering Aurora

When viewed in the zenith, flickering aurora is an auroral form for which localized spots along a discrete arc are modulated in brightness at frequencies from 2-20 Hz [Beach *et al.*, 1968; Berkey *et al.*, 1980; McFadden *et al.*, 1987] to over 100 Hz [McHarg *et al.*, 1998]. These spots are typically 1-5 km in diameter and flicker coherently for seconds. When viewed out of the magnetic zenith, the flickering elements are seen as vibrating columns of optical intensity [Kunitake and Oguti, 1984]. Flickering is observed in bright, discrete aurora such as in auroral surges [Berkey *et al.*, 1980].

*In situ* periodic fluctuations in the electron differential number flux were recorded as early as 1966 [Evans, 1967]. These measurements showed periodicities around 10 Hz in 1-120 keV electrons at altitudes around 90-200 km, with the fluctuations strongest for electrons >60 keV. Similar results were deduced from measurements of charged particles with energies >85 keV at similar altitudes [Arnoldy, 1970; Spiger and Anderson, 1985]. Since then, instruments on rockets and satellites have recorded periodic fluctuations from a few hertz to near 100 Hz with lower energy electron detectors ( $E < 20$  keV) and at altitudes greater than 250 km [Lin and Hoffman, 1979b; Arnoldy *et al.*, 1985; McFadden *et al.*, 1987]. From these studies, the fluctuations are known to be strongly field aligned and have thus been given the name field-aligned bursts (FABs). Pitch-angle dispersion has been measured more recently [Temerin *et al.*, 1993; Arnoldy *et al.*, 1999], implying that the modulation is not completely

in the field-aligned component. Source altitudes for modulation of the electron differential fluxes have been calculated from velocity dispersion [Evans, 1967; McFadden et al., 1987; Arnoldy et al., 1999], from pitch angle dispersion [Temerin et al., 1993; Arnoldy et al., 1999], from the time lag between detection of precipitating electrons and the associated Alfvén wave [Lund et al., 1995], and by determining the altitude at which the oxygen or hydrogen cyclotron frequency matches the measured electron differential flux modulation frequency, which assumes that flickering is caused by electromagnetic ion cyclotron waves [Temerin et al., 1986; Lund et al., 1995]. These calculations have provided many different source altitudes ranging from 1300 [Evans, 1967] to 8000 km [McFadden et al., 1987]. A few of the papers discussing measurements of electron fluctuations also mention simultaneous optical measurements [Spiger and Anderson, 1985; McFadden et al., 1987; Lund et al., 1995; Arnoldy et al., 1999], and all of these optical measurements recorded flickering in the same discrete arcs as the electron modulations were detected.

In this chapter, the time-dependent transport equation is solved to study the modification of field-aligned bursts of electrons (FABs) by the atmosphere. Optical emissions of such FABs are shown for different source regions and different flicker frequencies. The way that the  $N_2(2PG)$  3371 Å to the  $N_2^+(1NG)$  4278 Å brightness ratio changes in time represents the time variation in the electron differential flux at different energies. In Section 5.2, the results of this study of flickering FABs are discussed in the context of past research.

## 5.1 Field-Aligned Bursts of Electrons

Arnoldy et al. [1999] have shown with the PHAZE II rocket data that field-aligned bursts (FABs) of electrons in flickering aurora often show a 100% on-off modulation of the down-going flux. These FABs have electron-differential fluxes that can extend from the peak electron differential number flux energy down to energies  $<50$  eV [Spiger and Anderson, 1985; McFadden et al., 1987]. The pitch-angle dispersion shown by Temerin et al. [1993] and Arnoldy et al. [1999] is seen in the high-energy electrons around the peak inverted V energy and not in the lower energy FABs. These pitch-angle dispersed electrons are assumed to come from the hot plasma sheet unlike the field-aligned bursts of electrons [Temerin et al., 1993; Arnoldy et al., 1999]. The electron differential number flux modulations measured

above  $\sim 200$  km are believed to be modulated below the potential drop in the acceleration region by electromagnetic ion cyclotron waves [Temerin *et al.*, 1986, 1993], or by the acceleration region parallel electric field turning on and off [Arnoldy *et al.*, 1999]. The FABs have also been measured in the absence of high-energy electrons [Lin and Hoffman, 1979b; Johnstone and Winningham, 1982]. Even though the plasma sheet electron modulations will be important to the optical signatures in the lower ionosphere, in order to investigate their importance to optical emissions only the lower energy FABs from an energy of 3 keV down to 10 eV are modeled in this study.

The FABs are modeled using a total flux of  $1 \text{ mW m}^{-2}$  and the differential number flux is assumed to be a flat distribution in energy from 10 eV to 3 keV and turned completely on and off at a source altitude of  $\sim 3800$  km (4000 km along the magnetic field line). Figure 5.1 shows this differential flux as a function of energy and time at 4000 km, where  $t = 0$  corresponds to the time the highest-energy electrons (3 keV) have reached the simulation box (630 km). Since the FABs are field-aligned, the calculation of the time varying flux at the top boundary is simply a matter of calculating the force-free motion along a magnetic field line from the source region (4000 km) to the simulation box top boundary (630 km) using  $v = \Delta s / \Delta t$  where  $v$  is the velocity of the electron,  $\Delta s$  is the length along the magnetic field from the source region to the top of the simulation box (3,370 km), and  $\Delta t$  is the length of time it takes for the electron to move this distance with velocity  $v$ . The calculation performed in the model uses this simple relation to determine at which time,  $t_f$ , electrons with a particular velocity,  $v$ , appear at the upper boundary and when they disappear due to being turned off at the source region. Beginning with  $\Delta t = \Delta s / v$ , gives  $t_f = \Delta s / v + t_0$  where  $t_0$  is defined as the time it took for the fastest electrons to reach 630 km,  $t_0 = \Delta s / v_{\text{max}}$ . Two typically observed flux modulation frequencies are used, as mentioned in the above references: 5 and 100 Hz. Because a 100 Hz frequency is so fast, in order to resolve each dispersed electron pulse on the simulation grid it is necessary to have a more refined energy grid than used in Chapters 3 and 4. The energy grid used in this study has a maximum  $dE$  of 35 eV. This study is not concerned with the mechanisms which create flickering but the observable optical effect of flickering FABs in the ionosphere.

The solution to the transport equation for flickering field aligned electron bursts is the electron spherical differential flux as a function of time, energy, and altitude. This electron

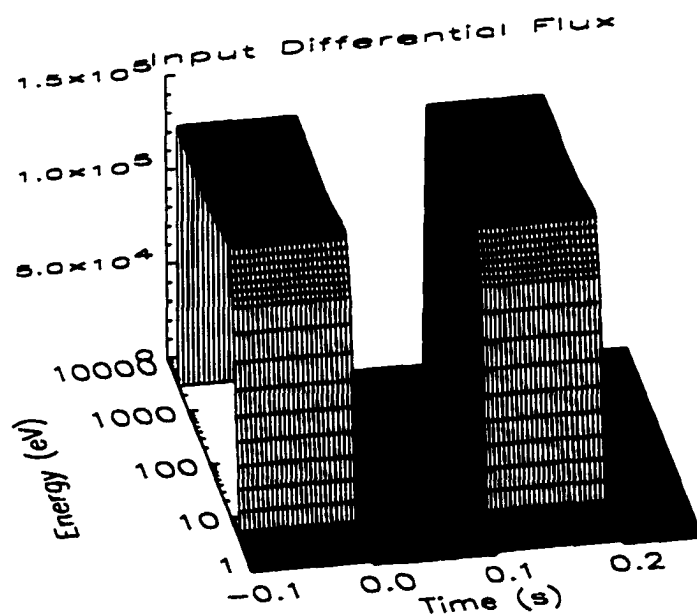


**Figure 5.1. Modulation of the initial differential flux. The plot shows this modulation at the source region (4000 km along the magnetic field). Note that  $t=0$  is the time the 3 keV electrons reach the 630 km upper boundary of the simulation box.**

flux for the 5 Hz case is shown in Figure 5.2 at four times as a function of energy and altitude. At  $t = 40$  ms, the electrons with energy greater than  $\sim 2$  keV have reached the upper atmosphere, collided, lost the bulk of their energy, and created secondaries from ionizing collisions. Electrons with energies between 600 eV and 2.5 keV have entered the upper atmosphere by  $t = 120$  ms. Since the pulse was turned off after 0.1 s, electrons with energies greater than 2 keV are no longer entering the atmosphere, so the altitude of peak secondary differential flux has increased by  $\sim 5$  km. At higher altitudes, the secondary differential flux continues to increase in part due to the slower electrons and in part due to difference in production *versus* loss rates at different energies, as was seen in Chapter 3. At 200 ms, the much slower electrons are still entering the upper atmosphere and the altitude of peak secondary differential flux has increased by 50 km since  $t = 40$  ms. The electrons with energies  $> 1$  keV have lost all their energy below 140 km, and only the secondaries of these electrons remain at energies  $< 10$  eV at these altitudes. At  $t = 280$  ms, the last of the low-energy electrons from the first pulse are still arriving and depositing their energy at altitudes above 200 km. The high-energy electrons of the second pulse have reached the lower altitudes (120-160 km) and the cycle begins anew.

The electron differential flux as a function of energy and altitude shows the consequence of the transport of the electrons into the upper atmosphere and the manner of their energy loss. It is also possible to look at the results as a function of time and energy from the perspective of a rocket flying through such FABs at a particular altitude. Shown in Figures 5.3 and 5.4 are the spherical electron differential fluxes created by a 5 Hz modulated FAB as a function of time at 502 km and 153 km, respectively. In order to demonstrate what this might look like to an electron detector flying at the two altitudes at an instant in time, a slice of each spherical differential flux at 348 ms has been taken, converted to distribution function and plotted below the time-dependent spectra in Figures 5.3 and 5.4.

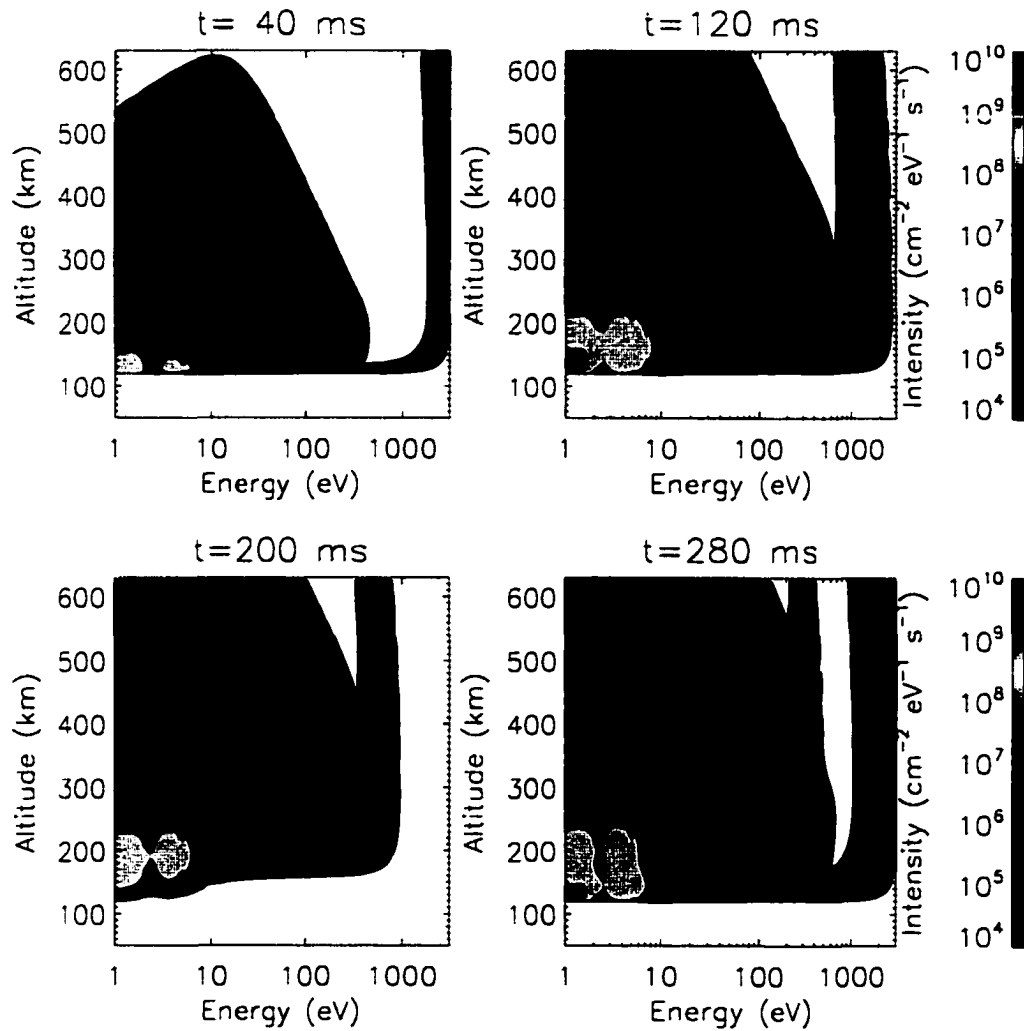
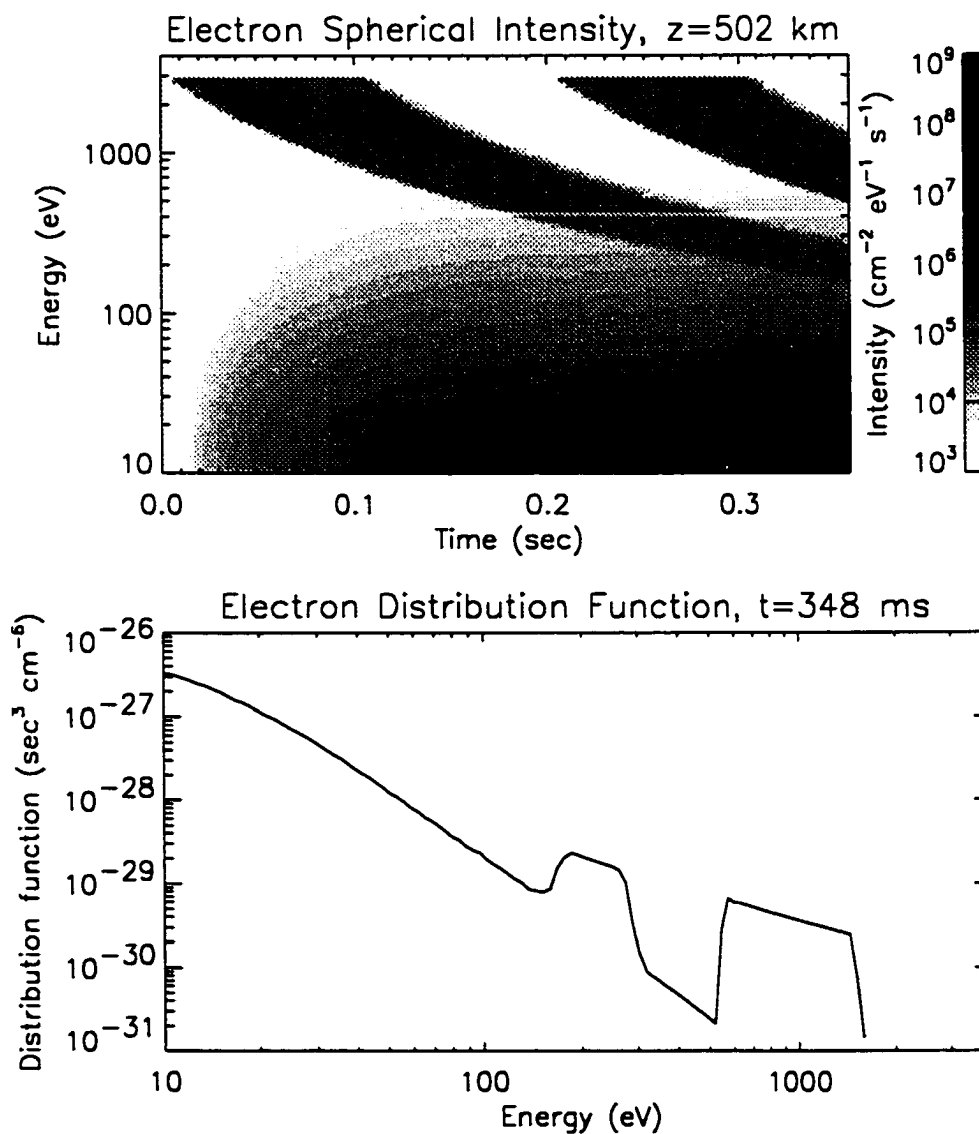


Figure 5.2. The differential flux for 5-Hz-modulated FABS. The electrons come from a source altitude of 4000 km. Each plot show the differential flux at a different time, where  $t=0$  corresponds to the arrival of the 3-keV electrons at 630 km altitude.





**Figure 5.3.** The differential electron flux at 502 km. (top) The field-aligned flux as a function of energy and time at 502 km altitude. (bottom) A cut at  $t=0.348$  s of the Figure 5.3(top) which has then been converted to distribution function from flux.

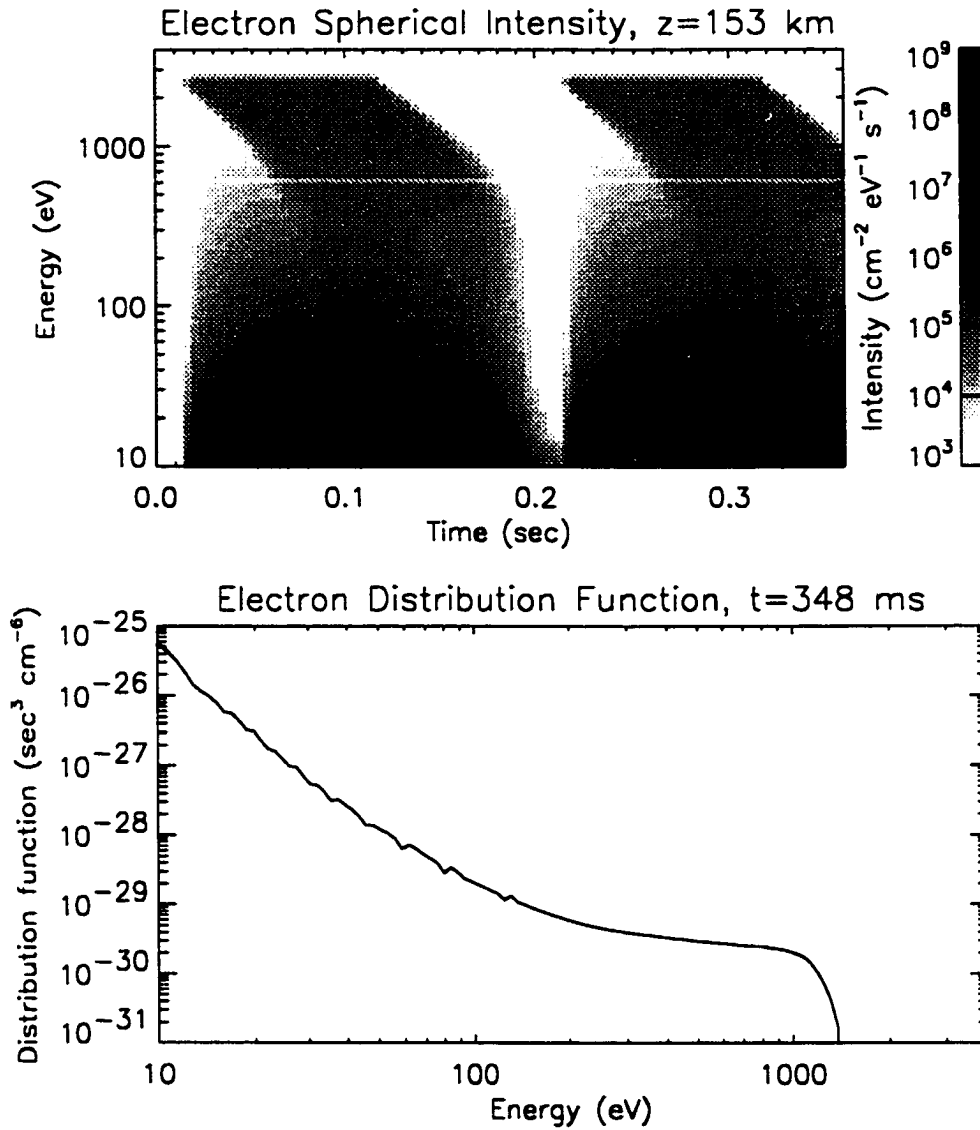


Figure 5.4. The differential electron flux at 153 km.

The spherical differential fluxes of Figure 5.3 clearly show the dispersion of the primary energy spectrum as these two beams reach 502 km. This dispersion is very similar to that seen in the fluxes of *Arnoldy et al.* [1999], especially in their Figure 2 and Plate 4. *Arnoldy et al.* [1999] show the field-aligned electrons, only so that the low-energy secondary electrons shown in Figure 5.3 are not seen in their figures. At this altitude, the atmospheric density is low enough that the probability of collisions is small, and the electrons which are created from ionizing collisions should be transported away. Only the backscattered low-energy electrons would be measured in this region.

The bumps shown in the distribution function of Figure 5.3 are due to the two FABs: one which has recently been turned on and for which only the high-energy electrons have arrived at the altitude of the rocket and a second one which has been turned off for a while and only the low-energy electrons are still propagating into the ionosphere. The plateau represents the original flat spectrum which was assumed as the upper-boundary condition. With higher frequency modulation of the down-going flux, there will be more bumps, and they will have narrower energy spans. If the time integration of the instruments measuring the electron differential flux is too long to resolve the two FABs in time, the flux from the two FABs at different energies will overlap, resulting in a distribution function which looks fairly constant over a broad range of energies.

Since the instruments used by *Arnoldy et al.* [1999] have sufficient energy and time resolution to see the dispersion in the FABs, when these PHAZE II electron data are plotted as distribution functions, multiple bumps are seen [*Semeter et al.*, 1999]. *McFadden et al.* [1990] also see similar bumps in field-aligned distribution functions measured by electron detectors on a sounding rocket during the Berkeley Ionospheric Dual Altitude Rocket Campaign. They explain these plateaus as due to waves created by the semi-unstable distribution function. From the results in Figure 5.3, it seems more likely that the plateaus seen in these rocket electron distributions are simply due to measurements of multiple FABs at a particular time and space in the aurora. If this interpretation is correct, it may be possible to deduce from rocket or satellite measurements not only the source altitude but also the source distribution function. Knowledge of the source distribution function should help to determine the process for generating modulated FABs detected during flickering aurora.

How collisions affect the electrons at 153 km can be seen by comparing Figure 5.4 with Figure 5.3. As time passes the low-energy electrons of the pulse eventually reach this altitude, where they are slowed down and stopped much faster than at 502 km (where they continue to move through the region at their original velocity). Figure 5.4 also shows how the distribution function, if sampled at a time when the pulse is still on, will look flat at high energies because of the large energy loss to the ionosphere. The effect of this energy loss is greater in denser atmosphere and at low energies, where the electron-neutral collision cross sections are largest. The altitude above which neutral-electron collisions are negligible will also change with the solar cycle since the atmosphere expands during the solar maximum period and increases in density at higher altitudes during these years. This can also be true of very active aurora, which heats the local thermosphere.

### 5.1.1 Emission Rates

As mentioned in Chapter 4, *McHarg et al.* [1998] and *Sakanoi and Fukunishi* [1999] have studied optical emissions of flickering aurora at time scales on the order of milliseconds and less. *McHarg et al.* [1998] used a 16-channel fast photometer with a time resolution of 10-25  $\mu$ s. They studied the frequency response of white-light flickering at an elevation angle from 10-30°. Not only did they observe 10-Hz flickering as recorded previously [*Beach et al.*, 1968; *Berkey et al.*, 1980; *McFadden et al.*, 1987], but they also observed flickering up to 180 Hz and broadband frequency spectra. *Sakanoi and Fukunishi* [1999] used filters on their MFP, as discussed in Chapter 4, to examine flickering at 10 ms and 1 ms resolution and at an elevation of 63°. Eight-Hertz flickering was found in their 10 ms, 4278 Å data.

The prompt  $N_2^+(1NG)$  4278 Å and  $N_2(2PG)$  3371 Å emission rates and brightnesses are modeled for 5-Hz and 100-Hz pulsed electron field-aligned bursts coming from source distances of 4000 km and 630 km. These emissions are calculated in the same manner as done in Chapter 4. Figures 5.5 and 5.6 show the 4278 Å emission rate profiles and column brightnesses for these four different cases (5 Hz from 4000 km; 5 Hz from 630 km; 100 Hz from 4000 km; and 100 Hz from 630 km). As with the single pulse in Chapter 4, the emission rate profiles of the 5 Hz flickering FABs in Figure 5.5 demonstrates flaming. This effect is more pronounced for the case in which the electrons come from 4000 km since the flaming is due to the velocity dispersion of the electrons. The flaming smoothes out the

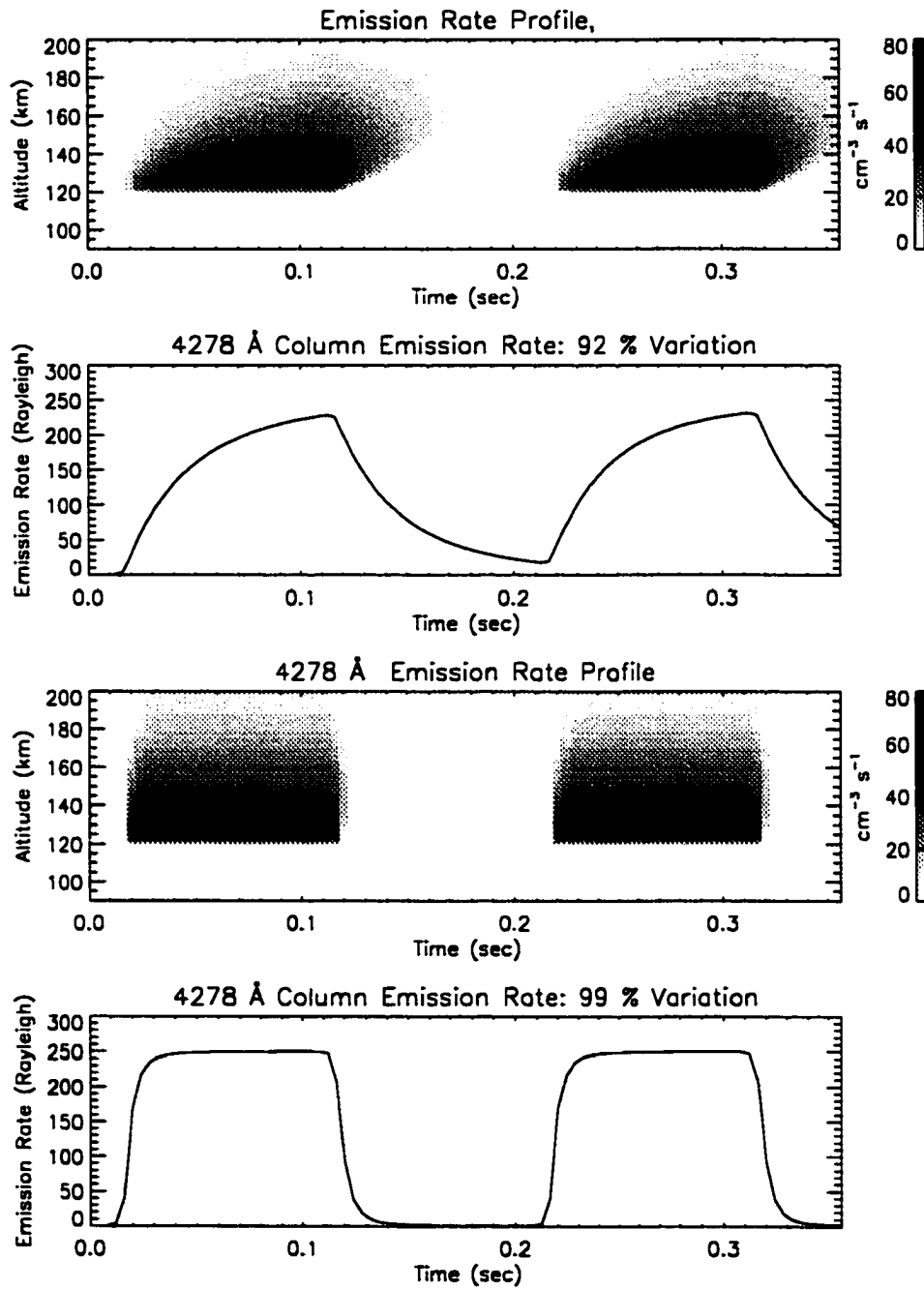


Figure 5.5. Optical emissions from FABs modulated at 5 Hz from 4000 km. (top) The altitude dependent 4278 Å emission rates over time due to the FABs. (bottom) The column integrated emission rates.

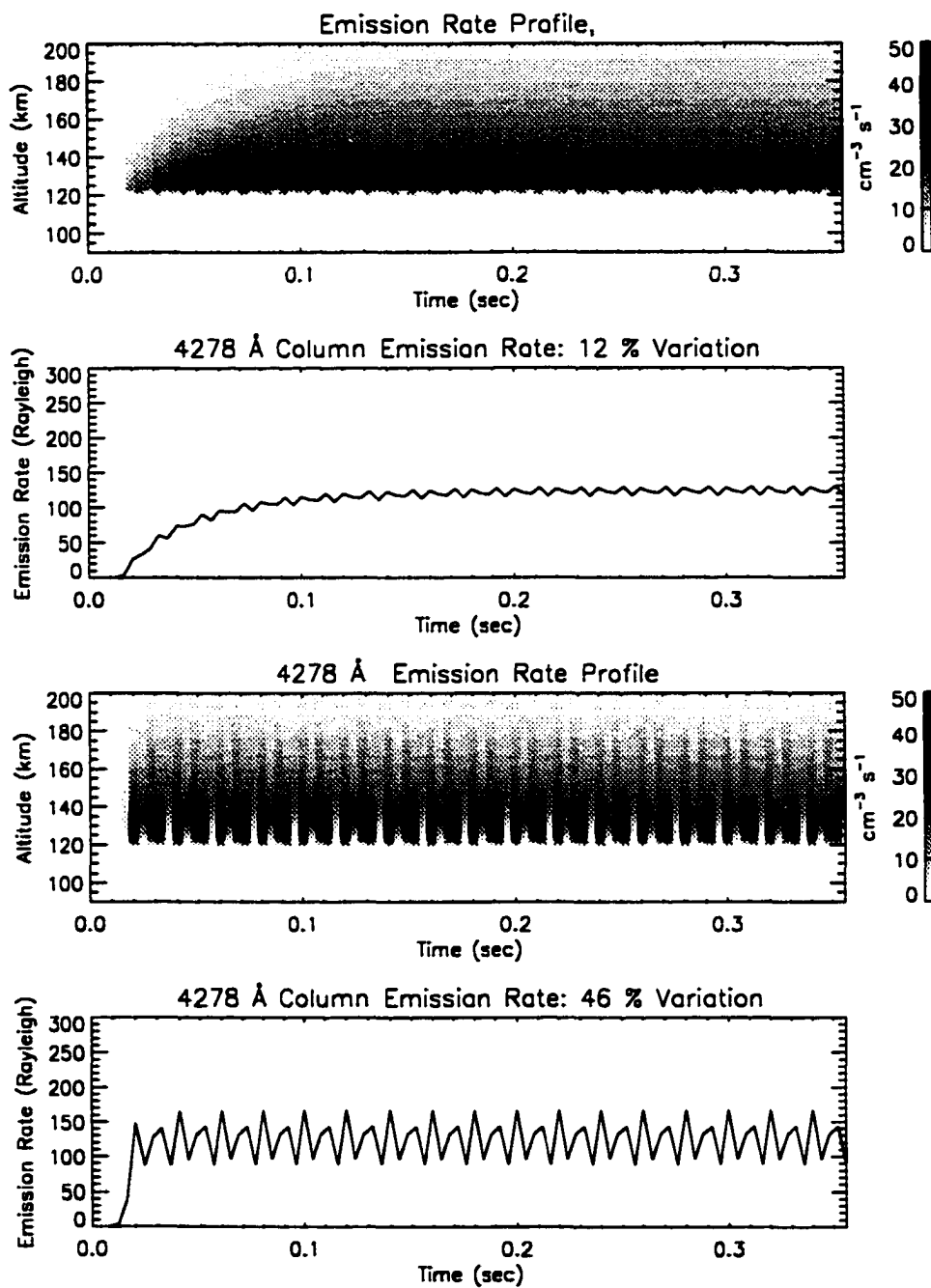


Figure 5.6. Optical emissions from FABs modulated at 100 Hz from 4000 km.

brightness variations as viewed in the magnetic zenith. The percent difference between the peak and valley of the brightness for the electrons coming from 630 km is 99%, while the percent variation is 92% for the electrons coming from 4000 km.

The 100-Hz modulated electron FABs have smaller variations in their peak-to-valley brightness emissions, as seen in Figure 5.6. The 100-Hz modulated electron differential flux from 630 km produces a 46% variation in 4278 Å brightness, while the modulated electrons from 4000 km produce a 12% difference. Even though the 4278 Å emission is prompt, this temporal variation in the electron differential flux in the ionosphere gives it the appearance of an emission from a long lived state.

Figures 5.5 and 5.6 are quite different in their column brightness. The maximum value of the  $N_2(2PG)$  brightness in flickering aurora is lower for the 5 Hz frequency case than the 100 Hz case, although the incident electron flux is the same as in the low-frequency case ( $1 \text{ mW m}^{-2}$ ). This is due to the time averaging that occurs from the dispersive transport of precipitating electrons. Averaging the brightness shown in Figures 5.5 and 5.6 over many on-off pulses yields the same brightness in both cases (125 Rayleighs) and is in agreement with the brightness of the steady-state model when driven with the time-averaged precipitation (i.e., with a constant energy flux of  $0.5 \text{ mW m}^{-2}$ ).

The shape and timing of the  $N_2^+(1NG)$  4278 Å and the  $N_2(2PG)$  3371 Å emission rate profiles and column brightnesses are very similar. The smoothing of the variation in the 3371 Å emission rate altitude profile and the surface brightness is greater than that of the 4278 Å emissions due to the slower growth and decay time of the very low-energy electrons. There is also a small delay in the growth and decay of the maximum brightness value in the 3371 Å emission. This difference is best seen in the ratio of  $N_2(2PG)$  3371 Å to  $N_2^+(1NG)$  4278 Å emission shown in Figure 5.7. As discussed in Chapter 4, if the value of this ratio is different from its steady-state value, then the electrons with energies  $\sim 14 \text{ eV}$  change in time differently than the electrons with energies  $\sim 100 \text{ eV}$ .

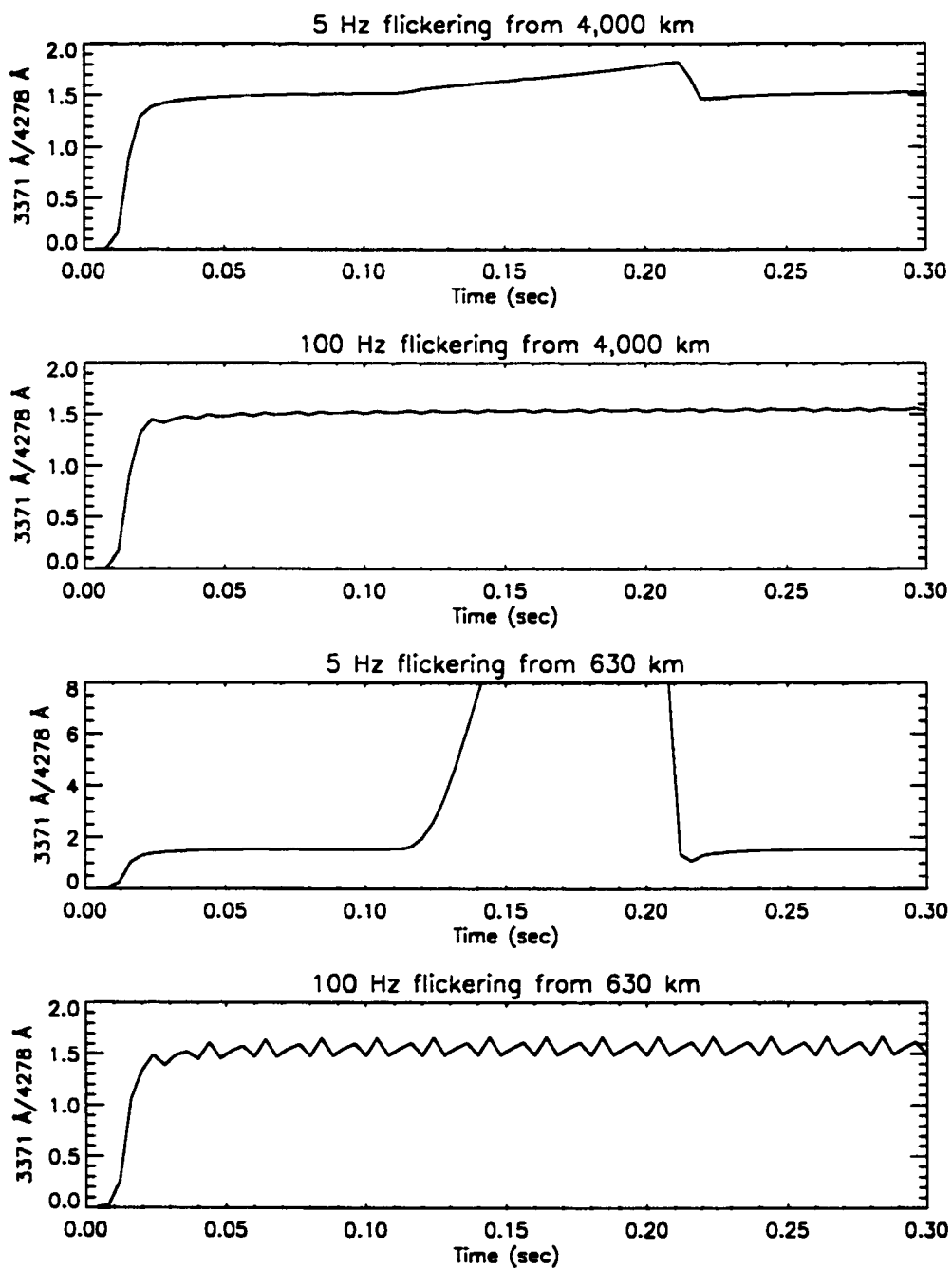


Figure 5.7.  $\text{N}_2(2\text{PG})$   $3371 \text{ \AA}$  to the  $\text{N}_2^+(1\text{NG})$   $4278 \text{ \AA}$  emission ratio.



As first shown in Chapter 4, the  $3371 \text{ \AA}/4278 \text{ \AA}$  ratio increases in the first  $\sim 20$  ms since the growth of the secondary electron differential flux near 14 eV lags the growth of the primary degraded electrons near 100 eV. The ratio of the 5-Hz, 4000-km case shown at the top of Figure 5.7 reaches the steady-state value of 1.5 and stays there until the pulse turns off. The lag in the electrons with energies  $\sim 14$  eV *versus* the electrons with energies  $\sim 100$  eV when the pulse is turned off is seen as a rise in the value of the  $3371 \text{ \AA}/4278 \text{ \AA}$  ratio. This rise is much larger in the case when the source region is closer to the lower ionosphere, as seen in the third plot as compared to the first plot in Figure 5.7. This is because the  $4278 \text{ \AA}$  brightness approaches zero as the last of the electrons propagate through the upper atmosphere and lose their energy. The  $3371 \text{ \AA}$  brightness does not approach zero as fast since the  $\sim 14$  eV electrons lose their energy more slowly to the atmosphere than the  $\sim 100$  eV electrons.

The  $3371 \text{ \AA}/4278 \text{ \AA}$  emission ratio produced by the 100 Hz FABs is also shown in Figure 5.7. The second plot from the top shows the emission ratio for the electrons coming from 4000 km and the bottom plot for the electrons from 630 km. The 100-Hz modulation changes in time on the same order that the growth and decay of the secondary electron differential flux near 14 eV lags the growth and decays of the primary degraded electrons near 100 eV. Not only does this change the ratio value, as for the 5-Hz case, but it also produces a phase shift of  $\sim 20^\circ$  between the peak emission ratio values and the peak  $4278 \text{ \AA}$  emission values. Although this phase difference will remain the same independent of the source altitude, the velocity dispersion will have a larger effect of smoothing the  $3371 \text{ \AA}/4278 \text{ \AA}$  ratio depending on the altitude. The second plot in Figure 5.7 shows that the velocity dispersion is more important than the lag in the low-energy response time for the 100 Hz FABs coming from 4000 km. This is seen in the very small oscillation about the steady-state value of 1.5 for this ratio. However, the  $4278 \text{ \AA}/3371 \text{ \AA}$  emission ratio for the electrons modulating at 100 Hz from 630 km show a larger oscillation in the ratio about the steady-state value. These four cases demonstrate that FABs modulated in time with frequencies close to 5 Hz and from a source region low in the ionosphere will produce the largest observable variations in the  $4278 \text{ \AA}/3371 \text{ \AA}$  emission ratio.

## 5.2 Discussion

The time-dependent transport model, in spite of the approximations discussed in Chapter 3 suggests some possible explanations of past conflicting data sets. *Evans* [1967] and *Spiger and Anderson* [1985] measured electrons less than a few keV as well as high-energy electrons greater than 10 keV. Strongest modulations in these data sets were observed in the higher-energy electrons, whereas in other data sets [*Lin and Hoffman*, 1979b; *Arnoldy et al.*, 1985; *McFadden et al.*, 1987], strong modulations were detected in the lower-energy electron differential number flux. The difference in these data sets is that the rockets flown by *Evans* [1967] and *Spiger and Anderson* [1985] were both below 190 km when flickering was observed, whereas the other rockets and satellites were above 200 km. As shown in Figure 5.4, as compared with Figure 5.3, electrons less than 2 keV lose energy below 150 km due to collisions with the ionosphere. It is feasible then that the lower-energy electrons measured by *Evans* [1967] and *Spiger and Anderson* [1985] were modified by the upper atmosphere and the modulations in these energies were not detected. The high-energy electrons have a smaller probability of colliding due to the energy dependent cross sections and thus would not be affected by the atmosphere at the altitudes through which the instruments flew.

It is also important to consider at what altitude the *in-situ* measurements of electron differential fluxes are made if the velocity dispersion of these fluxes is used to estimate the acceleration region altitude. As shown in Figure 5.4, the loss of energy to the atmosphere is large. If the source altitude for this beam is calculated from the apparent dispersion, assuming no atmospheric loss, the source region appears to be from 2000 km along the magnetic field line instead of the actual 4000 km used in this simulation. As mentioned above, the effect of the atmosphere depends strongly on the energy of the electrons and the atmospheric density. *Evans* [1967] calculates a source altitude of no more than 1300 km from *in-situ* electron differential number flux modulations using dispersion calculations while the rocket is flying between 90 and 150 km. While the electrons detected below 16 keV will probably give source regions which are too low due to the loss of energy to the atmosphere at the detection altitudes, the 60 and 120 keV electrons should still give an accurate source calculation assuming velocity dispersion between these electrons. It can

therefore be concluded that the source altitude of the modulations in electron differential flux in the tens to hundreds of keVs that *Evans* [1967] used leads to the correct result. There are a few explanations for electron flux modulation in the ionosphere below 1500 km [*Evans*, 1967; *Perkins*, 1968; *Lin and Hoffman*, 1979b; *Ganguli et al.*, 1994; *McHarg et al.*, 1998] as well as explanations for the modulation occurring at higher altitudes between 2500 and 8000 km [*Temerin et al.*, 1986, 1993; *Arnoldy et al.*, 1999]. This study of field-aligned bursts assumes the source region is at 4000 km, and the agreement between Figure 5.3 and *Arnoldy et al.* [1999] and *McFadden et al.* [1987] strongly suggests that the main electron modulations which create flickering aurora occur near the acceleration region, which is found at these high altitudes. However, it may be, as *McHarg et al.* [1998] suggest, that there is more than one process acting to modulate precipitating electrons, especially since a broadband frequency spectrum from optical observations cannot be explained with the optical modeling in this chapter.

As shown in Section 5.1.1 the velocity dispersion smoothes the optical intensity and the farther the source is from the upper atmosphere, the more the intensity will be smoothed. With a time-dependent transport code and recently developed instruments mentioned above [*H. Stenbaek-Nielsen*, personal communication, 1999; *McHarg et al.*, 1998; *Sakanoi et al.*, 1999], one should be able to deduce an upper bound on the altitude from which the electrons creating a flickering auroral display are modulated. Such instruments are well suited to detect the integrated column intensity variation in flickering aurora. To demonstrate what type of study one could do with a more complete time-dependent transport code, the time-dependent simulation was run for three different source altitudes and three different frequencies. Figure 5.8 shows the brightness modulation of the height integrated emission rate as a function of frequency for different source altitudes. The higher the frequency, the smaller the variation in brightness due to the velocity dispersion in the electrons and the slow decay of the higher altitude secondary intensities. The closer the source is to the atmosphere, the greater the variation since there is less dispersion. Given integrated optical column intensity variations of  $4278 \text{ \AA}$  of suprathermal field-aligned electron bursts, Figure 5.8 provides an upper bound on the altitude from which the bursts come.

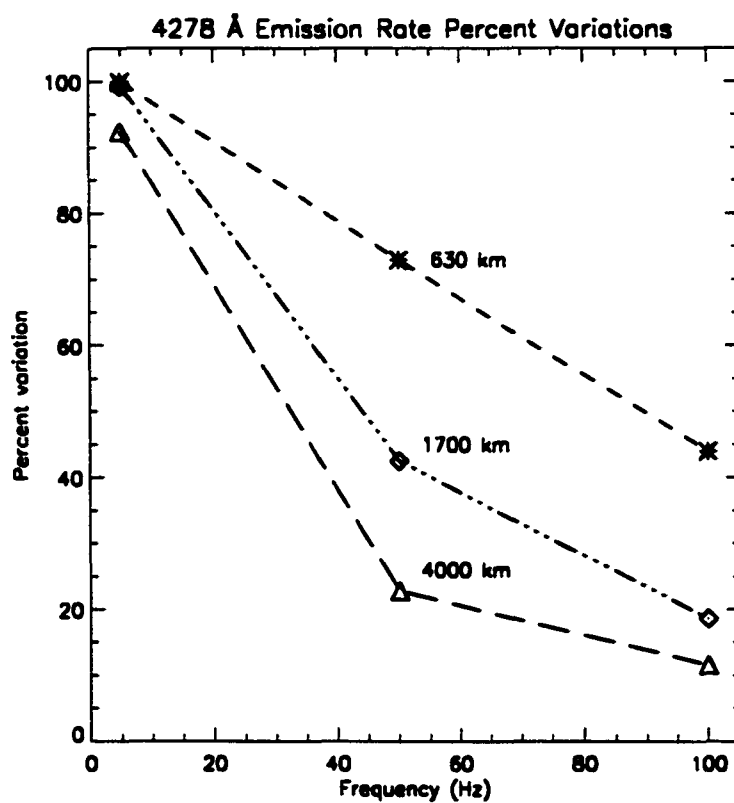


Figure 5.8. Brightness variations in 4278 Å. The variation in optical emission of 4278 Å as a function of frequency for three different source altitudes using the same initial downward electron intensities as for Figures 5.5 and 5.6.

In order to use such observations of brightness variations in flickering aurora with the transport calculation results, as in Figure 5.8, it is necessary to address some remaining issues. For white light measurements, it is important to include with the time-dependent transport calculation a synthetic spectrum to simulate white light measurements. The addition of the bright 6300 Å and 5577 Å emissions will add constant offsets to the optical observations which could decrease the percent variations as shown in Figure 5.8. It is also important to note that most of the electron fluxes that cause flickering aurora are not only low-energy, cold, field-aligned bursts but also high-energy, hot, pitch-angle-dispersed electrons as discussed in references above. This part of the spectra must be included in the model to obtain correct percent variation in optical brightness. Since the inverted-V electrons are often greater than 3 keV, these electrons will deposit their energy lower in the atmosphere and will create larger variations in brightness if they do flicker as *Arnoldy et al.* [1999] have shown. However, these electrons are also pitch angle dispersed, which will smooth the optical signal since electrons at larger pitch angles will deposit their energy at a later time than the field-aligned inverted-V electrons as well as at an altitude higher than these field-aligned electrons. Taking into account these considerations, it should be possible to use ground based optical measurements of flickering aurora and a time-dependent transport code to obtain an upper bound on the modulation source altitude.

In this chapter, the time-dependent transport simulation was used to study field-aligned bursts in flickering aurora. By comparing a 100 Hz *versus* a 5 Hz electron modulation, one is reminded that it is the time-averaged downward flux which gives the correct time-averaged emission rate. Of the physics included in the transport calculation, it is velocity dispersion of the modulated downward precipitating electrons that is the most important process which affecting the 4278 Å emission rate modulation. The effect of this dispersion depends on the altitude at which the field-aligned electron beams are modulated. From this, it may be possible to determine an upper bound on the altitude of the electron source.

Rocket and satellite differential flux measurements are common and important in studying flickering aurora and FABs. The results from this study have shown that velocity dispersion calculations using observations from well above 150 km for electrons less than ~2 keV because the energy degradation of these electrons in the upper atmosphere obscures the velocity dispersion. From the similarity of the differential flux at 502 km of this study

to that of the data by *Arnoldy et al.* [1999] and *McFadden et al.* [1987], there must be flickering aurora that is a result of electrons modulated at altitudes well above the lower ionosphere. These similarities also agree with the interpretation that the bursts seen in rocket and satellite detectors are a temporal rather than a spatial phenomena. With sufficient time resolution, one should be able to reconstruct the initial electron intensity from the bumps in the distribution function. The possibility of modulations in the lower ionosphere cannot be ruled out by this study, though the discrepancy between the *in-situ* modulation of high-energy electron *versus* low-energy electron modulations can be described by the time-dependent transport model.

## Chapter 6

# Summary and Conclusions

Auroral electron transport calculations are useful for studying precipitating electron intensities and the optical emissions produced from these intensities. The first time-dependent auroral electron transport model is developed in this thesis to calculate changing electron spherical intensities and optical emissions of  $N_2(2PG)$  and  $N_2^+(1NG)$  in time. It is demonstrated that a time-dependent transport calculation is a useful tool in determining the altitude of the electron source region from optical measurements taken with millisecond resolution and it will help interpret the spatial *versus* temporal effects in electron spectra measured in the aurora.

### 6.1 Summary

The solution to the time-dependent equation for different upper boundary conditions (Chapter 3) demonstrates that the time it takes the electron intensity to reach steady state can exceed 300 ms. The specific time to reach steady state depends on the energy of the precipitating electrons and the density of the neutral atmosphere. It is also shown that the time for the degraded primary and secondary electrons to thermalize takes longer than 150 ms. The relatively long time scales ( $>100$  ms) are primarily due to the slow growth and decay of secondary electron fluxes at energies less than 10 eV and at altitudes greater than 110 km. If the electron sources are rapidly varying, emissions that depend on low energies and high altitudes will have the largest errors when modeled using a steady-state transport

calculation.

The emission band of  $N_2^+(1NG)$  4278 Å for monoenergetic, field-aligned electrons is shown in Chapter 4 to have a very small time dependence, from less than 8 ms for a 10-keV beam to 15 ms for a 700-eV beam to reach its maximum column brightness. Of the 700-eV, 2-keV and 10-keV monoenergetic, field-aligned beams modeled in Chapter 3, only the 700-eV electrons are shown to produce emissions that move down in altitude with time. The time-dependent  $N_2^+(1NG)$  emission rate profiles for a Maxwellian and/or an isotropic electron beam will always produce flaming aurora that move up in altitude when the beam enters the upper atmosphere and again when the beam is turned off. Flaming on longer time scales has been observed *Sourfield and Parsons* [1969], although confirming that the moving brightness is due to flaming and not horizontal motion is difficult. If optical brightness is observed to move down a magnetic field line at millisecond time-scales instead of flame up a field line, then either the energy of the electrons is modified in time or the electron energies are less than 1 keV. The time for “flaming” to rise to its maximum altitude will depend on the spectrum of the incident electrons. For electrons being produced at 630 km, it takes a 2-keV, monoenergetic, isotropic beam 30 ms to flame upward in altitude to its maximum altitude. It takes 20 ms for a 2-keV, Maxwellian, field-aligned beam coming from 630 km to flame upward in altitude. Since the  $N_2^+(1NG)$  4278 Å band emission is proportional to the ionization rate, the ionization rate will change as a function of time and altitude. The time dependence of the ionization rate will not significantly affect the electron density since the ion chemistry reacts to pulses of electrons on the order of tens of seconds [*Palmer, 1995*].

The lower-energy electrons have a slower time dependence both because they move more slowly than the higher-energy electrons and because the inelastic cross sections are smaller at lower energies, making a slower loss rate at the lowest energies. This slower time dependence is shown in Chapter 4 in emission rate profiles and column brightnesses of the  $N_2(2PG)$  3371 Å band emission. The cross section of the parent state  $C^3\Pi_u$  of this emission peaks at ~14 eV, sampling the low-energy secondary electrons. Flaming in the  $N_2(2PG)$  emissions for a 2-keV Maxwellian, field-aligned electron beam takes three times longer to reach its peak column brightness than the  $N_2^+(1NG)$  emission. In the case of the 2-keV monoenergetic, isotropic electron beam, it takes just over two times longer for the  $N_2(2PG)$  emission to reach its peak column brightness than the  $N_2^+(1NG)$ . Quantitatively, it is easier



to discuss the way in which these two emissions change by using the ratio of the 3371 Å to 4278 Å brightnesses. This ratio changes differently in time depending on the incident electron intensity and can be used to determine the incident electron spectrum responsible for a particular auroral display.

To model field-aligned bursts (FABs) of electrons in flickering aurora it is important to use a time-dependent electron transport calculation because of the short duration and strong velocity dispersion within the beam. The velocity dispersion inhibits the prompt optical brightnesses from directly correlating with the source region on/off modulation of the electron intensity in time because it smooths the optical brightness compared with the electron modulation (Chapter 5). Because this velocity dispersion will smooth the optical signal more when the source is farther from the ionosphere, it is possible to use a time-dependent transport code and optical measurements using prompt emissions to determine an upper bound on the source altitude for the incident electrons. There will be additional significant smoothing of the variation in optical emissions due to the long lifetimes of 5577 Å and 6300 Å when observations are made with broadband filters or white light.

The ratio of  $N_2(2PG)$  to  $N_2^+(1NG)$  on millisecond time resolution provides another way to study flickering FABs. Because of the time lag in the growth and decay of the electrons exciting the  $N_2(2PG)$  emissions *versus* the  $N_2^+(1NG)$  emissions, the 3371Å/4278Å ratio will vary in time. The more distant the source of the flickering, the less this ratio will differ. Also, the frequency of brightness variations in these two emissions should be the same if the emissions are caused by electron transport effects. Different response characteristics observed in the lower-energy  $N_2(2PG)$  band emissions could be due to plasma waves interacting with the 14-eV electrons. Studying the emission rates at millisecond time scales is an excellent way to investigate not only the time dependence of the auroral electrons but helps to infer process in the lower ionosphere and in the acceleration region.

## 6.2 Discussion and Future Research

This study into the time dependence of auroral electrons suggests several new ways to study the aurora. First, however, the lack of a correct scattering term needs to be addressed. As shown in Chapter 3, it was possible to create an *ad hoc* method to ensure that the altitude

at which the bulk of the energy is deposited is consistent with the steady-state transport calculations. However, this method includes neither the time dependence of scattering nor does it correctly fill in the electron spherical differential flux between the peak energy of the precipitating electrons and the low-energy secondary electrons. Also, it does not allow a determination of the electrons that backscatter in time. The backscattered electrons are important since these are the electrons that return to the magnetosphere and may change stability properties of electron distribution functions and thus may change growth rates of waves in the acceleration region. Scattering must be included correctly into the time-dependent transport calculation also to quantify correctly the emission and ionization rates as a function of time. It would also be prudent include discrete energy losses below 3 keV instead of 70 eV (as done in this thesis). With the assumption that it will be possible to develop such a transport calculation in the not too distant future, the rest of the discussion will focus on how a test of a time-dependent transport calculation can be made and on the types of physics one can examine using a time-dependent transport equation.

The peaks in the column brightness of the 3371Å/4278Å ratio from flickering FABs will be noticeably out of phase with the 4278 Å brightness if the frequency of the flickering is on the order of the time lag between the 4278 and the 3371 Å brightness peaks caused by the different responses of electrons with different energies. For example, the 100-Hz flickering ratio is 20% out of phase with the 4278 Å brightness peaks. One way to test the computer model would be to observe the ratio of two photometers looking at the same 100-Hz flickering aurora and compare this ratio with the ratio obtained from the time-dependent transport computer modelling, although an even better experiment to test a time-dependent transport calculation would be to have a rocket or satellite measuring the electron intensity at millisecond resolution while traversing a flickering auroral form, with two cameras or photometers, one with a 4278 Å filter and another with a 3371 Å filter, looking along the magnetic field and also observing at millisecond resolution. *Arnoldy et al.* [1999] had instruments on board a rocket with millisecond resolution and cameras looking at the aurora beneath the rocket. But the cameras were not recording at millisecond resolution and instead of a N<sub>2</sub>(2PG) filter, one camera used a 5577 Å filter. Flickering is often recorded during rocket flights because it is associated with auroral break up. It should be possible to set up the appropriate cameras for a future rocket launch. An accurate time-dependent

auroral electron transport model, including scattering, may be developed in time for such an experiment.

Although white-light optical observations allow for observations of very dim aurora, with the long-lived emissions a constant offset, it is much too difficult to discern flaming due to the electron precipitation in the presence of this background emission. Not only are the oxygen 5577 Å and 6300 Å emissions long lived, but as was shown in Chapter 3, the secondaries at the higher altitudes can take as long as 300 ms to reach steady state. This means that the production of 5577 and 6300 Å emissions can take this long. The 5577 Å emission lifetime can be confused with the time dependence in the electron transport. If one is mostly interested in studying the electrons that cause the aurora, then it is important to know what emissions are due to direct electron collisions and what emissions are due to long lifetimes of the 6300 Å emission rate.

Even with filters to obtain only prompt emissions, flaming and horizontal motion are difficult to differentiate in optical observations. Another way of studying the electron transport to learn about the electron spectra and to separate the role of the ionosphere *versus* the role of the acceleration region in creating auroral optical emissions, is to have one camera looking in the magnetic zenith and another camera ~10 km away looking at the same auroral volume. This set up would be especially important in studying fast moving auroral filaments and curls since flaming could be well differentiated from horizontal motion with thin features from two locations. Observing the 3371 and 4278 Å emissions of curls and studying the ratio change at millisecond time scales will add further information needed to determine electrons spectra making up curls and the source region altitudes from where these curls originate.

Besides including scattering, it would be interesting to include some of the terms in the equation that were left out in this thesis. The non-linearity of the loss to the thermal electrons may be important to the time dependence of the very-low-energy electrons that excite the oxygen long-lived emissions. Modeling the plasma waves in the ionosphere using a time-dependent electron transport calculation to quantify what type of optical effect such waves have in the aurora could answer some long-debated questions regarding plasma waves and optical emissions. And if parallel electric fields do penetrate into the ionosphere, the effect on the electrons and the optical emissions resulting from such a field may help to

explain such things as the emissions seen in pulsating patches that have on the order of a kilometer in thickness in altitude [*Stenbaek-Nielsen and Hallinan, 1979*].

All in all, the variation in auroral electron fluxes in the ionosphere (especially the secondary electrons) due to millisecond changes in the precipitating electrons is considerably longer than was expected from the speeds of the high energy electrons. Studying the time dependence of the auroral electron transport has helped to fill a significant gap in our knowledge of the auroral electrons and their interaction with the upper atmosphere.

## Appendix A

# Relating Electron Functions in Phase Space

Differential electron flux detectors are usually found on rockets or satellites flying through a variety of space plasmas. These detectors measure particles with kinetic energies between  $E$  and  $E + dE$  that travel through a solid angle cone  $d\Omega$  opening about a unit vector  $\hat{\Omega}$  and cross a surface area  $d\vec{A}$  (a counting device) perpendicular to  $\hat{\Omega}$ ,  $\hat{\Omega} \cdot d\vec{A}$ . Figure A.1 shows an example of such a configuration. The number of counts measured by the detector will be proportional to the number of particles,  $dN$ , in this phase space with the constant of proportionality dependent on such things as the detector efficiency and spacecraft charging. The directional differential electron flux,  $\frac{\partial j(E, \hat{\Omega}, \vec{r}, t)}{\partial E}$  is related to  $dN$  by

$$dN = \frac{\partial j(E, \hat{\Omega}, \vec{r}, t)}{\partial E} \hat{\Omega} \cdot d\vec{A} d\Omega dE dt, \quad (\text{A.1})$$

where  $d\vec{A} = \hat{A} dA$ . The units of this differential flux are  $\# e^- / (\text{cm}^2 \cdot \text{s} \cdot \text{ster} \cdot \text{eV})$ . In electron transport theory,  $\frac{\partial j}{\partial E}$  is called angular intensity or angular flux or phase space flux with the symbols,  $I(E, \hat{\Omega}, \vec{r}, t)$  or  $\phi(E, \hat{\Omega}, \vec{r}, t)$  [Stamnes, 1977; Duderstadt, 1979; Lummerzheim, 1987]. The term flux is misleading since a flux is a vector quantity whereas this phase space quantity is a scalar [Duderstadt, 1979]. For this reason I will refer to this quantity as the angular intensity and will use the symbol  $I(E, \hat{\Omega}, \vec{r}, t)$ .

There are times when it may be useful to know the intensity as a function of velocity instead of energy and direction. For auroral electron transport theory, the assumption of

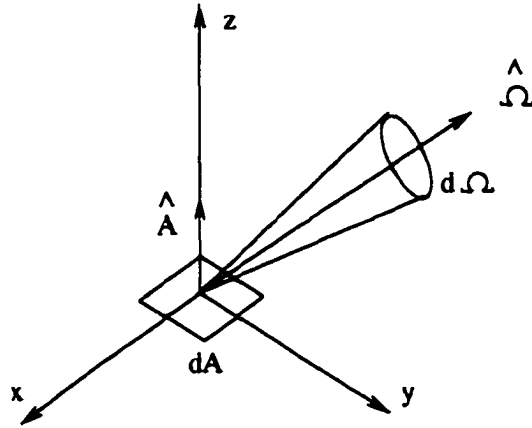


Figure A.1. The geometry for a differential electron flux detector. Note that  $d\vec{A} = \hat{A}dA$ .

asymuthal symmetry makes it convenient to speak of velocities parallel,  $v_{\parallel}$ , and perpendicular,  $v_{\perp}$ , to the magnetic field or energy,  $E$ , and the cosine of the pitch angle,  $\mu$ . These quantities are related to each other and to the cartesian velocity vector space in the following way (with  $z$  the direction of the magnetic field):

$$\begin{aligned}
 (v_x, v_y, v_z) &= (v_{\perp} \cos \phi, v_{\perp} \sin \phi, v_{\parallel}) \\
 (v_{\perp}, v_{\parallel}, \phi) &= \left( \sqrt{\frac{2E}{m}}(1 - \mu^2)^{1/2}, \mu \sqrt{\frac{2E}{m}}, \phi \right) \\
 (E, \mu, \phi) &= \left( \frac{1}{2}m(v_x^2 + v_y^2 + v_z^2), \frac{v_z}{\sqrt{v_x^2 + v_y^2 + v_z^2}}, \tan^{-1} \frac{v_y}{v_x} \right) \quad (\text{A.2})
 \end{aligned}$$

To transform an arbitrary function,  $g$ , from one coordinate system,  $(x_1, x_2, x_3)$ , to another,  $(y_1, y_2, y_3)$ , it is possible to use the fact that the function in one coordinate system times a differential volume in that coordinate system is the same in another coordinate system,

$$g(x_1, x_2, x_3)dx_1dx_2dx_3 = g(y_1, y_2, y_3)dy_1dy_2dy_3,$$

and that the differential volumes in the two coordinate systems are related through the

Jacobian,  $J_{xy}$ , by means of

$$dx_1 dx_2 dx_3 = J_{xy} dy_1 dy_2 dy_3,$$

where  $J_{xy}$  is a matrix with elements  $\frac{\partial x_i}{\partial y_j}$ ,  $i, j = 1, 2, 3$ . The way that the function in the two coordinate systems is related can thus be written as

$$g(x_1, x_2, x_3) = \frac{1}{J_{xy}} g(y_1, y_2, y_3).$$

Using this equation, any function,  $g$  of  $(E, \hat{\Omega}, \vec{r}, t)$  to  $(\vec{v}, \vec{r}, t)$  can be transformed via

$$g(E, \hat{\Omega}, \vec{r}, t) = \frac{v}{m} g(\vec{v}, \vec{r}, t), \quad (\text{A.3})$$

and thus

$$I(E, \hat{\Omega}, \vec{r}, t) = \frac{v}{m} I(\vec{v}, \vec{r}, t). \quad (\text{A.4})$$

In the kinetic theory of electrons, it is often convenient to model the electron phase space distribution function,  $f(\vec{v}, \vec{r}, t)$ . It is important to know how  $f$  and  $I$  are related in order to compare electron measurements with theories involving  $f$ . From Equation A.1 and from using the rules involving transformations of functions above,

$$dN = I(E, \hat{\Omega}, \vec{r}, t) dt \hat{\Omega} \cdot d\vec{A} d\hat{\Omega} dE = I(\vec{v}, \vec{r}, t) dt \hat{\Omega} \cdot d\vec{A} d^3\vec{v}. \quad (\text{A.5})$$

Also, it is known that

$$dN = f(\vec{v}, \vec{r}, t) d^3\vec{r} d^3\vec{v}. \quad (\text{A.6})$$

If one thinks back to the particle detector (see Figure A.1), the electrons in the volume  $d^3\vec{r}$  are those that have travelled through the detector opening and traced out a column of space in  $dt$  with the side defined by  $v dt$  and the area defined by  $\hat{\Omega} \cdot d\vec{A}$ . Thus,  $d^3\vec{r}$  can be rewritten as  $v dt \hat{\Omega} \cdot d\vec{A}$  to obtain

$$dN = f(\vec{v}, \vec{r}, t) v dt \hat{\Omega} \cdot d\vec{A} d^3\vec{v} = I(\vec{v}, \vec{r}, t) dt \hat{\Omega} \cdot d\vec{A} d^3\vec{v}, \quad (\text{A.7})$$

which implies that

$$I(\vec{v}, \vec{r}, t) = v f(\vec{v}, \vec{r}, t). \quad (\text{A.8})$$

Combining Equation A.8 with Equation A.4 an equation is obtained to relate what is measured,  $I(E, \hat{\Omega}, \vec{r}, t)$ , versus what is modelled in kinetic theory,  $f(\vec{v}, \vec{r}, t)$ :

$$I(E, \hat{\Omega}, \vec{r}, t) = \frac{v^2}{m} f(\vec{v}, \vec{r}, t). \quad (\text{A.9})$$

In Chapter 2, the auroral electron transport equation is derived using  $f = f(E, \hat{\Omega}, \vec{r}, t)$ . This quantity can be related to  $I = I(E, \hat{\Omega}, \vec{r}, t)$  using the same concept as was used in Equation A.7 as well as Equation A.3 for  $f$  to obtain:

$$I(E, \hat{\Omega}, \vec{r}, t) = \sqrt{\frac{2E}{m}} f(E, \hat{\Omega}, \vec{r}, t). \quad (\text{A.10})$$

This relation is used to obtain Equation 2.21 in Chapter 2.



# Bibliography

- Akasofu, S. I., and J. R. Kan (Eds.), *Physics of Auroral Arc Formation*, Geophys. Monog. 25, American Geophysical Union, Washington, DC, 1981.
- Angelopoulos, V., C. F. Kennel, F. V. Coroniti, R. Pellat, M. G. Kivelson, R. J. Walker, C. T. Russell, W. Baumjohann, W. C. Feldman, and J. T. Gosling, Statistical characteristics of bursty bulk flow events, *J. Geophys. Res.*, 99, 21257, 1994.
- Arnoldy, R. L., Rapid fluctuations of energetic auroral particles, *J. Geophys. Res.*, 75, 228, 1970.
- Arnoldy, R. L., Review of auroral particle precipitation, in *Physics of Auroral Arc Formation*, edited by S. I. Akasofu and J. R. Kan, American Geophysical Union, Washington D.C., 1981.
- Arnoldy, R. L., T. E. Moore, and L. J. C. Jr., Low-altitude field-aligned electrons, *J. Geophys. Res.*, 90, 8445, 1985.
- Arnoldy, R. L., K. A. Lynch, J. B. Austin, and P. M. Kintner, Energy and pitch angle dispersed auroral electrons suggesting a time-variable inverted-V potential structure, *J. Geophys. Res.*, 104, 22613, 1999.
- Banks, P. M., C. R. Chappell, and A. F. Nagy, A new model for the interaction of auroral electrons with the atmosphere: Spectral degradation, backscatter, optical emission, and ionization, *J. Geophys. Res.*, 79, 1459, 1974.
- Barth, C. A., S. M. Baily, and S. C. Solomon, Solar-terrestrial coupling: Solar soft x-rays and thermospheric nitric oxide, *Geophys. Res. Lett.*, 26, 1251, 1999.

- Beach, R., G. R. Cresswell, T. N. Davis, T. J. Hallinan, and L. R. Sweet, Flickering, a 10 cps fluctuation within bright auroras, *Planet. Space Sci.*, *16*, 1525, 1968.
- Beluja, K. L., and C. J. Zeippen, M1 and E2 transition probabilities for states within the  $2p^4$  configuration of the OI isoelectric sequence, *J. Phys. B.*, *21*, 1455, 1988.
- Berkey, F. T., M. B. Silevitch, and N. R. Parsons, Time sequence analysis of flickering auroras 1. Application of fourier analysis, *J. Geophys. Res.*, *85*, 6827, 1980.
- Bilitza, D., K. Rawer, L. Bossy, and T. Gulyaeva, International reference ionosphere - past, present, future, *Adv. Space Res.* *13*, 3, 3, 1993.
- Borovsky, J. E., Auroral arc thickness as predicted by various theories, *J. Geophys. Res.*, *98*, 6101, 1993.
- Borovsky, J. E., D. M. Suszcynsky, M. I. Buchwald, and H. V. DeHaven, Measuring the thicknesses of auroral curtains, *Arctic*, *44*, 231, 1991.
- Borst, W. L., and E. C. Zipf, Cross section for e impact excitation of the  $0,0\ 1N\ N_2^+$  band from threshold to 3 keV, *Phys. Rev.*, *A1*, 834, 1970.
- Bryant, D. A., Rocket studies of particle structure associated with auroral arcs, in *Physics of Auroral Arc Formation*, edited by S. I. Akasofu and J. R. Kan, American Geophysical Union, Washington D.C., 1981.
- Carlson, C. W., R. F. Pfaff, and J. G. Watzin, The Fast Auroral SnapshoT (FAST) mission, *Geophys. Res. Lett.*, *25*, 2013, 1998.
- Cartwright, D. C., S. Trajmar, and W. Williams, Vibrational population of the  $A^3\Sigma_u^+$  and  $B^3\Pi_g$  states of  $N_2$  in normal auroras, *J. Geophys. Res.*, *76*, 8368, 1971.
- Cartwright, D. C., S. Trajmar, and W. Williams, Reply, *J. Geophys. Res.*, *78*, 2365, 1973.
- Cercignani, C., *The Boltzmann Equation and Its Applications*, Springer-Verlag, New York, New York, 1998.
- Chamberlain, J. W., *Theory of Planetary Atmospheres: An Introduction to Their Physics and Chemistry*, Academic Press, New York, N. Y., 1978.

- Chamberlain, J. W., *Physics of the Aurora and Airglow*, American Geophysical Union, Washington, D. C., 1995.
- Cresswell, G. R., Flaming auroras, *J. Atmos. Terrest. Phys.*, *31*, 179, 1969.
- Doering, J. P., and J. Yang, Direct experimental measurements of electron impact ionization-excitation branching ratios: 3. Branching ratios and cross sections for the  $N_2^+ X^2\Sigma_g^+$ ,  $A^2\Pi_u$ , and  $B^2\Sigma_u^+$  states at 100 ev, *J. Geophys. Res.*, *102*, 9683, 1997.
- Duderstadt, J. J., *Transport Theory*, John Wiley and Sons, New York, New York, 1979.
- Evans, D. S., A 10-cps periodicity in the precipitation of auroral-zone electrons, *J. Geophys. Res.*, *72*, 4281, 1967.
- Evans, D. S., The observations of a near monoenergetic flux of auroral electrons, *J. Geophys. Res.*, *73*, 2315, 1968.
- Evans, D. S., Precipitating electron fluxes formed by a magnetic field-aligned potential difference, *J. Geophys. Res.*, *79*, 2853, 1974.
- Feautrier, P., Sur la résolution numérique de l'équation de transfert, *C. R. Acad. Sci. Paris*, *258*, 3189, 1964.
- Fennell, J. F., D. J. Gorney, and P. F. Mizera, Auroral particle distribution functions and their relationship to inverted Vs and auroral arcs, in *Physics of Auroral Arc Formation*, edited by S. I. Akasofu and J. R. Kan, American Geophysical Union, Washington D.C., 1981.
- Fletcher, C. A. J., *Computational Techniques for Fluid Dynamics*, 2nd ed., Springer-Verlag, Berlin Heidelberg, 1991.
- Frank, L. A., and K. L. Ackerson, Observations of charged particle precipitation into the auroral zone, *J. Geophys. Res.*, *76*, 3612, 1971.
- Frey, H. U., G. Haerendel, J. Clemmons, D. D. Wallis, J. Vogt, O. H. Bauer, E. Rieger, M. H. Boehm, and H. Luhr, Studies of auroral arcs using Freja satellites and ground-based data, *Adv. Space Res.*, *18*, 107, 1996.

- Ganguli, G., M. J. Keskkinen, H. Roero, R. Heelis, T. Moore, and C. Pollock, Coupling of microprocesses and macroprocesses due to velocity shear: An application to the low-altitude ionosphere, *J. Geophys. Res.*, **99**, 8873, 1994.
- Gattinger, R. L., A. Vallance Jones, J. H. Hecht, D. J. Strickland, and J. Kelly, Comparison of ground-based optical observations of  $N_2$  second positive to  $N_2^+$  first negative emission ratios with electron precipitation energies inferred from the Sondre Stromfjord radar, *J. Geophys. Res.*, **96**, 11,341, 1991.
- Gorney, D. J., Overview of auroral spatial scales, in *Auroral Physics*, edited by C. I. Meng et al., p. 325, Cambridge University Press, New York, NY, 1991.
- Hallinan, T. J., Auroral spirals, 2. Theory, *J. Geophys. Res.*, **81**, 3959, 1976.
- Hallinan, T. J., Auroras, in *Geomagnetism V 4*, edited by J. Jacobs, chap. 8, Academic Press, 1991.
- Hallinan, T. J., and T. N. Davis, Small-scale auroral arc distortions, *Planet. Space Sci.*, **18**, 1735, 1970.
- Hallinan, T. J., H. C. Stenbaek-Nielsen, J. Kimball, D. Swift, C. W. Carlson, J. P. McFadden, and M. Temerin, A case study of flickering aurora using auroral images together with FAST data, *Eos Trans. AGU*, **77**, Spring Meet. Suppl., 1997.
- Hallinan, T. J., J. Kimball, D. Osborne, and C. S. Deehr, Spectra of type-b red lower borders, *J. Geophys. Res.*, **103**, 11635, 1998.
- Hays, P. B., R. A. Jones, and M. H. Rees, Auroral heating and the composition of the neutral atmosphere, *Planetary Space Sci.*, **21**, 559, 1973.
- Heavner, M. J., *Optical Spectroscopic Observations of Sprites, Blue Jets, and Elves: Inferred Microphysical Processes and Their Macrophysical Implications*, Ph.D. thesis, University of Alaska, Fairbanks, 2000.
- Hedin, A. E., Extension of the MSIS thermosphere model into the middle and lower atmosphere, *J. Geophys. Res.*, **96**, 1159, 1991.

- Hultqvist, B., M. Oeieroset, G. Paschmann, and R. Treumann, Magnetospheric plasma sources and losses, *Space Sci. Rev.*, *88*, 1, 1999.
- Itikawa, Y., and O. Aono, Energy change of a charged particle moving in a plasma, *Physics Fluids*, *9*, 1259, 1966.
- Jackson, J. D., *Classical Electrodynamics*, John Wiley and Sons, New York, NY, 1975.
- Johnstone, A. D., and J. D. Winningham, Satellite observations of suprathermal electron bursts, *J. Geophys. Res.*, *87*, 2321, 1982.
- Kelley, M. C., *The Earth's Ionosphere: Plasma Physics and Electrodynamics*, Academic Press, San Diego, CA, 1989.
- Khazanov, G. V., and M. W. Liemohn, Nonsteady state ionosphere-plasmasphere coupling of superthermal electrons, *J. Geophys. Res.*, *100*, 9669, 1995.
- Kunitake, M., and T. Oguti, Spatial-temporal characteristics of flickering spots in flickering auroras, *J. Geomagn. Geoelectr.*, *36*, 121, 1984.
- Lanchester, B. S., J. R. Palmer, M. H. Rees, D. Lummerzheim, K. Kaila, and T. Turunen, Energy flux and characteristic energy of an elemental auroral structure, *Geophys. Res. Lett.*, *21*, 2789, 1994.
- Lanchester, B. S., M. H. Rees, D. Lummerzheim, A. Otto, H. U. Frey, and K. U. Kaila, Large fluxes of auroral electrons in filaments of 100 m width, *J. Geophys. Res.*, *102*, 9741, 1997.
- Lennartsson, O. W., A scenario for solar wind penetration of the earth's magnetic tail based on ion composition data from the ISSEE-1 spacecraft, *J. Geophys. Res.*, *97*, 19221, 1992.
- Liemohn, M. W., G. V. Khazanov, T. E. Moore, and S. M. Guiter, Self-consistent superthermal electron effects on plasmaspheric refilling, *J. Geophys. Res.*, *102*, 7523, 1997.
- Lin, C. S., and R. A. Hoffman, Characteristics of the inverted-V event, *J. Geophys. Res.*, *84*, 1514, 1979a.

- Lin, C. S., and R. A. Hoffman, Fluctuations of inverted V electron fluxes, *J. Geophys. Res.*, **84**, 6547, 1979b.
- Link, R., Feautrier solution of the electron transport equation, *J. Geophys. Res.*, **97**, 159, 1992.
- Lummerzheim, D., *Electron Transport and Optical Emissions in the Aurora*, Ph.D. thesis, University of Alaska, Fairbanks, 1987.
- Lummerzheim, D., and J. Liliensten, Electron transport and energy degradation in the ionosphere: Evaluation of the numerical solution, comparison with laboratory experiments and auroral observations, *Ann. Geophys.*, **12**, 1039, 1994.
- Lummerzheim, D., M. H. Rees, and H. R. Anderson, Angular dependent transport of auroral electrons in the upper atmosphere, *Planet. Space Sci.*, **37**, 1989, 1989.
- Lund, E. J., J. LaBelle, R. B. Torbert, K. Liou, W. Peria, C. A. Kletzing, M. C. Kelley, S. D. Baker, F. Primdahl, H. C. Stenbaek-Nielsen, A. Ranta, G. Haerendel, and H. U. Frey, Observation of electromagnetic oxygen cyclotron waves in a flickering aurora, *Geophys. Res. Lett.*, **22**, 2465, 1995.
- Lundin, R., and L. Eliasson, Auroral energization processes, *Ann. Geophysicae*, **9**, 202, 1991.
- Lundin, R., G. Haerendel, and S. Grahn, The Freja Project, *Geophys. Res. Lett.*, **21**, 1823, 1994.
- Lysak, R. L. (Ed.), *Auroral Plasma Dynamics*, Geophys. Monog. 80, American Geophysical Union, Washington, DC, 1993.
- Maggs, J. E., and T. N. Davis, Measurements of the thickness of auroral structures, *Planet. Space Sci.*, **16**, 205, 1968.
- Marklund, G. T., Viking investigations of auroral electrodynamic parameters, *J. Geophys. Res.*, **98**, 1691, 1993.
- McFadden, J. P., C. W. Carlson, M. H. Boehm, and T. J. Hallinan, Field-aligned electron flux oscillations that produce flickering aurora, *J. Geophys. Res.*, **92**, 11133, 1987.

- McHarg, M. G., D. L. Hampton, and H. C. Stenbaek-Nielsen, Fast photometry of flickering in discrete auroral arcs, *Geophys. Res. Lett.*, *25*, 2637, 1998.
- Meng, C. I., Auroral arcs observed by DMSP satellites, in *Physics of Auroral Arc Formation*, edited by S. I. Akasofu and J. R. Kan, American Geophysical Union, Washington D.C., 1981.
- Min, Q. L., D. Lummerzheim, M. H. Rees, and K. Stamnes, Effects of a parallel electric field and the geomagnetic field in the topside ionosphere on auroral and photoelectric energy distributions, *J. Geophys. Res.*, *98*, 19223, 1993.
- Morrill, J. S., and W. M. Benesch, Auroral N<sub>2</sub> emissions and the effect of collisional processes on N<sub>2</sub> triplet state vibrational populations, *J. Geophys. Res.*, *101*, 261, 1996.
- Mozer, F. S., C. W. Carlson, M. K. Hudson, R. B. Torbert, B. Parady, J. Yatteau, and M. C. Kelley, Observations of paired electrostatic shocks in the polar magnetosphere, *Phys. Rev. Lett.*, *38*, 292, 1977.
- Nicholls, R. W., Aeronomically important transition probability data, *Can. J. Chem.*, *47*, 1847, 1969.
- Ohwada, T., Higher order approximation methods for the Boltzmann equation, *J. Comput. Phys.*, *139*, 1, 1998.
- Onda, K., M. Ejiri, and Y. Itikawa, Analysis of electron auroras based on the Monte Carlo method: Application to active electron arc auroras observed by the sounding rocket at Syowa Station, *J. Geophys. Res.*, *104*, 27991, 1999.
- Opal, C. B., W. K. Peterson, and E. C. Beaty, Measurements of secondary-electron spectra produced by electron impact ionization of a number of simple gases., *J. Chem. Phys.*, *55*, 4100, 1971.
- Otto, A., and G. T. Birk, Formation of thin auroral arcs by current striation, *Geophys. Res. Lett.*, *20*(24), 2833, 1993.
- Palmer, J., *Plasma Density Variations in the Aurora*, Ph.D. thesis, University of Southampton, 1995.

- Paterson, W. R., and L. A. Frank, Survey of plasma parameters in the earth's distant magnetotail with the Geotail spacecraft, *Geophys. Res. Lett.*, *21*, 2971, 1994.
- Perkins, F. W., Plasma-wave instabilities in the ionosphere over the aurora, *J. Geophys. Res.*, *73*, 6631, 1968.
- Porter, H. S., F. Varosi, and H. G. Mayr, Iterative solution of the multistream electron transport equation: 1. Comparison with laboratory beam injection experiments, *J. Geophys. Res.*, *92*, 5933, 1987.
- Pulliam, D. M., H. R. Anderson, K. Stamnes, and M. H. Rees, Auroral electron acceleration and atmospheric interactions: (1) Rocket-borne observations and (2) Scattering calculations, *J. Geophys. Res.*, *86*, 2397, 1981.
- Reasoner, D. L., and C. R. Chappell, Twin payload observations of incident backscattered auroral electrons, *J. Geophys. Res.*, *78*, 2176, 1973.
- Rees, M. H., A method for determining the height and geographical position of an auroral arc from one observing station, *J. Geophys. Res.*, *68*, 175, 1963.
- Rees, M. H., *Physics and Chemistry of the Upper Atmosphere*, Cambridge University Press, New York, NY, 1989.
- Rees, M. H., and D. Lummerzheim, Auroral excitation processes, in *Auroral Physics*, edited by C. I. Meng et al., p. 29, Cambridge University Press, New York, NY, 1991.
- Rees, M. H., A. I. Steward, and J. C. G. Walker, Secondary electrons in aurora, *Planet. Space. Sci.*, *17*, 1997, 1969.
- Rees, M. H., D. Lummerzheim, R. G. Roble, J. D. Winningham, J. D. Craven, and L. A. Frank, Auroral energy deposition rate, characteristic electron energy, and ionospheric parameters derived from Dynamics Explorer 1 images, *J. Geophys. Res.*, *93*, 12841, 1988.
- Richards, P. G., and D. G. Torr, Auroral modeling of the 3371 Å emission rate: Dependence on characteristic electron energy, *J. Geophys. Res.*, *95*, 10337, 1990.
- Richmond, A. D., E. C. Ridley, and R. G. Roble, A thermosphere/ionosphere general circulation model with coupled electrodynamics, *Geophys. Res. Lett.*, *19*, 601, 1992.



- Roble, R. G., and E. C. Ridley, An auroral model for the NCAR thermospheric general circulation model (TGCM), *Ann. Geophys.*, *5A*, 369, 1987.
- Sakanoi, K., and H. Fukunishi, Multi-anode fast photometer observations of flickering aurora at Syowa Station, *Eos Trans. AGU*, *80(46)*, Fall Meet. Suppl., F767, 1999.
- Schlesier, A. C., M. J. Buonsanto, and S. C. Solomon, Secondary ionization in ionospheric modelling, *CEDAR*, 1997.
- Semeter, J., D. Lummerzheim, R. L. Arnoldy, K. A. Lynch, J. Vogt, and G. Haerendel, Modeling optical emissions of flickering aurora, *Eos Trans. AGU*, *80(17)*, Spring Meet. Suppl., S250, 1999.
- Sharp, R. D., E. G. Shelley, R. G. Johnson, and A. G. Ghielmetti, Counterstreaming electron beams at altitudes of  $1 R_E$  over the auroral zone, *J. Geophys. Res.*, *85*, 92, 1980.
- Shemansky, D. E., and A. L. Broadfoot, Excitation of N and N systems by electrons. I. Absolute transition probabilities, *J. Quant. Spectrosc. Radiat. Transfer*, *11*, 1385, 1971.
- Shemansky, D. E., and A. L. Broadfoot, Comment on paper by D.C. Cartwrite, S. Trajmar, and W. Williams: Vibrational population of the  $A^3\Sigma_u^+$  and  $B^3\Pi_g$  states of  $N_2$  in normal auroras, *J. Geophys. Res.*, *78*, 2357, 1973.
- Shepherd, G. G., A. Steen, and J. S. Murphree, Auroral boundary dynamics observed simultaneously from the Viking spacecraft and from the ground, *J. Geophys. Res.*, *95*, 5845, 1990.
- Sivjee, G. G., and D. Shen, Auroral optical emissions during the solar magnetic cloud event of October 1995, *J. Geophys. Res.*, *102*, 7431, 1997.
- Solomon, S., Progress towards a quantitative understanding of Antarctic ozone depletion, *Nature*, *347*, 347, 1990.
- Solomon, S. C., Auroral transport using the Monte Carlo method, *Geophys. Res. Lett.*, *20*, 185, 1993.
- Solomon, S. C., C. A. Barth, and S. M. Baily, Auroral production of nitric oxide measured by the SNOE satellite, *Geophys. Res. Lett.*, *26*, 1259, 1999.

- Sourfield, M. W. J., and N. R. Parsons, Auroral pulsations and flaming - some initial results of a cinematographic study using an image intensifier, *Planet. Space Sci.*, *17*, 1141, 1969.
- Spiger, R. J., and H. R. Anderson, Fluctuations of precipitated electron intensity in flickering auroral arcs, *J. Geophys. Res.*, *90*, 6647, 1985.
- Stamnes, K., Analytic approach to photoelectron transport: Extensions of Stolarski's (1972) work, *J. Geophys. Res.*, *82*, 2391, 1977.
- Stamnes, K., *A Theoretical Investigation of the Interaction of Auroral Electrons with the Atmosphere*, Ph.D. thesis, University of Colorado, Colorado, 1978.
- Stamnes, K., Analytic approach to auroral electron transport and energy degradation, *Planet. Space Sci.*, *28*, 427, 1980.
- Stamnes, K., and P. Conklin, A new multi-layer discrete ordinate approach to radiative transfer in vertically inhomogeneous atmospheres, *J. Quant. Spectrosc. Radiat. Transfer*, *31*, 273, 1984.
- Stamnes, K., and M. H. Rees, Inelastic scattering effects on photoelectron spectra and ionospheric electron temperature, *J. Geophys. Res.*, *88*, 6301, 1983.
- Stenbaek-Nielsen, H. C., and T. J. Hallinan, Pulsating auroras: Evidence for noncollisional thermalization of precipitating electrons, *J. Geophys. Res.*, *84*, 3257, 1979.
- Stenbaek-Nielsen, H. C., T. J. Hallinan, E. M. Wescott, and H. Föppl, Acceleration of barium ions near 8000 km above an aurora, *J. Geophys. Res.*, *89*, 10,788, 1984.
- Stenbaek-Nielsen, H. C., T. J. Hallinan, D. L. Osborne, J. Kimball, C. Chaston, J. McFadden, G. Delory, M. Temerin, and C. W. Carlson, Aircraft observations conjugate to FAST: auroral arc thicknesses, *Geophys. Res. Lett.*, *25*, 2073, 1998.
- Stoermer, C., *The Polar Aurora*, Clarendon Press, Oxford, 1955.
- Stoker, P. H., M. J. Mathews, and M. W. Scourfield, Co-ordinated measurements of auroral light intensities and riometric radio wave absorption, *Geophys. Res. Lett.*, *23*, 641, 1996.

- Strickland, D. J., and I. B. Bernstein, Angular properties of particle fluxes for strongly forward-peaked scattering, *J. Appl. Phys.*, **47**, 2184, 1976.
- Strickland, D. J., D. L. Brook, T. P. Coffey, and J. A. Fedder, Transport equation techniques for the deposition of auroral electrons, *J. Geophys. Res.*, **81**, 2755, 1976.
- Strickland, D. J., R. R. Meier, J. H. Hecht, and A. B. Christensen, Deducing composition and incident electron spectra from ground based auroral optical measurements: Theory and model results, *J. Geophys. Res.*, **94**, 13,527, 1989.
- Swartz, W. E., Thermalization and transport of photoelectrons: a comparison of theoretical approaches 2. Transport details for isotropic scattering, *J. Geophys. Res.*, **76**, 8425, 1971.
- Swartz, W. E., Optimization of energetic electron energy degradation calculations, *J. Geophys. Res.*, **90**, 6587, 1985.
- Swartz, W. E., J. S. Nisbet, and A. S. Green, Analytic expression for the energy-transfer rate from photoelectrons to thermal-electrons, *J. Geophys. Res.*, **76**, 8425, 1971.
- Temerin, M., J. McFadden, M. Boehm, and C. W. Carlson, Production of flickering aurora and field-aligned electron flux by electromagnetic ion cyclotron waves, *J. Geophys. Res.*, **91**, 5769, 1986.
- Temerin, M., C. Carlson, and J. P. McFadden, The acceleration of electrons by electromagnetic ion cyclotron waves, in *Auroral Plasma Dynamics, Geophys. Monog.*, vol. 80, edited by Robert L. Lysak, , American Geophysical Union, Washington, DC, 1993.
- Trondsen, T., *High Resolution Auroral Imaging*, Ph.D. thesis, University of Tromso, 1998.
- Truffer, M., *Till Deformation Beneath Black Rapids Glacier, Alaska, and Its Implication on Glacier Motion*, Ph.D. thesis, University of Alaska, Fairbanks, 1999.
- Vallance Jones, A., *Aurora*, D. Reidel Publishing Company, Boston, MA, 1974.
- Vallance Jones, A., Overview of auroral spectroscopy, in *Auroral Physics*, edited by C. I. Meng et al., p. 15, Cambridge University Press, New York, NY, 1991.

- Vallance Jones, A., and R. L. Gattinger, Auroral spectroscopy and its application to the characterization of primary particle fluxes, *J. Geom. Geoelectr.*, **42**, 1385, 1990.
- Vallance Jones, A., R. L. Gattinger, F. Creutzberg, F. R. Harris, A. G. McNamara, A. W. Yau, E. J. Llewellyn, D. Lummerzheim, M. H. Rees, I. C. McDade, and J. Margot, The ARIES auroral modelling campaign: Characterization and modelling of an evening auroral arc observed from a rocket and a ground-based line of meridian scanners, *Planet. Space Sci.*, **39**, 1677, 1991.
- Waite, J. H., M. O. Chandler, R. V. Yelle, B. R. Sandel, and T. E. Cravens, Superthermal electron processes in the upper atmosphere of uranus: Aurora and electroglow, *J. Geophys. Res.*, **93**, 14295, 1988.
- Walt, M., W. M. Macdonald, and W. E. Francis, Penetration of auroral electrons into the atmosphere, in *Physics of the Magnetosphere*, edited by R. L. Carovillano, p. 435, Reidel Publishing, Dordrecht, Netherlands, 1969.
- Wescott, E. M., H. C. Stenbaek-Nielsen, T. N. Davis, and H. M. Peek, The Skylab barium plasma injection experiments, Part 1: Convection observations, *J. Geophys. Res.*, **81**, 4487, 1976.
- Wescott, E. M., T. J. Hallinan, H. C. Stenbaek-Nielsen, D. W. Swift, and D. D. Wallis, Rapid ray motions in barium plasma clouds and auroras, *J. Geophys. Res.*, **98**, 3711, 1993.
- Wiscombe, W. J., The delta-M method: Rapid yet accurate radiative flux calculations for strongly asymmetric phase functions, *J. Atmos. Sci.*, **34**, 1408, 1977.
- Wolf, R. A., Introduction to space physics, edited by M. G. Kivelson and C. T. Russell, chap. 10, Cambridge University Press, Cambridge, United Kingdom, 1997.
- Zhu, H., *Small Spatial and Fast Temporal Ionosphere-Magnetosphere Coupling Processes*, Ph.D. thesis, University of Alaska, Fairbanks, 2000.
- Zhu, H., A. Otto, M. H. Rees, B. S. Lanchester, and D. Lummerzheim, Ionosphere-magnetosphere simulation of small scale structure and dynamics, *Submitted, J. Geophys. Res.*, 2000.

Zwickl, R. D., D. N. Baker, S. J. Bame, W. Feldman, J. T. Gosling, E. W. H. Jr., D. J. McCormas, B. T. Tzurutani, and J. A. Slavin, Evolution of the earth's distant magnetotail: ISEE 3 electron plasma results, *J. Geophys. Res.*, *89*, 11007, 1984.